The Dissertation Committee for Arturo Javier Contreras Certifies that this is the approved version of the following dissertation:

Spatial Delineation, Fluid-Lithology Characterization, and Petrophysical Modeling of Deepwater Gulf of Mexico Reservoirs through Joint AVA Deterministic and Stochastic Inversion of 3D Partially-Stacked Seismic Amplitude Data and Well Logs

Committee:

William L. Fisher, Supervisor

Carlos Torres-Verdin, Co-Supervisor

William E. Galloway

Robert Tatham

Lesli J. Wood

Spatial Delineation, Fluid-Lithology Characterization, and Petrophysical Modeling of Deepwater Gulf of Mexico Reservoirs through Joint AVA Deterministic and Stochastic Inversion of 3D Partially-Stacked Seismic Amplitude Data and Well Logs

by

Arturo Javier Contreras, B. S.

Dissertation

Presented to the Faculty of the Graduate School of
The University of Texas at Austin
in Partial Fulfillment
of the Requirements
for the Degree of

Doctor of Philosophy

The University of Texas at Austin
May 2006

Dedication

To the Almighty, who keeps leading my way, and to my wife Silvia and sons Angel and Miguelangel, for their lovely support and inspiration.

Acknowledgements

First I would like to express my most sincere gratitude and appreciation to my advisor, Dr. William Fisher; his patience, understanding, constant guidance, and suggestions have made my stay at The University of Texas at Austin a wonderful experience. I would also like to express my gratitude to my co-advisor Dr. Carlos Torres-Verdin, who gave me the opportunity of joining his research group and consortium in Formation Evaluation at the Department of Petroleum and Geosystems Engineering. He introduced me to the wonderful world of inverse methods, and he showed me the importance of searching for meaningful ways to better promote quantitative science and data integration in geosciences. Special thanks go to my committee members, Dr. William Galloway, Dr. Robert Tatham, and Dr. Lesli Wood, for their valuable comments, recommendations, and contributions.

I am grateful to PDVSA-CIED and Universidad Central de Venezuela for awarding me a scholarship to pursue doctoral studies at The University of Texas at Austin.

I would like to extend my gratitude to Western Geco and Anadarko Petroleum Corporation for releasing the data set reported in this dissertation and to Fugro-Jason for their generous donation of the software used to carry out the seismic inversions.

The work reported in this dissertation was partially funded by UT Austin's Research Consortium on Formation Evaluation (Department of Petroleum and Geosystems Engineering), jointly sponsored by Anadarko Petroleum Corporation, Baker Atlas, BP, ConocoPhillips, ExxonMobil, Halliburton Energy Services, the Mexican Institute for Petroleum, Occidental Petroleum, Petrobras, Precision Energy Services, Schlumberger, Shell International E&P, Statoil, and TOTAL.

Special thanks go to Tim Fasnacht, Knut Kvien, William Chesters, and Dr. Torres-Verdin, primary contributors to and co-authors of all of the publications associated with the research described in this dissertation.

Amanda Masterson provided constructive editorial feedback that improved the final version of the manuscript.

I would like to thank the students at the Formation Evaluation Research Group, especially Maika Gambus for her valuable help with the less "geo" and more "engineering" stages of the research work.

Last but not least, I would like to thank my friends Jacinto Lopez, Roque Hernandez, and Luis Rangel for their acquaintance and tremendous support with technologic and logistic issues.

Spatial Delineation, Fluid-Lithology Characterization, and Petrophysical Modeling of Deepwater Gulf of Mexico Reservoirs through Joint AVA Deterministic and Stochastic Inversion of 3D Partially-Stacked Seismic Amplitude Data and Well Logs

Publication No._____________

Arturo Javier Contreras, Ph.D.
The University of Texas at Austin, 2006

Supervisor: William L. Fisher
Co-Supervisor: Carlos Torres-Verdin

This dissertation describes a novel Amplitude-versus-Angle (AVA) inversion methodology to quantitatively integrate pre-stack seismic data, well logs, geologic data, and geostatistical information. Deterministic and stochastic inversion algorithms are used to characterize flow units of deepwater reservoirs located in the central Gulf of Mexico. A detailed fluid/lithology sensitivity analysis was conducted to assess the nature of AVA effects in the study area. Standard AVA analysis indicates that the shale/sand interface represented by the top of the hydrocarbon-bearing turbidite deposits generate typical Class III AVA responses. Layer-dependent Biot-Gassmann analysis shows significant sensitivity of the P-wave velocity and density to fluid substitution, indicating that presence of light saturating fluids clearly affects the elastic response of sands. Accordingly, AVA deterministic and stochastic inversions, which combine the advantages of AVA analysis with those of inversion, have provided quantitative information about the lateral continuity of the turbidite reservoirs based on the interpretation of inverted acoustic properties and fluid-sensitive modulus attributes (P-Impedance, S-Impedance, density, and LambdaRho, in the case of deterministic inversion; and P-velocity, S-velocity, density, and lithotype (sand-shale) distributions, in the case of stochastic inversion).

The quantitative use of rock/fluid information through AVA seismic data, coupled with the implementation of co-simulation via lithotype-dependent multidimensional joint probability distributions of acoustic/petrophysical properties, provides accurate 3D models of petrophysical properties such as porosity, permeability, and water saturation. Pre-stack stochastic inversion provides more realistic and higher-resolution results than those obtained from analogous deterministic techniques. Furthermore, 3D petrophysical models can be more accurately co-simulated from AVA stochastic inversion results. By combining AVA sensitivity analysis techniques with pre-stack stochastic inversion, geologic data, and awareness of inversion pitfalls, it is possible to substantially reduce the risk in exploration and development of conventional and non-conventional reservoirs.

From the final integration of deterministic and stochastic inversion results with depositional models and analogous examples, the M-series reservoirs have been interpreted as stacked terminal turbidite lobes within an overall fan complex (the Miocene MCAVLU Submarine Fan System); this interpretation is consistent with previous core data interpretations and regional stratigraphic/depositional studies.

Table of Contents

List of Figures

List of Tables

Chapter 1: Introduction

This study describes a novel methodology for quantitative reservoir characterization based on the integration of 3D partially-stacked seismic amplitude data, well-logs, geostatistical information, and geologic data into high-resolution 3D lithologic and elastic/petrophysical reservoir models. It also illustrates the successful application of this approach to the spatial delineation and fluid/lithology characterization of Miocene hydrocarbon reservoirs in the central Gulf of Mexico, one of the most active exploration targets in the deepwater Gulf Basin.

1.1 PROBLEM STATEMENT

The central goal of geophysical reservoir characterization is to provide accurate quantitative descriptions of the static properties of a reservoir. Assessment of the lateral continuity of lithologic and fluid units away from wells and the estimation of inter-well petrophysical properties are the central topic of this dissertation. Geophysical inverse theory provides an adequate mathematical framework to infer model parameters from physical measurements of the model's behavior (Menke, 1989; Sen and Stoffa, 1995; Tarantola, 2005). In petroleum applications, in-situ measurements of reservoir properties are difficult to perform due to limited spatial accessibility. Most of the reservoir properties are then inferred from indirect measurements (e.g., well logs, seismic data). Wireline logs and core data are routinely used to estimate petrophysical properties in the vicinity of existing wells (Bassiouni, 1994). Well-log data possess high vertical resolution , but quite often well locations are sparsely distributed within the reservoir. This causes the corresponding petrophysical properties to be statistically biased and hence to be rarely representative of the spatial variability within the reservoir. However, this is often overlooked in practical reservoir characterization projects since the well-log data are a primary source of rock and fluid properties. By contrast, seismic surveys are carried out on a surface grid to infer a three-dimensional (3D) distribution of elastic properties (Brown, 1999). The seismic acquisition process embodies a dense lateral coverage of measurements; however, relatively low vertical resolution (anywhere between 5 and 25 m) is the most prominent disadvantage of seismic data (Liner, 1999).

In the past, post-stack seismic data have been used to fill the spatial gap between sparse well locations (Torres-Verdin et al., 1999). However, post-stack seismic data respond to acoustic impedance (the product of bulk density and P-wave velocity) and, therefore, cannot always uniquely discriminate between spatial variations of porosity, layer thickness, shale concentration, and fluid saturation. Pre-stack seismic data, on the other hand, are sensitive to S-wave velocity and bulk density in addition to P-wave velocity. This provides additional degrees of freedom to uniquely interpret lateral variations of seismic amplitude in terms of variations of petrophysical properties and flow-unit thickness.

1.2 SCOPE AND OBJECTIVES

The main purpose of this research is to develop a novel methodology for quantitative reservoir characterization based on the implementation of state-of-the-art seismic inversion techniques that truly integrate pre-stack seismic amplitude data, well-log data, geologic models, and geostatistical information.

1.2.1 Primary Objectives

- To apply the novel methodology to deepwater hydrocarbon reservoirs in the central Gulf of Mexico with emphasis on reservoir delineation and fluid/lithology characterization.
- To determine specific sand body dimensions and geometries, and increase understanding of the factors controlling hydrocarbon distribution.
- To assess the lateral extent of lithology and fluid units away from wells and estimate inter-well petrophysical properties.
- To quantify the effect of data- and algorithm-dependent factors on the accuracy of the inversion results through detailed sensitivity analyses.

1.2.2 Secondary Objectives

- To assess the nature of AVA effects in the study area.
- To determine the sensitivity of elastic properties to changes in lithology, fluid content, and petrophysical properties.
- To quantify the uncertainty in the lithologic and petrophysical models.
- To geologically interpret the inversion results within the framework of a consistent depositional model.

1.3 METHODOLOGY

To accomplish the above objectives, we first conducted a detailed Amplitude Versus Angle (AVA) fluid/lithology sensitivity analysis. Then we considered two different procedures to construct spatial distributions of reservoir properties, namely,

(1) Deterministic Inversion: using the "Amplitude Versus Angle Constrained Sparse Spike Inversion" algorithm (chapters 2 and 3), and

(2) Stochastic Inversion: using the "Amplitude Versus Angle Markov Chain Monte Carlo" inversion algorithm (chapters 4 and 5).

1.4 STUDY AREA AND INTERVAL OF INTEREST

This dissertation is focused on the analysis of deepwater hydrocarbon reservoirs in Anadarko's Marco Polo Field, which is located in Block 608, Green Canyon area, central Gulf of Mexico, approximately 280 km south of New Orleans, underlying a 1300-m water column (Figures 1.1 and 1.2).

Hydrocarbon production originates from reservoirs consisting of Tertiary deepwater sand deposits. We are specifically concerned with a small portion of the Marco Polo Field where hydrocarbon-bearing sands pertain to the "M" series and are buried at depths between 3500 and 3800 m (Figures 1.3 and 1.4).

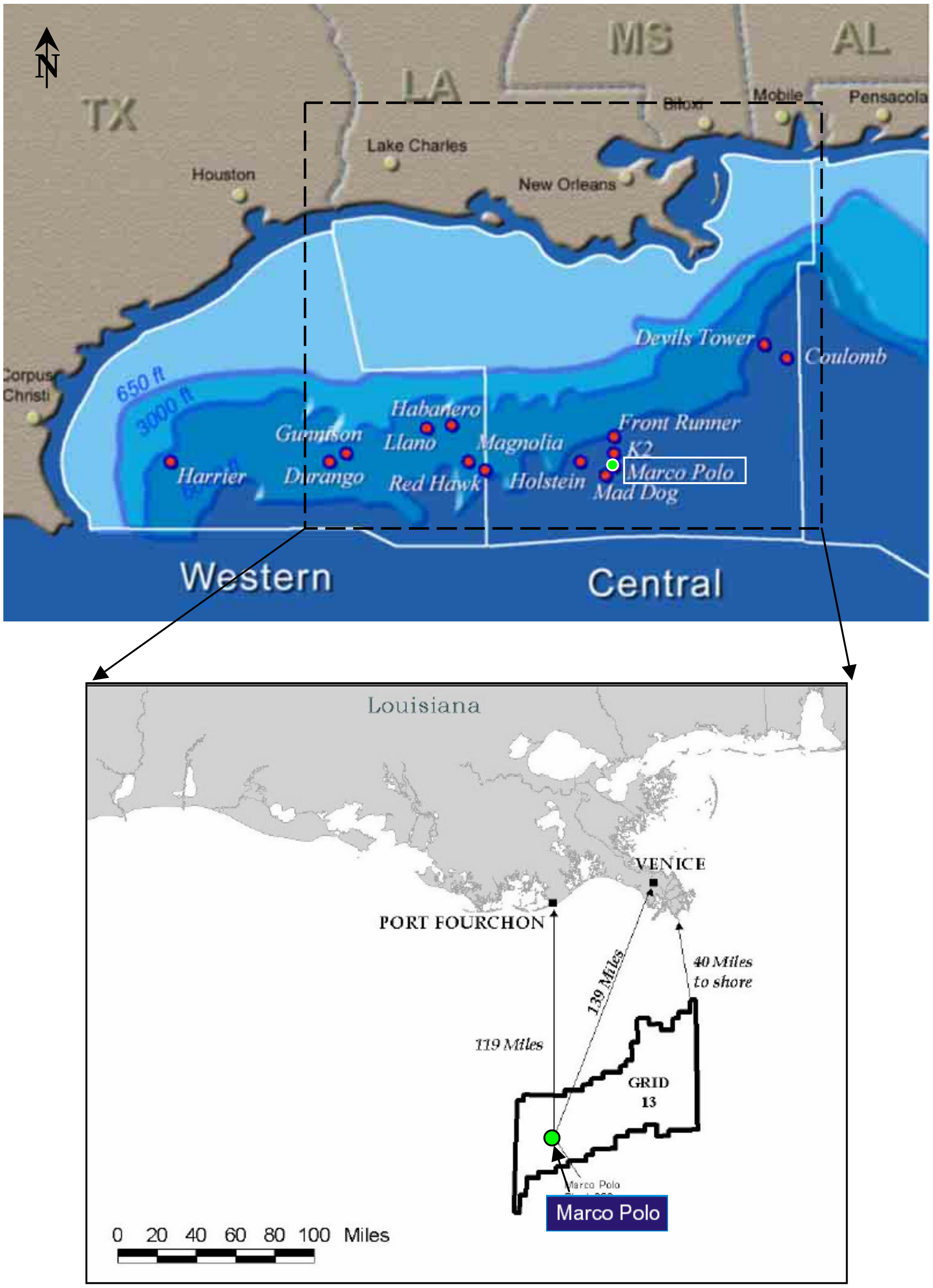

Figure 1.1: Geographic location of the Marco Polo Field among major deepwater GOM fields. Anadarko's Marco Polo deepwater development project is located in Green Canyon Block 608 in the Gulf of Mexico.

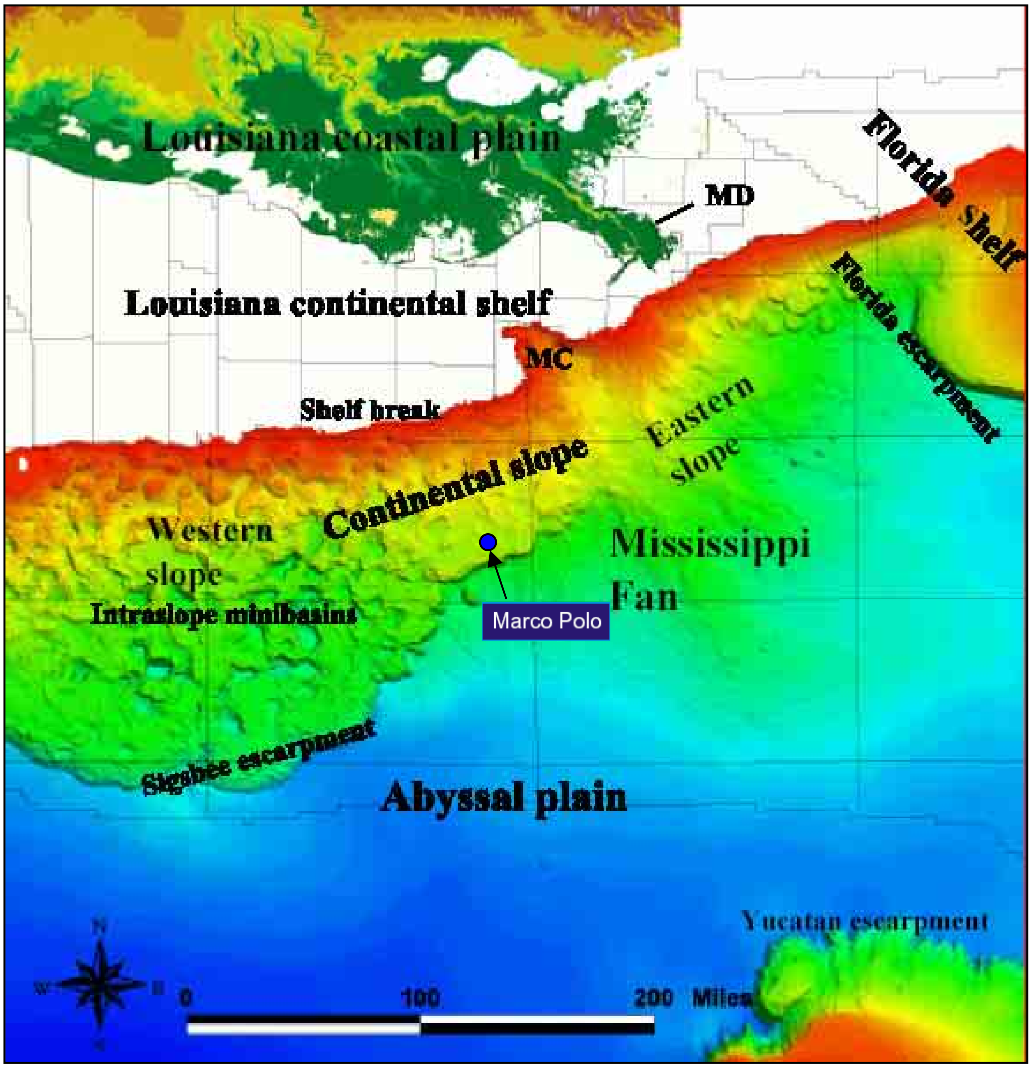

Figure 1.2: Physiographic map of the east-central Gulf of Mexico showing the location of the Marco Polo Field. (MD Mississippi Delta, MC Mississippi Canyon) (Modified from Combellas, 2003).

1.5 DATA SET

The data set used in this study consisted of volumes of post- and pre-stack seismic amplitude data, wireline logs for 12 wells, core data for 4 wells, 1 migration velocity field, 1 check-shot table, and 3 horizons corresponding to the tops of the main reservoir sands. The 3D survey in the Marco Polo Field consisted of 254 cross-lines spaced at 25-m intervals (6.35 km), and 320 in-lines spaced at 20-m intervals (6.4 km). This generated 81,280 traces over an area of approximately 40.64 km^2 (Table 1.1; Figures 1.3 and 1.4).

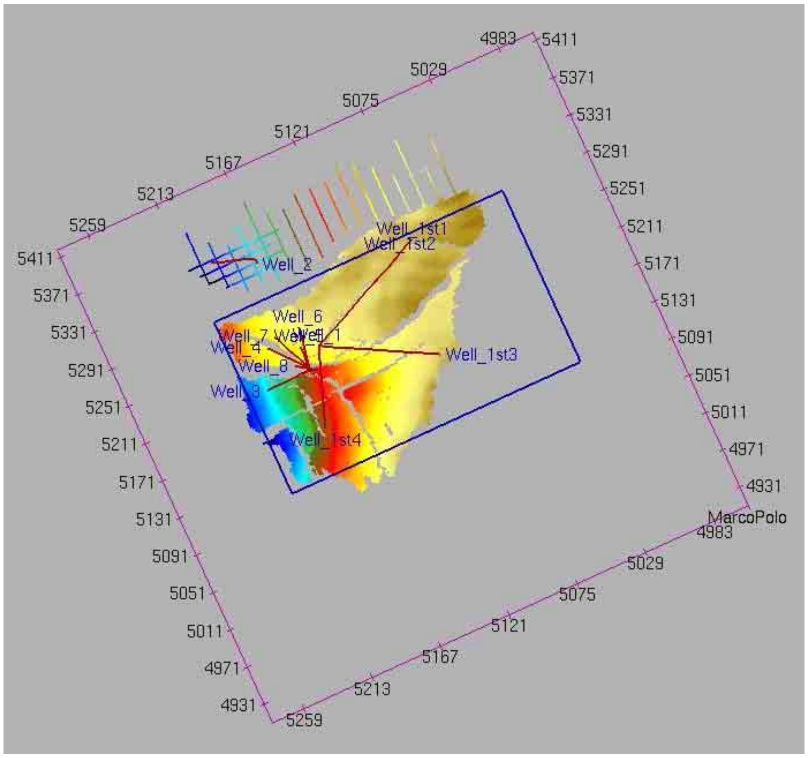

Figure 1.3: Basemap of the Marco Polo Field with structural map in time for the top of the uppermost (M-10) reservoir sand. Red lines represent well trajectories. Blue box indicates area of interest.

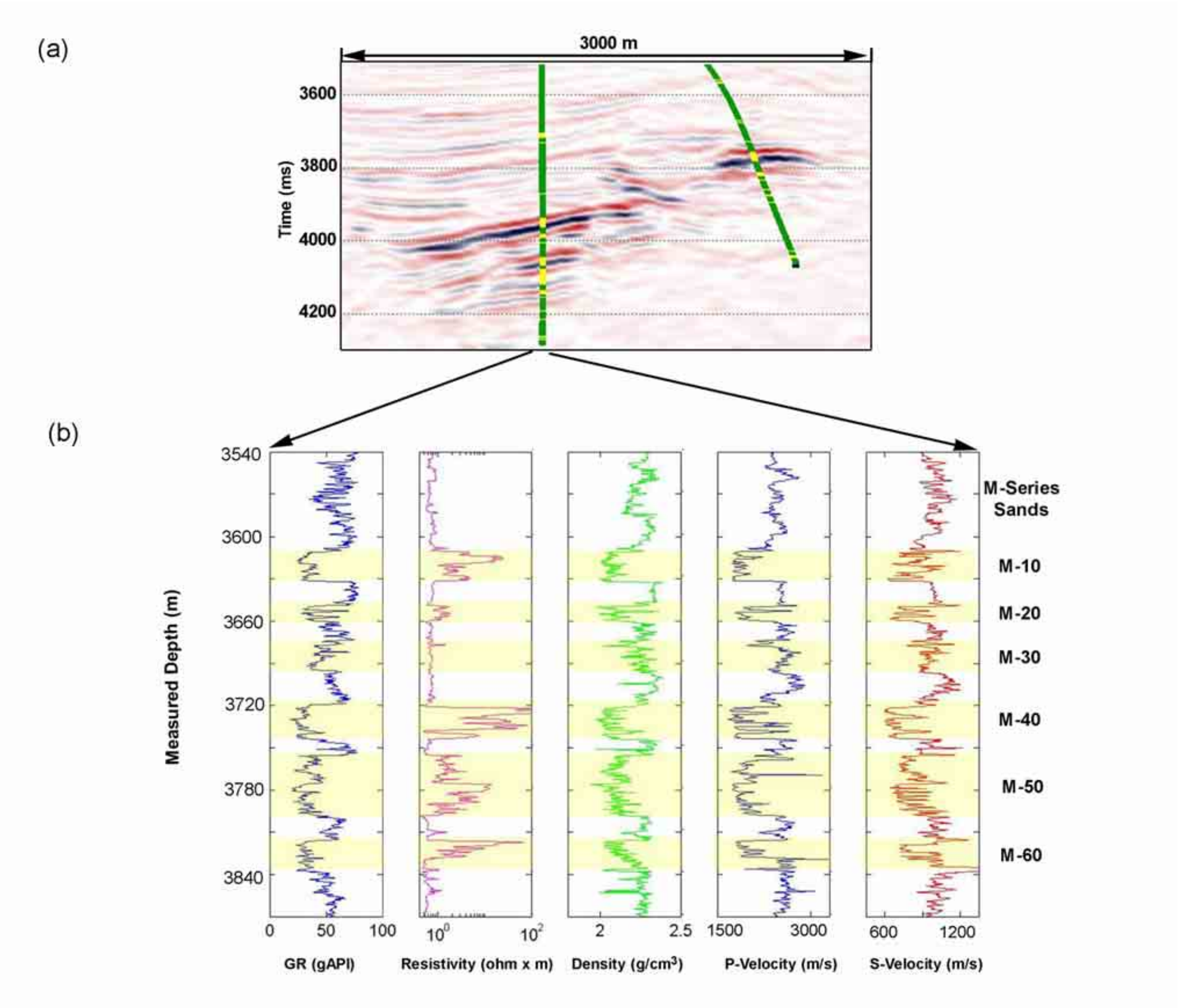

Figure 1.4: (a) Seismic cross-section in time with lithotype well logs indicating the vertical interval comprised by the M-series sands (yellow).
(b) Example of wireline logs acquired in the vertical control well shown in Panel (a). Well-log measurements evidence the characteristic low density, P-velocity, and S-velocity values of the hydrocarbon-bearing M-series sands.

Table 1.1: Summary of the measured seismic data parameters used in this study.

SEISMIC PARAMETER	**VALUE**
Number of In-lines	320
In-Line Separation	20 m
In-Line Length	6.4 km
Number of Cross-lines	254
Cross-Line Separation	25 m
Cross-Line Length	6.35 km
Total Number of Traces	81.280
Survey Area	40.64 km^2
Seismic Time Range	0 – 5 s
Time Sampling Interval	4 ms
Frequency Range	6 – 70 Hz
Central Frequency	28 Hz
Average P-wave velocity	8404 ft/s

1.6 GULF OF MEXICO BASIN EVOLUTION

The north-central Gulf of Mexico basin is a divergent margin basin in which most of the basement subsidence related to plate tectonics had ceased by Tertiary time, leaving a deep marine environment over much of its area (Buffler, 1991). The Gulf of Mexico basin originated with a brief period of rifting during the late Triassic to early Jurassic (Buffler and Sawyer, 1985) (Figure 1.5). This rifting was followed by an extended period of thermally induced subsidence during the mid-Jurassic to early Cretaceous, accompanied by deposition of basinal evaporates (Louann and equivalent salt in the northern Gulf) and carbonates around the periphery of the Gulf basin. A subsequent rapid sea-level fall capped this early Gulf section with a prominent unconformity called the Mid-Cretaceous Sequence Boundary or MCSB (Buffler, 1991). Carbonate production ceased as a rapid basinwide flooding drowned the early Cretaceous margin (Buffler and Sawyer, 1985; Winker and Buffler, 1988). The later period began with a switch from carbonate-dominated to clastic-dominated deposition. In the late Cretaceous, clastic progradation beyond the lower Cretaceous shelf margin was achieved only by stable, mud-dominated systems (Winker, 1982). It was not until the Paleocene that the first, large, sandy deltas prograded into the northwestern Gulf during lower Wilcox deposition (Fisher and McGowen, 1967; Winker, 1982). Offshore Texas continued to be the focal point for pulses of clastic sediments prograding into the Gulf through the early Miocene (Winker, 1982; Galloway et al., 2000). During the Miocene, the main depocenter migrated east from offshore Texas to offshore Louisiana (Woodbury et al., 1973; Winker, 1982; Winker and Booth, 2000). This coincided with the ancestral Mississippi and Tennessee Rivers becoming the dominant drainage systems for the northern interior (Galloway et al., 2000). Pliocene and Pleistocene depocenters then continued to prograde not only seaward, but also westward, from the Miocene shelf edge (Woodbury et al., 1973; Winker, 1982; Winker and Booth, 2000).

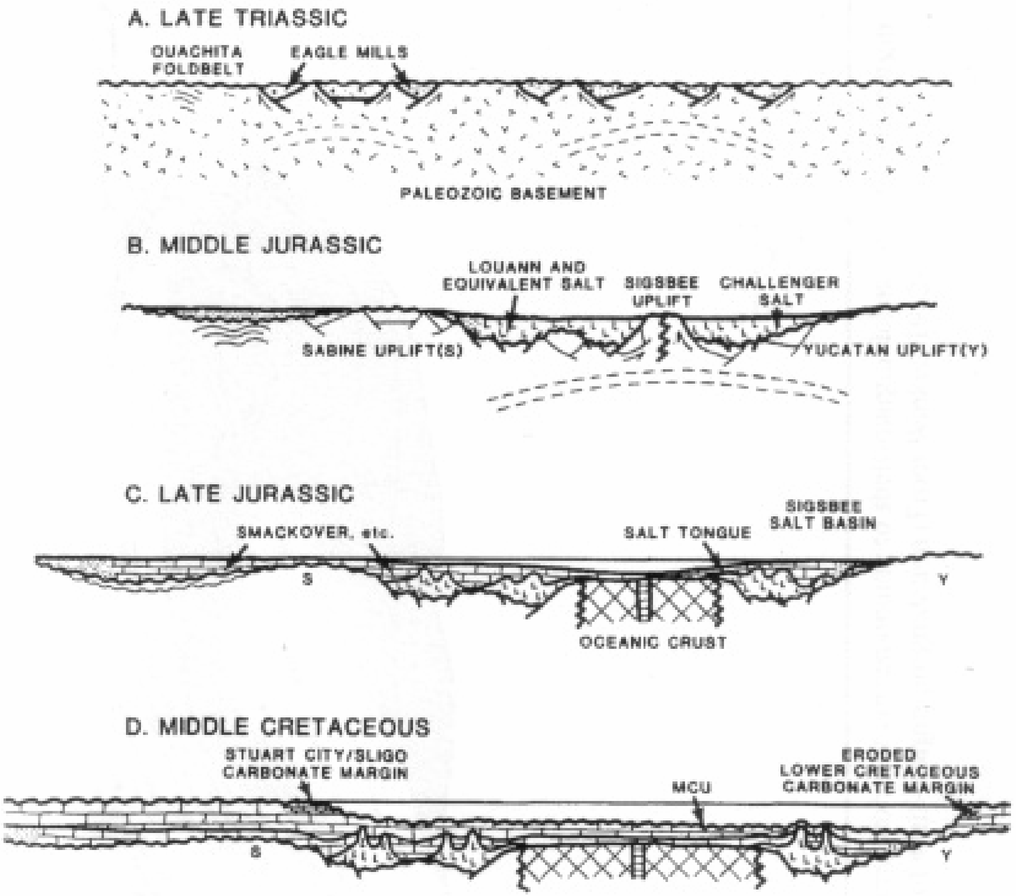

Figure 1.5: The pre-MCSB evolution of the deep Gulf of Mexico basin (From Buffler and Sawyer, 1985).

1.7 CENOZOIC DEPOSITIONAL HISTORY

The Cenozoic depositional history of the GOM basin is the product of the complex interactions among sediment supply, salt-influenced gravity tectonism, relative sea-level change, and subsidence. The GOM Miocene stratigraphic record reveals this complex interaction. Galloway et al. (2000) summarize the depositional history of the northern Cenozoic GOM. Major conclusions of this work are:

1. Principal depositional episodes of the GOM basin Cenozoic are recorded in 18 basinwide genetic stratigraphic sequences bounded by major MFS.

2. High rates of sediment supply and extensive progradation characterized most depositional episodes of the Cenozoic. The basin margin has prograded 150-180 miles from its relict Cretaceous position.

3. Three major depositional systems tracts composed the genetic sequences (Figure 1.6).

4. The widespread progradational offlap during the episodes of basin fill was interrupted by brief but intense periods of retreat, submarine erosion, and starvation. Major, localized continental margin failures are common products of these periods of retreat and submarine erosion, which nucleate submarine canyons, megaslides, and autochthonous aprons. These areas of mass wasting and gravity-dominated flows bypassed sediments to the basin floor.

5. Localized structural displacement radically affects the continuity of the sediment dispersal system and depositional facies. Salt tectonics plays a major role in the GOM, where complex interactions between sediment loading and salt

deformation from different structural provinces then affect, in turn, the configuration and evolution of the depositional systems.

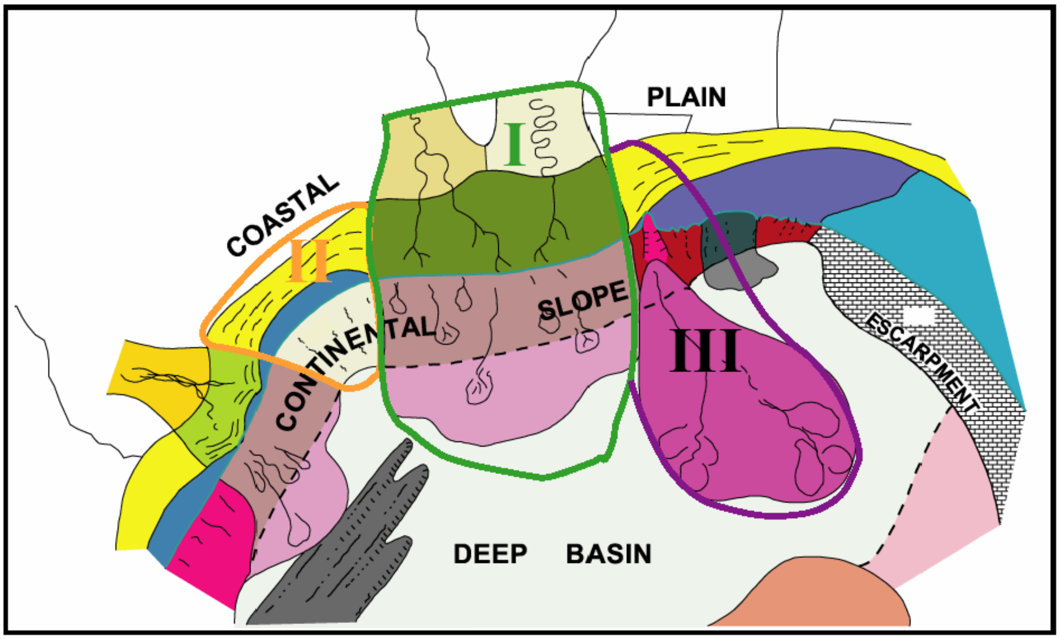

Figure 1.6: Schematic map of the typical depositional systems and systems tracts present in the Cenozoic GOM basin. I. Fluvial, delta, delta-fed apron systems tract. II. Coastal plain, shore zone, shelf, shelf-fed apron. III. Delta flank, submarine fan system tract (Modified from Galloway et al., 2000).

1.8 MIOCENE DEPOSITIONAL HISTORY

During the lower Miocene, the ancestral Mississippi delta was established in southwestern Louisiana (Rainwater, 1964). Reactivation of the southern Rocky Mountains, the Colorado Plateau, Cumberland Plateau, and the Appalachian Mountains is related to the consolidation of the ancestral Mississippi delta (Rainwater, 1964; Meyerhoff, 1968; Winker, 1982). From the early to late Miocene the ancestral Mississippi delta shifted eastward to southeastern Louisiana (Curtis, 1970).

The Middle Miocene depostional episode is characterized by the presence of the following systems tracts (Figure 1.7) (Galloway et al., 2000).

1. Mixed-load fluvial, central fluvial-dominated delta, delta-fed apron systems tract.
2. Mixed-load fluvial, east wave-dominated delta, MCAVLU submarine fan systems tract.
3. Texas-Louisiana shore zone, shelf, muddy shelf-fed apron.
4. Louisiana-Mississippi shore zone, shelf, muddy shelf-fed apron.

The central fluvial-dominated delta prograded rapidly to the shelf margin, in contrast with east wave-dominated delta, where along-strike sediment reworking delivered sediments parallel to the continental platform. Deltaic offlap wedges formed extensive delta-fed aprons (Galloway et al., 2000).

The two strike-fed systems tracts lay at the flanks of the delta depositional systems (Figure 2.2). Sand-rich shore zones and mud-dominated clastic shelves characterized both depositional systems tracts (Galloway et al., 2000).

A displaced major submarine fan system, the MCAVLU Fan, formed in the east-central basin floor (Figure 1.7). The MCAVLU fan forms a sandy depositional element encased in the muddy basin floor sediment. A major depositional facies of this system is channelized turbidite lobe deposits of a muddy turbidite system (Feng, 1995; Galloway et al., 2000). Origin of the MCAVLU fan is unknown due to the absence of evident submarine canyons. Galloway et al. (2000) proposed that slope bypassing was favored by a narrow, steep northeast Gulf slope.

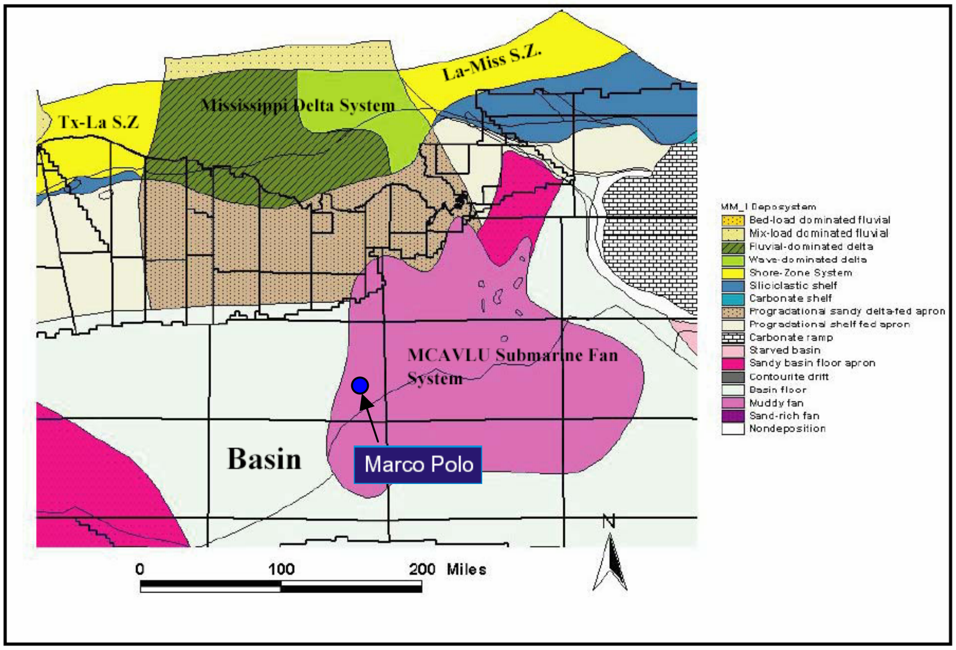

Figure 1.7: Principal depositional systems interpreted in the Middle Miocene depositional episode in the east-central GOM basin. Two major depositional systems are present. The fluvial-dominated delta system in the coastal plain-shelf is one, the MCAVLU submarine fan system in the basin center is the other. Tx-La S.Z. Texas-Louisiana shore zone, La-Miss S.Z. Louisiana-Mississippi shore zone (modified from Galloway et al., 2000).

1.9 REGIONAL DEEPWATER STRATIGRAPHIC STUDIES

1.9.1 Middle Miocene MCAVLU Submarine Fan System

Combellas (2003) describes the depositional history and stratigraphic evolution of the Middle Miocene MCAVLU Submarine Fan System, in the east-central Gulf of Mexico. For delineation and characterization, the expansion of the MCAVLU fan system is denoted as unit SS3.

During the deposition of SS3 the MCAVLU fan system grows basinward of a bypass-dominated slope. For the first time two submarine fans are clearly differentiated on the basin floor: the Eastern submarine fan and the Western submarine fan; the well-developed, ancestral Tennessee delta-fed apron sourced the MCAVLU fan system. The fan was dominated by a bypass submarine channel fill facies.

The Marco Polo Field is located in the area corresponding to the Western submarine fan (Figure 1.8). Bypass facies assemblages characterize the western minibasin province. The extensive South Timbalier and salt-stock canopies and the active eastern Mississippi Fan fold belt controlled sediment transport pathways in the slope. The newly established erosional channels incised relict lobe complexes of SS2 in the western, unconfined basin floor.

Principal depositional and seismic facies of the western basin floor are:

1. Erosional channel fills.
2. Small depositional channel fills.

3. Sandy lobes and sheets: wedge, mounded, high-amplitude and high-continuity reflections. Laterally extensive (approximately 70 miles wide by 50 miles long on average), high net to gross lobes and sheets extend onto the western basin floor (Figures 1.8, 1.9, and 1.10).
4. Distal, thin lobes and sheets: divergent, low- and high-amplitude, high continuity reflections.

The well logs display upward-coarsening to blocky sandy units that are interpreted as laterally continuous lobes and sheets (Figure 1.10). Average sand body thickness ranges from 50 to 100 feet.

The western fan is sandier than the eastern fan. Erosional/depositional channels dominate the eastern fan, whereas highly continuous, sandy lobes and sheets are typical facies of the western fan.

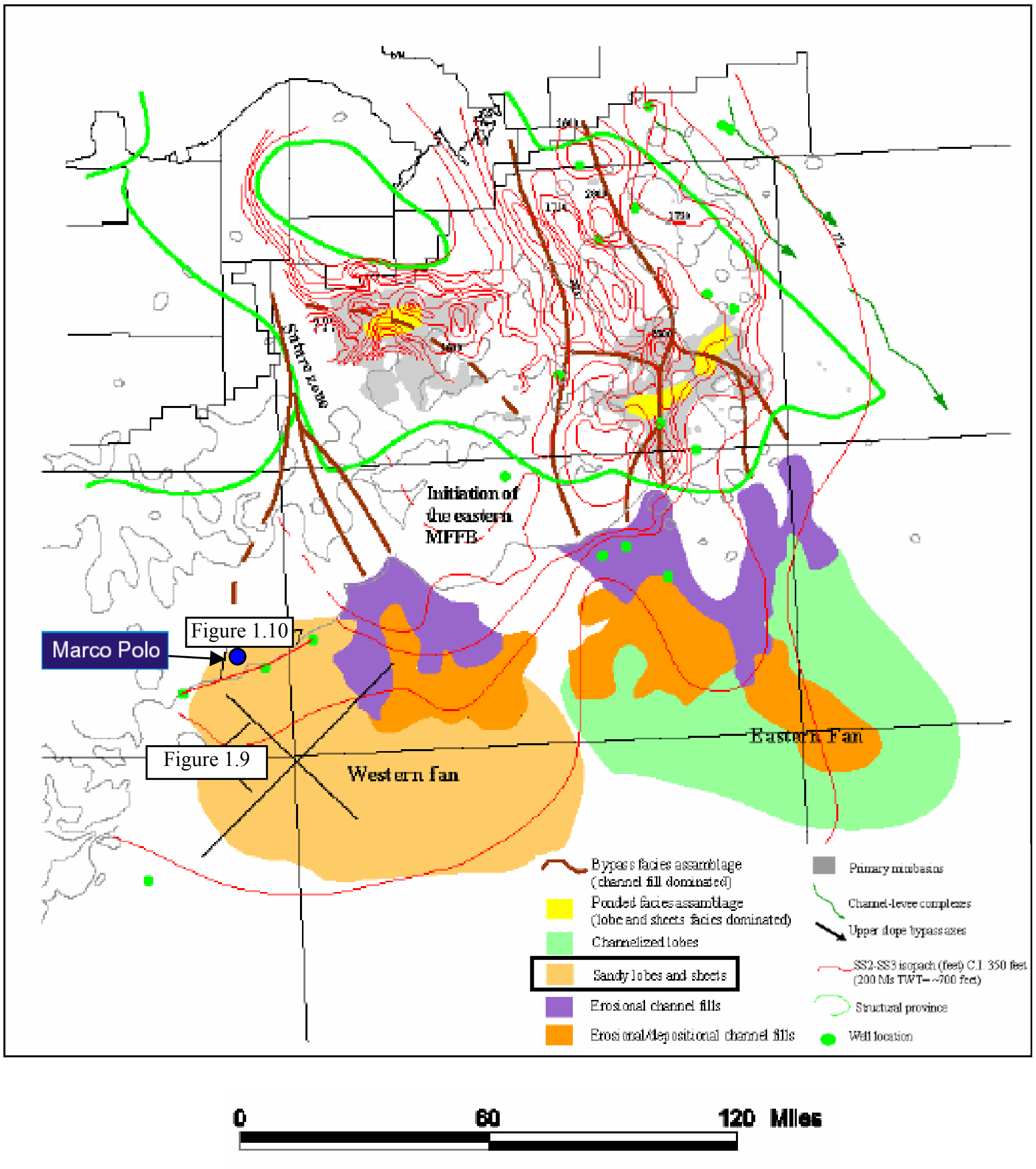

Figure 1.8: SS3 depositional facies map. Eastern and western submarine fan systems expanded in the slope and basin floor. (Modified from Combellas, 2003).

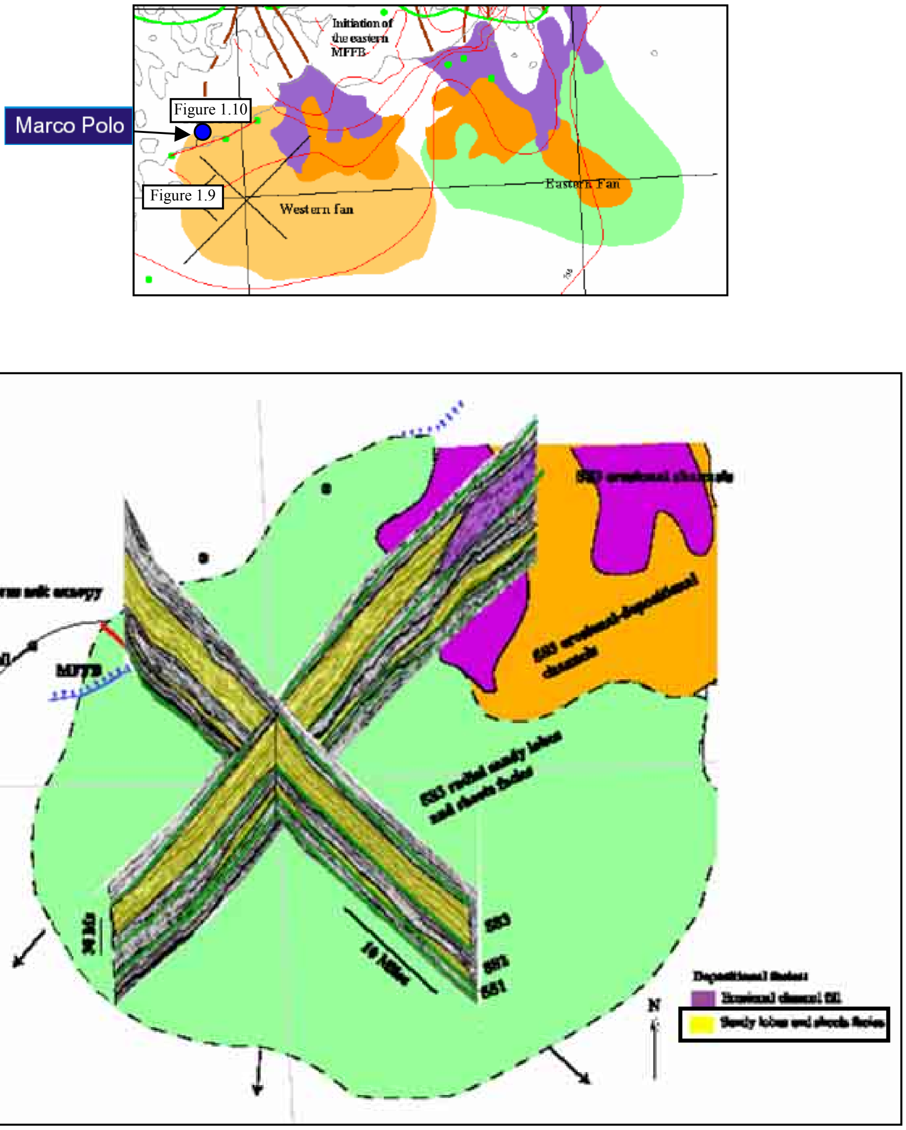

Figure 1.9: Fence diagram showing principal depositional facies based on seismic facies interpretation in the western basin floor (see Figure 1.8 and upper panel for location). Mounded sandy lobes of SS2 are capped by continuous sandy lobes of SS3. (Modified from Combellas, 2003).

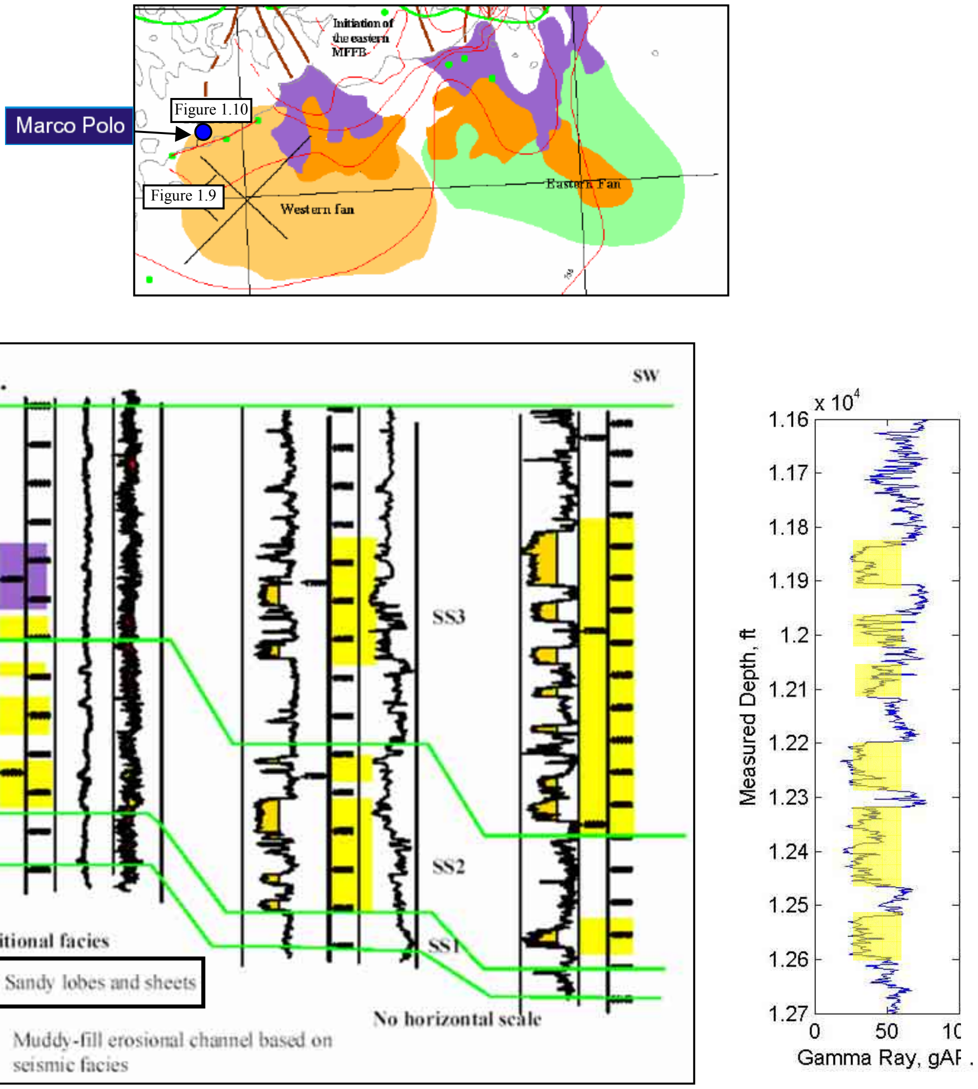

Figure 1.10: Well-log cross-section through the western unconfined basin floor (see Figure 1.8 and upper panel for location). Thick upward-coarsening to blocky sandy lobes and sheets characterize SS2 and SS3. Compare to typical log signature of the M-series reservoir sands (right panel). (Modified from Combellas, 2003).

1.9.2 Upper Miocene MCAVLU Submarine Fan System

Wu (2004) describes the depositional history and stratigraphic evolution of the Upper Miocene MCAVLU Submarine Fan System in the East-Central Gulf of Mexico, mainly based on the work by Galloway et al. (2000) in the Gulf Basin Depositional Synthesis (GBDS) project.

The upper Miocene paleography is characterized by the composite fluvial-dominated paleo-Tennessee and Mississippi River delta system, its sandy, delta-fed central Gulf slope apron and the adjacent deep Gulf MCAVLU submarine fan, as defined by Galloway et al. (2000), (Figure 1.11).

The upper Miocene deepwater depositional systems in the east central Gulf of Mexico included in the linked self-margin deltas, the slope apron, containing the western slope canyon complex and the eastern intra-slope MCAVLU fan and related channels, and the abyssal MCAVLU submarine fan system, where the Marco Polo Field is located (Wu, 2004; Figure 1.12). The map of the abyssal plain MCAVLU is based on the original results of the GBDS project (Galloway et al., 2000). This huge basin floor fan represents focused allochthonous sediment accumulation on the basin floor and is interpreted to have been supplied by the confluence of a variety of sources, including the western slope canyon system, the overflow from eastern intraslope McAVLU fan systems, the eastern canyon, and possibly the sandy slope apron. The accumulation of a regional sandy fan in the deep basin suggests that, despite the broad, bathymetrically complex slope dominated by salt tectonism, long-term sediment supply was sufficient to repeatedly overflow the topographic obstruction and bypass to the abyssal plain.

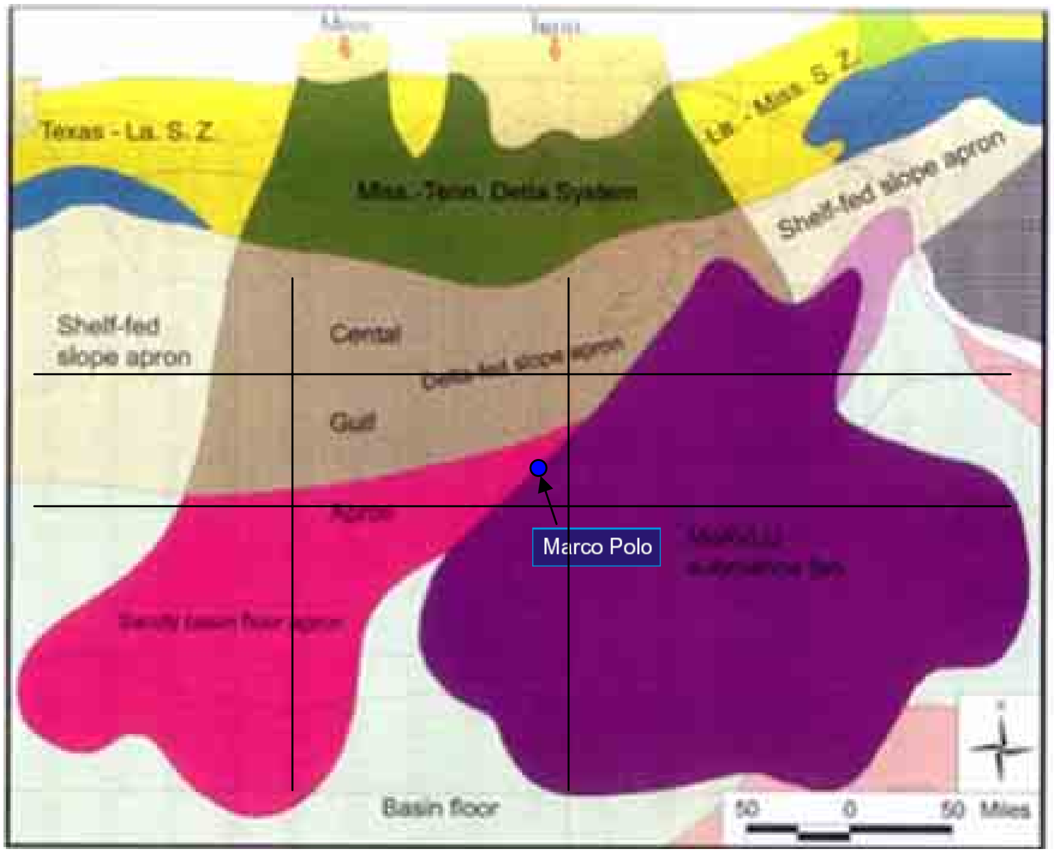

Figure 1.11: Upper Miocene paleography as defined by Galloway et al. (2000). The East-Central GOM was characterized by the composite fluvial-dominated paleo-Tennessee and Mississippi River delta system, its sandy, delta-fed central Gulf slope apron and the adjacent deep Gulf MCAVLU submarine fan. Miss = Mississippi, Tenn = Tennessee, S.Z. = Shore zone. (Modified from Wu, 2004).

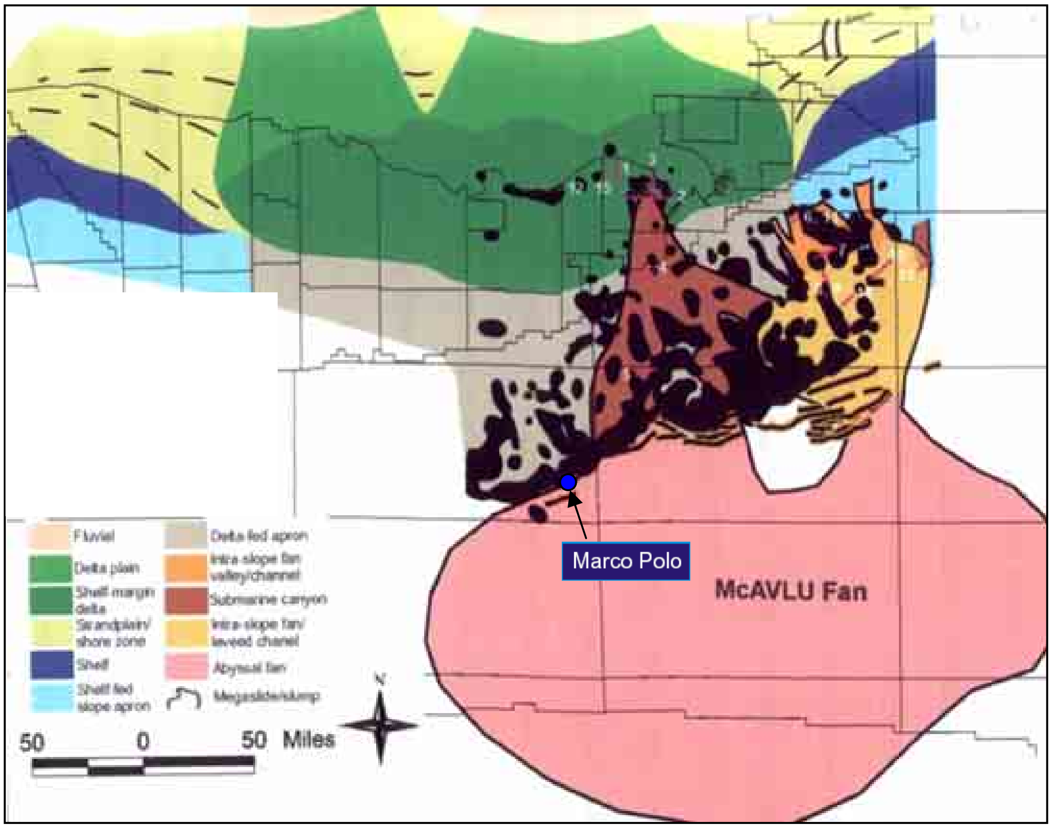

Figure 1.12: The upper Miocene deepwater depositional systems in the east-central Gulf of Mexico included the linked self-margin deltas, the slope apron, containing the western slope canyon complex and the eastern intra-slope MCAVLU fan and related channels, and the abyssal MCAVLU submarine fan system, where the Marco Polo Field is located.

1.10 PETROLEUM RESOURCES

The Gulf of Mexico basin is one of the three petroleum megaprovinces in the world, and Miocene sandstones are the single most important producing unit (Figure 1.13) (Nehring, 1991). As of the end of 1987, known recovery in the Miocene was 148 trillion cubic feet of natural gas, 18.45 billion barrels of crude oil, and 5.55 billion barrels of natural gas liquids. The Miocene alone contains 21.9% of the oil-equivalent petroleum resources of the Gulf of Mexico basin. Upper Miocene production is dominated by a major deltaic oil and gas trend straddling the southeast Louisiana coast, with nearly 40% of all Miocene known recovery. Upper Miocene reservoirs in south Louisiana occur across a very extensive depth range from -950 to -18,000 ft (-300 to -5400 m). Reservoir thicknesses are generally 15 to 300 ft (5 to 100 m). Reservoir quality in these sands is good to excellent, with porosity generally ranging from 20% to 35% and permeabilities from 50 to 2500 md. The great productivity of the central Gulf of Mexico Upper Miocene results primarily from the presence of extremely large volumes of high-quality sandstone reservoirs. The rapid, large-volume sedimentation that produced Upper Miocene reservoirs also resulted in subsequent movement of underlying salt and the creation of numerous growth faults and salt-cored structures, the two major mechanisms of trap formation in the Upper Miocene. Local and regional seals, formed by transgessive shales, are also common throughout the Upper Miocene section. There are large volumes of Paleogene and Mesozoic source rocks. Although the quality of the Paleogene and Mesozoic source rocks is only fair to good because of a high sedimentation rate, and therefore low proportion of total organic matter, extensive migration has charged numerous, commonly multistory reservoirs. Together, juxtaposition of good to excellent reservoir, migration, trap, and seal elements has led to the highly efficient trapping of petroleum in the Upper Miocene genetic sequence.

Most of the deep-water (>15,000 ft) GOM remained unexplored until the 1990's, when massive exploration campaigns were conducted by major oil companies. Large Miocene deepwater discoveries and reserves have subsequently been found in the east-central GOM, including the giant fields Thunder Horse (>1,000 million BOE), Atlantis (~400 to 800 million BOE), Mad Dog (~200 to 450 million BOE), and Champlain (>100 million BOE). Estimated potential of 10,000 million BOE remains in deepwater reservoirs for the next generation (Rain and Meyer, 2001).

The combination of good reservoir quality, structural and stratigraphic traps, and mature source rocks makes the Miocene one of the most prolific intervals in the deepwater GOM. Principal traps include subsalt turtle structures associated with inverted primary minibasins, compressional folds associated with the Mississippi Fan Foldbelt (MFFB), subsalt, compressional, high-relief folds related with the MFFB, and combined structural and stratigraphic traps along the Lower Cretaceous shelf margin and diapir-salt flanks. Source rocks are mainly Upper Jurassic and Lower Cretaceous marine marls (Colling et al., 2001).

Modern seismic data often generate new ideas leading to surges in leasing and drilling activity. Figure 1.13 illustrates several new deepwater plays in the GOM. Although the traditional mini-basin plays are far from mature (especially considering the recently announced Crazy Horse discovery in Mississippi Canyon Block 778), the Mississippi Fan Foldbelt, Perdido Foldbelt, and Tertiary Fan/Mesozoic Plays show that the deepwater arena is very much a frontier area. Although sparsely tested, the Mississippi Fan Foldbelt shows great potential with announced discoveries at three locations (prospects Mad Dog in Green Canyon Block 826, Neptune in Atwater Block 575, and Atlantis in Green Canyon Block 699) (Baud et al., 2000).

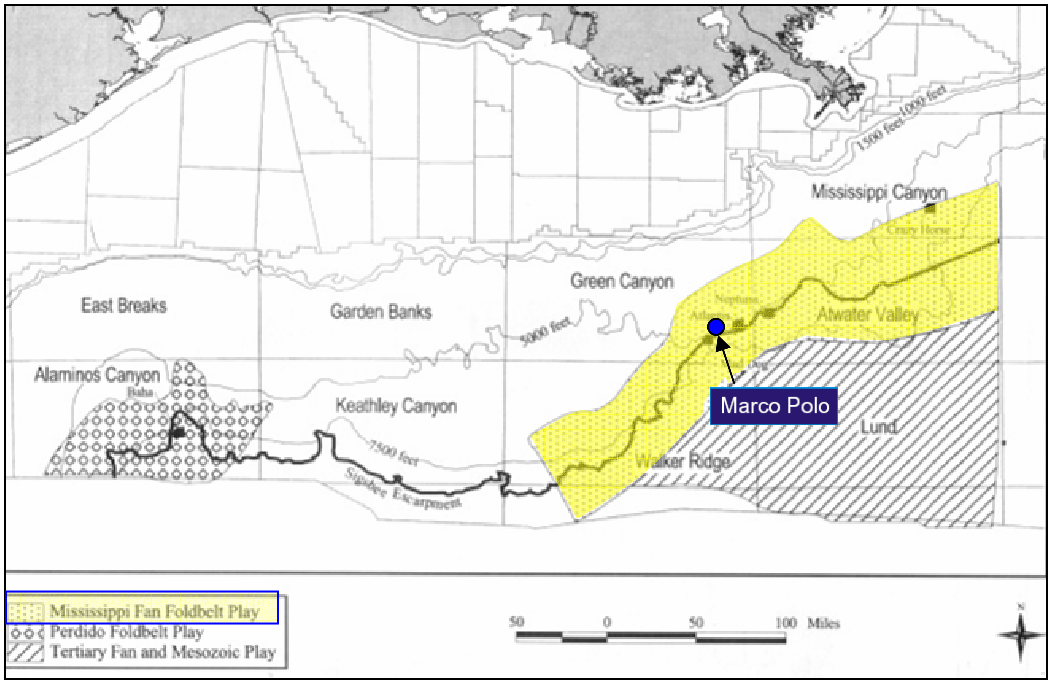

Figure 1.13: New deepwater plays in the Gulf of Mexico including the location of the Marco Polo Field. Although sparsely tested, the Mississippi Fan Foldbelt shows great potential with announced discoveries at three locations: prospects Mad Dog in Green Canyon Block 826, Neptune in Atwater Block 575, and Atlantis in Green Canyon Block 699. (Modified from Baud et al., 2000).

1.11 CORE DATA ANALYSIS OF M-SERIES RESERVOIR SANDS

Anadarko’s internal reports of core data analysis indicate that the “M” series reservoir sands consist of six sand units (M-10 to M-60), in which M-10, M-40, and M-50 are the main reservoir intervals. The overall “M” series have been described as unconsolidated, interbedded high- and low-density fine-grained (mixed sandy-muddy) turbidite deposits. The intervening shale-dominated intervals that separate the main reservoir sand packages are low-density muddy turbidite deposits that have been re-deposited as thick, muddy debris flow/slump deposits (i.e., the overall "M" series consists of sandy turbidite reservoir packages interbedded and separated by muddy debris flows). The lower contacts of the sand beds are generally sharp and planar, with very minor amounts of loading and rare, minor scour. Upper contacts are commonly gradational, with massive and planar stratified, upper very fine to lower fine-grained sands typically capped by climbing ripple-stratified, finer-grained, better sorted sands. Rippled sands, in turn, are overlain by thin, diffuse ripple and planar laminated silts (lower plane beds), invariably capped by normally graded, planar laminated mudstones (i.e., normally graded beds containing complete and very nearly complete Bouma sequences of varying thicknesses). The sandy flows that deposited and compose the main reservoir intervals were strongly depositional and aggradational in character (i.e., waning, depletive flows with very little scour), with the finer muddy portions of the flows typically deposited and preserved as normally graded and laminated drapes.

Bouma "A-B" division (massive and planar stratified) sands dominate the lower M-50 and M-40 packages (gross 126 ft and 41 ft thick, respectively, for the massive sand intervals). Direct evidence of channelization is lacking. Both the M-40 and the lower portion of the M-50 sand packages show upward-thickening and increasingly sandy beds ("coarsening" in a broad sense), consistent with a progradational sequence. These reservoir intervals are interpreted as stacked, progradational lobes within an overall fan complex (terminal lobes/basin floor fan complex). These massive and planar stratified sands have moderate sorting and excellent visible interparticle porosity, with early core analysis data indicating excellent intrinsic properties (30%+ porosity, 10-4000 millidarcies of permeability). Specific sand body dimensions and geometries are still being determined.

The upper portion of the M-50 reservoir series is composed of medium to thin bedded (typically 5-30 cm thick), planar and climbing-ripple laminated sands, with relatively thin, normally graded clay drapes. The thickness of this upper M-50 rippled-sand and mud interval (55 ft), and the unidirectional nature of the ripple-set directions suggest that it could be the lateral equivalent of offset sandier, more thickly bedded fan lobes similar to those described for the lower M-50 and the M-40 interval. Offset lobe shingling is the preferred interpretation for this package at this time as opposed to gradual lobe abandonment, or upstream avulsion (this is inferred due to the absence of upward thinning and fining of beds which would indicate a gradual retreat or switching of sediment source.)

1.12 DEPOSITIONAL MODEL: SLOPE AND BASE-OF-SLOPE SYSTEMS

1.12.1 Channel-Lobe Complexes

Galloway and Hobday (1996) and Galloway (1998) describe the turbidite lobes as one of the slope environments and facies. While not all channels support discrete turbidite lobes at their terminus, the association is quite common. Consequently, the channel-lobe complex forms a basic framework building block of many slope depositional systems. Elements of the complex include a proximal incised channel (and any tributaries), a distal leveed channel, and a terminal lobe, which grades into fine sediments of the basin floor. In an idealized channel-lobe complex, each element is characterized by distinctive depositional geometry, facies associations, textural and bedding successions, and resultant log patterns (Figure 1.14).

The incised channel fill is relatively narrow, lenticular, coarse-grained, and erosionally inset within other slope facies. It may also be plugged with muddy slump debris. Downslope, the depositional channel broadens the isopach belt, with extensive levees and overbank deposits. Channel fill consists of massive, amalgamated, high-density turbidites. As the channel opens out at the slope base, flows expand, depositing agraddational, sandy lobe turbidites.

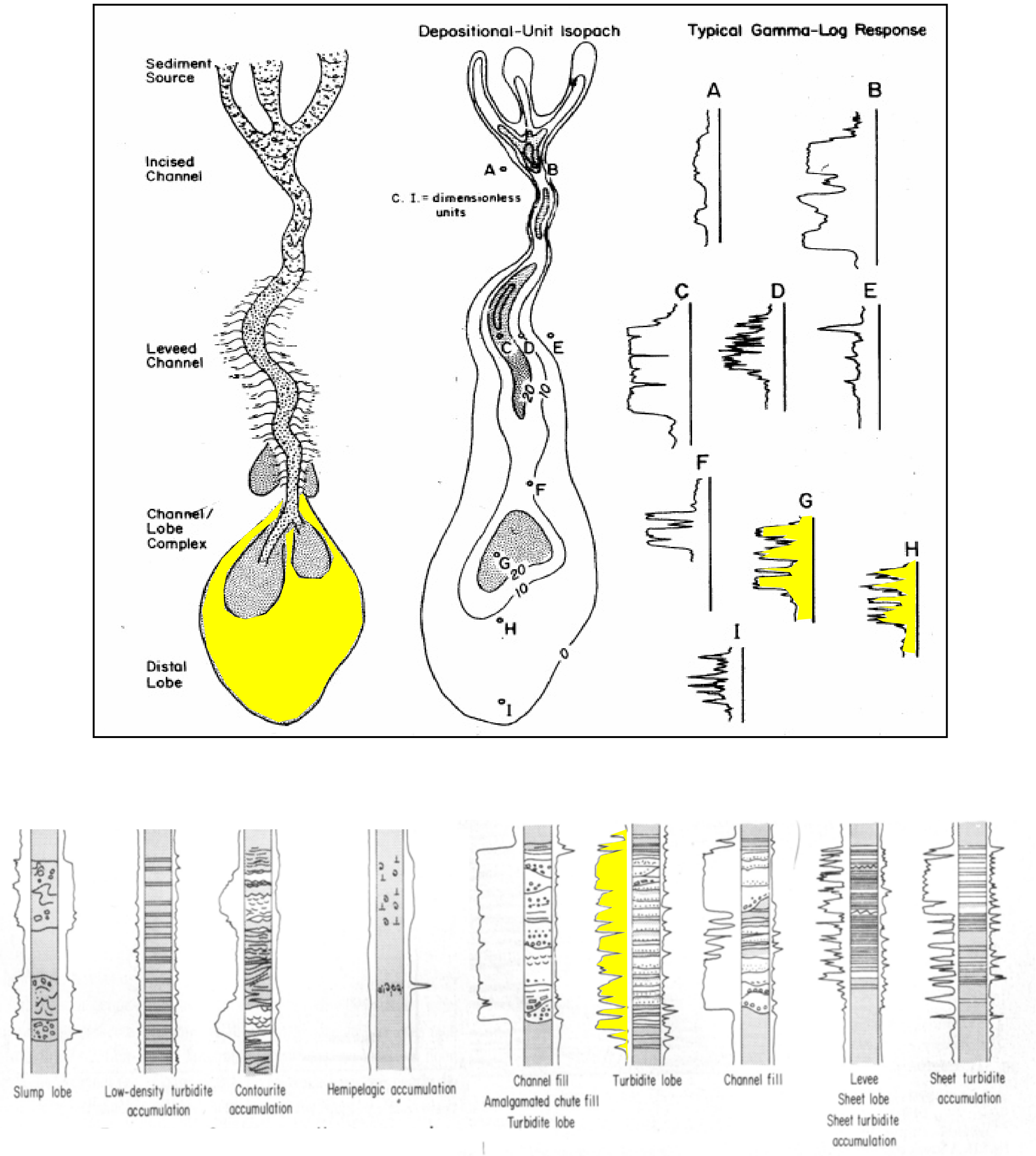

Figure 1.14: (a) Depositional model: Geomorphic elements, depositional unit isopach, and typical log responses of a channel-lobe complex. (Modified from Galloway and Hobday, 1996). (b)Typical vertical facies successions and log responses of slope and base-of-slope facies (Modified from Galloway and Hobday, 1996). Areas highlighted in yellow correspond to the turbidite-lobes interpretation initially suggested by M-series core data analysis.

1.12.2 Turbidite Lobes

The term “lobe” has been used in a variety of ways in fan and turbidite systems (Shanmugam and Moiola, 1988). As illustrated in early key papers on modern and ancient fan systems by Normark et al. (1979) and Mutti and Ricci Lucci (1972), turbidite lobes are spatially localized accumulations of sandy turbidites found at the downstream end of slope channels (Figure 1.16). They record focused aggradation of coarse sediment as turbidity flows spread and decelerate. Coarse-grained, high-density turbidites pile up, forming mounded lobes that have relatively restricted areal distribution and bathymetric relief (suprafan lobes; Normark et al., 1979). More efficient, muddy flow systems disperse sand far into the basin (Mutti, 1992), creating sheet lobes. Sheet lobes are transitional into basin plan sheet turbidites, and in sand-poor systems may spread and lose their identity as a discrete sand body. Creation of lobes requires relatively stable channels to focus multiple flows onto specific sites on the basin floor.

1.12.3 Mounded Turbidite Lobes

Feature of lobes have been summarized by Mutti and Normark (1991) and Mutti et al. (1987) and described in outcrop by Kleverlaan (1989). Mounded lobe facies are rich in sand and gravel and consist of amalgamated coarse-grained turbidites. Scours and low-relief channels may cut through bedded turbidites of the proximal lobe. Mounded lobe sand bodies range from a few meters to many tens of meters in thickness and are typically up to a few kilometers in width. Downflow, thickness, and grain size of turbidite beds decrease rapidly.

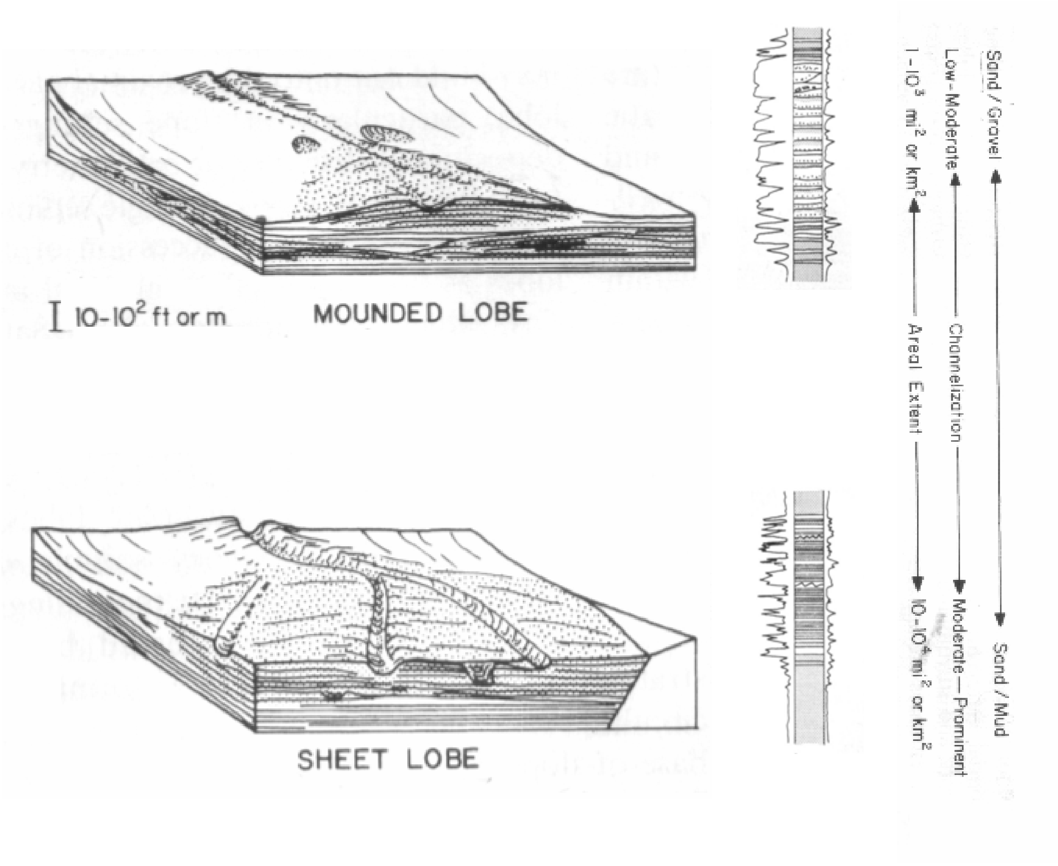

Figure 1.15: Block diagram illustrating the geometry, characteristic, typical vertical facies successions, and log pattern of coarse, sandy and mixed sandy to muddy turbidite lobes. (Modified from Galloway and Hobday, 1996; and Galloway, 1998).

1.13 MODERN AND ANCIENT ANALOGOUS EXAMPLES

1.13.1 Quaternary Navy Fan, California

Modern turbidite fans are represented by the well-studied Navy fan (Normark et al., 1979; Piper and Normark, 1983; Normark and Piper, 1985). Galloway and Hobday (1996) describe the mounded turbidite lobes as one of the component facies of the sandy submarine fans. Mounded turbidite lobes form where channels open out onto a highly aggradational fan plain. Lobes on the Quaternary Navy fan, California (Normark et al., 1979) are 1 to 10 km across and slightly elongate (Figure 1.16). Through time, lobe aggradation causes autocyclic channel avulsion and lobe shifting, forming compensation cycles. Lobes consist of upward-coarsening and thickening or massive, blocky turbidite successions.

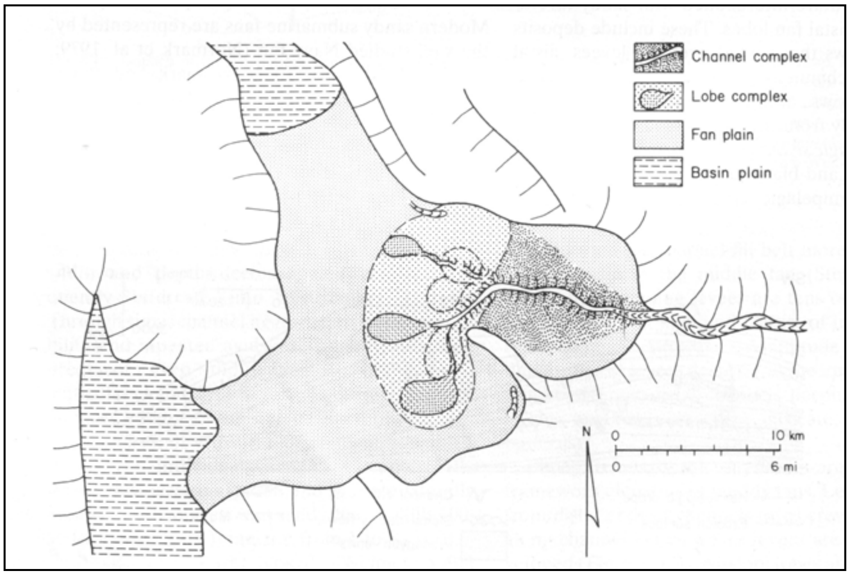

Figure 1.16: Depositional setting, morphology, and environments of the Quaternary Navy fan, California. (From Galloway and Hobday, 1996; Modified from Normark et al., 1979).

1.13.2 Niger Delta Slope, Offshore Nigeria

Pirmez et al. (2000) describe the western Niger delta slope as a complex tectono-sedimentary system, with a number of active structures and submarine channels during the latest Pleistocene (Figure 1.17). Three main channels are illustrated in this 3D seismic image of the seafloor: the X channel to the north, the Y channel to the south, and the Y` channel in the center, a tributary to the Y system. High amplitudes in the image (red/yellow) are interpreted to result from high impedance material near the seafloor; i.e., sand within the channel axes, proximal overbank and depositional lobes, and shallow cemented zones near fluid expulsion features.

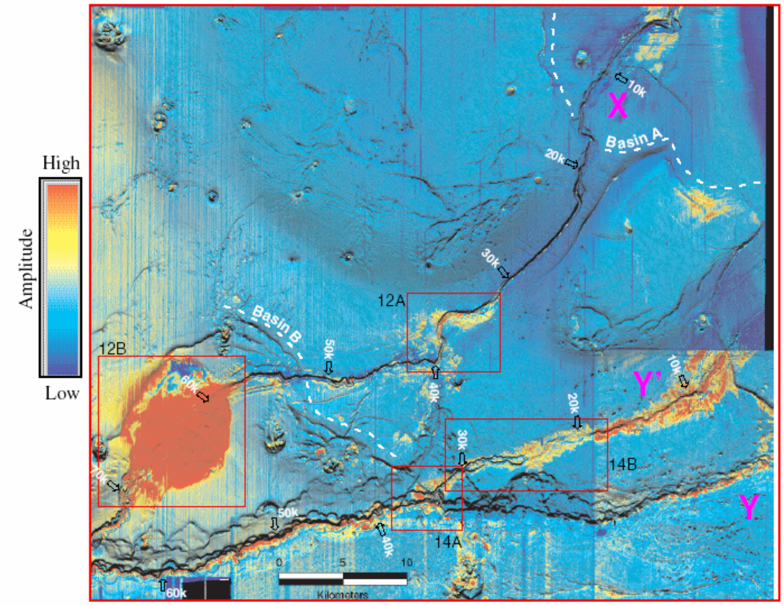

Figure 1.17: Seafloor mosaic based on 3D seismic surveys, offshore Nigeria. Color is derived from amplitude and color intensity based on artificial illumination from the north. Features indicated on the image indicate the X, Y, and Y` channel, distance marks along the channels, and basin boundaries. (From Pirmez et al., 2000).

As described by Pirmez et al. (2000), the X channel is only slightly sinuous and extends for about 80 km from the shelf edge, terminating in a depositional lobe. The depositional lobe is composed of two main depositional units and reaches a maximum thickness of about 80 ms in the center of the basin (Figure 1.18).

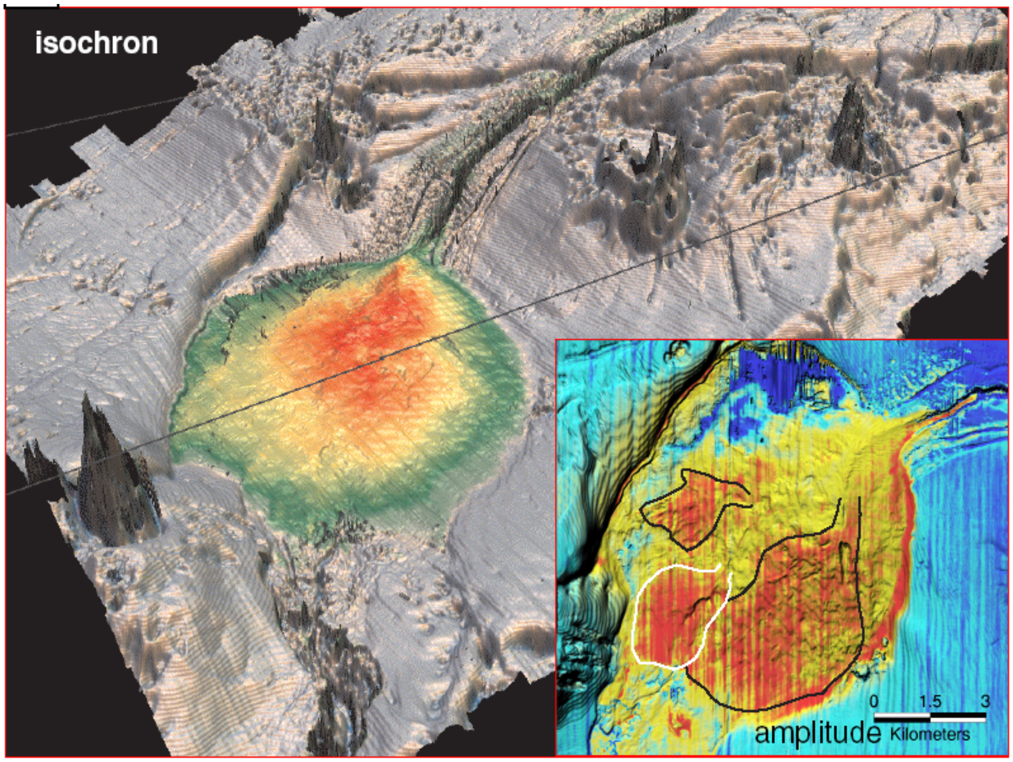

Figure 1.18: Analogous example: Niger Delta Slope: Three-dimensional perspective of depositional lobe of channel X, image represents isochron (maximum thickness is 100 ms, in red) draped on seafloor structure. Inset shows same area with amplitude draped on structure. Note high-amplitudes on feeder channel and in older channel down-dip of basin, indicating the sites of recent deposition. Lobate-shaped deposits are outlined in the amplitude patterns (From Pirmez et al., 2000).

1.14 FUNDAMENTALS OF SEISMIC INVERSION

Seismic inversion, as discussed in this study, refers to the inversion of seismic traces into acoustic impedance (AI, Ip) from post-stack seismic data, and [Ip, Is, Rho] or [Vp, Vs, Rho] from pre-stack seismic data. In simple terms, acoustic impedance inversion is just the transformation of post-stack seismic data into pseudo acoustic impedance logs at every trace (Latimer et al., 2000); and analogously, elastic inversion is the transformation of pre-seismic data into pseudo [Ip, Is, and Rho] or [Vp, Vs, Rho] logs at every trace.

1.14.1 Deterministic Inversion (Trace based)

The earliest methodologies developed for AI inversion were based on recursive or trace integration algorithm (RTI) methods. These are truly trace-based because the seismic trace is the sole input.

In the sparse spike inversion (SSI) algorithm, the reflection coefficients series underlying the acoustic impedance is assumed to be sparse; i.e., the seismic trace can be modeled with fewer reflection coefficients than seismic trace data samples. A sparse spike series is also broadband. In these methods the link to the seismic is also through the convolutional model, which can incorporate any wavelet. Nonuniqueness is countered by applying the sparsity criterion. To provide further control on reconstructing frequencies outside the seismic data bandwidth, modern constrained SSI algorithms (CSSI) can also use model data for stabilization and/or constraint (Figure 1.19).

Acoustic impedance is a mechanical property of rocks equal to the product of density and velocity, both of which can be directly measured by well logging.

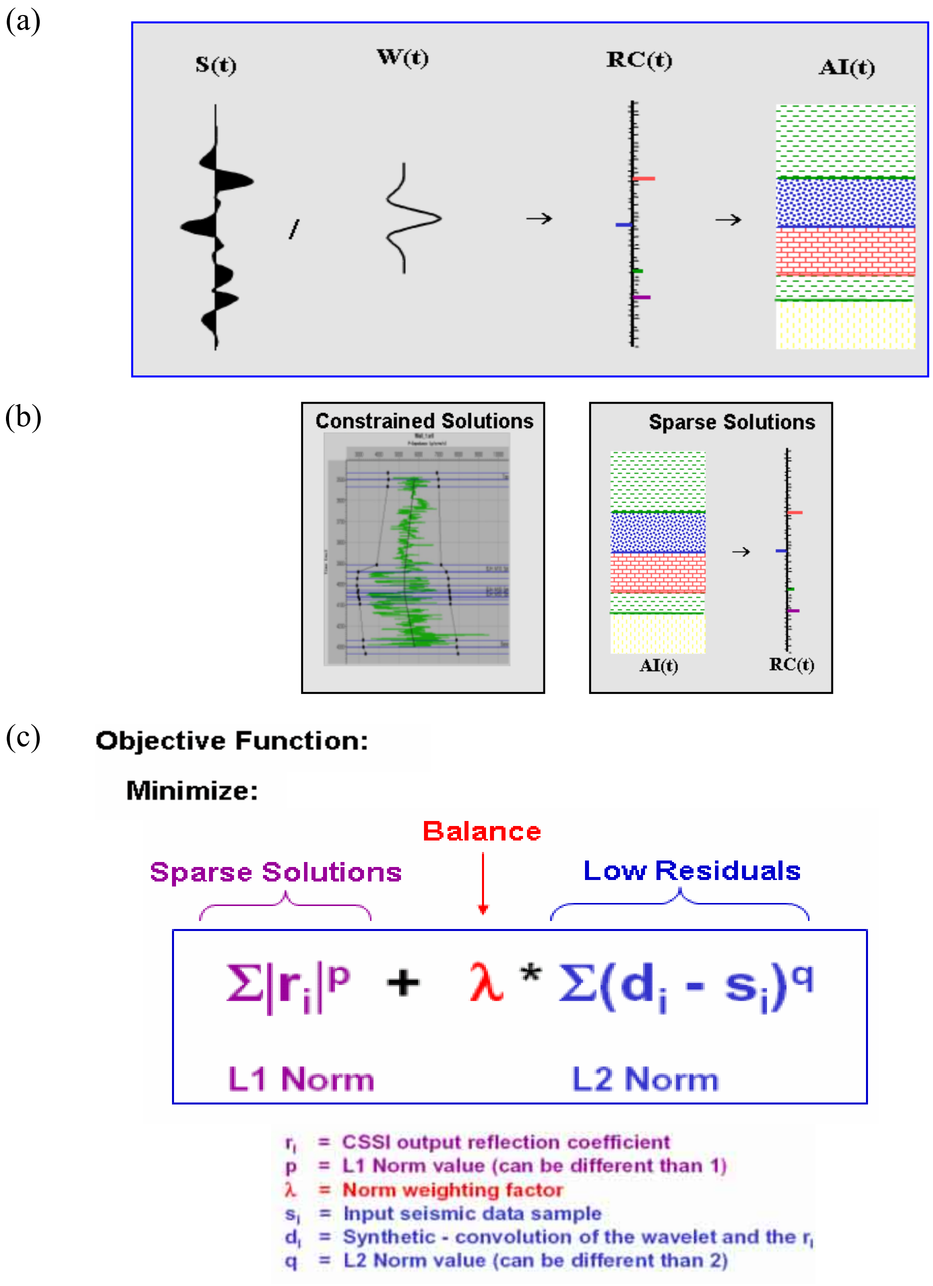

Objective Function:

Minimize:

$$\underbrace{\Sigma|r_i|^p}_{\text{L1 Norm}} + \lambda * \underbrace{\Sigma(d_i - s_i)^q}_{\text{L2 Norm}}$$

r_i = CSSI output reflection coefficient
p = L1 Norm value (can be different than 1)
λ = Norm weighting factor
s_i = Input seismic data sample
d_i = Synthetic - convolution of the wavelet and the r_i
q = L2 Norm value (can be different than 2)

Figure 1.19: Post-stack deterministic inversion. (a) General trace-based inverse modeling scheme. (b) Main CSSI attributes: well-log based constraints (left), sparse reflectivity series (right). (c) Basic CSSI objective function.

On the other hand, post-stack seismic data are an interface property, a close approximation to the convolution of the wavelet with a reflection coefficient series, which reflect relative changes in acoustic impedance. Therefore, acoustic impedance becomes a natural link between seismic and well data (Latimer et al., 2000).

The main objective of applying seismic inversion to this project is to generate an integrated 3D model of elastic properties (Ip, Is, Rho) for the area and interval of study that will be used for geological interpretation and quantitative reservoir characterization. The 3D models of elastic properties (Ip, Is, Rho) will be generated by applying trace-based inversion to the 3D post- and pre-stack seismic data. Such trace-based inversion will be performed with a constrained sparse-spike inversion (CSSI) algorithm that enforces time-dependent bound constraints to the results. The following input data will be used: the seismic data, a high-resolution sequence stratigraphic framework, and control wells with available P- and S-sonic and density information. Deterministic seismic inversion will provide a number of important benefits, including increased vertical resolution and generation of petrophysical relationships for reservoir characterization. For interpretation, the thinnest resolvable layer in the inverted data can be down to 1/3 the thickness of the thinnest resolvable layer in the seismic data. In other words, if 60-ft layers can be resolved with the seismic data alone, then 20-ft layers may be resolved with acoustic impedance. This is because inversion largely removes the wavelet tuning and side lobe effects caused by the close proximity of the reflection coefficients in seismically thin layers.

1.14.2 Stochastic or Geostatistical Inversion (Model based)

This inversion algorithm combines geostatistical data and modeling with seismic inversion. In geostatistical analysis, the spatial statistics of the data are generated. Geostatistical modeling simulates data at grid points starting from known control points, typically well logs. Geostatistical modeling preserves the spatial statistics of the data but does not guarantee that any simulations are consistent with seismic data. In geostatistical inversion, the simulation algorithm is modified to simultaneously honor both the wellbore and the seismic data while producing estimates of reservoir parameters between wells. Geostatistical inversion provides a powerful way to bring in information from outside the seismic bandwidth, utilizing both the well control and geologic control on the spatial distribution of acoustic impedance (Latimer et al., 2000).

Geostatistical inversion is also defined as a sequential method of stochastic modeling constrained by seismic data (Haas and Dubrule, 1994); this geostatistical technique allows the information from all available measurements to be integrated into a unique, consistent quantitative description of the reservoir (Torres-Verdin et al., 1999).

Standard geostatistical inversion techniques are based on Gaussian sequential geostatistical algorithms that simulate acoustic impedance along vertical traces following a random path in the seismic area. The geostatistical inversion algorithm simply accepts or discards simulations at individual grid points depending upon whether they produce synthetic seismograms approximately equal to those of the input seismic (Figure 1.20).

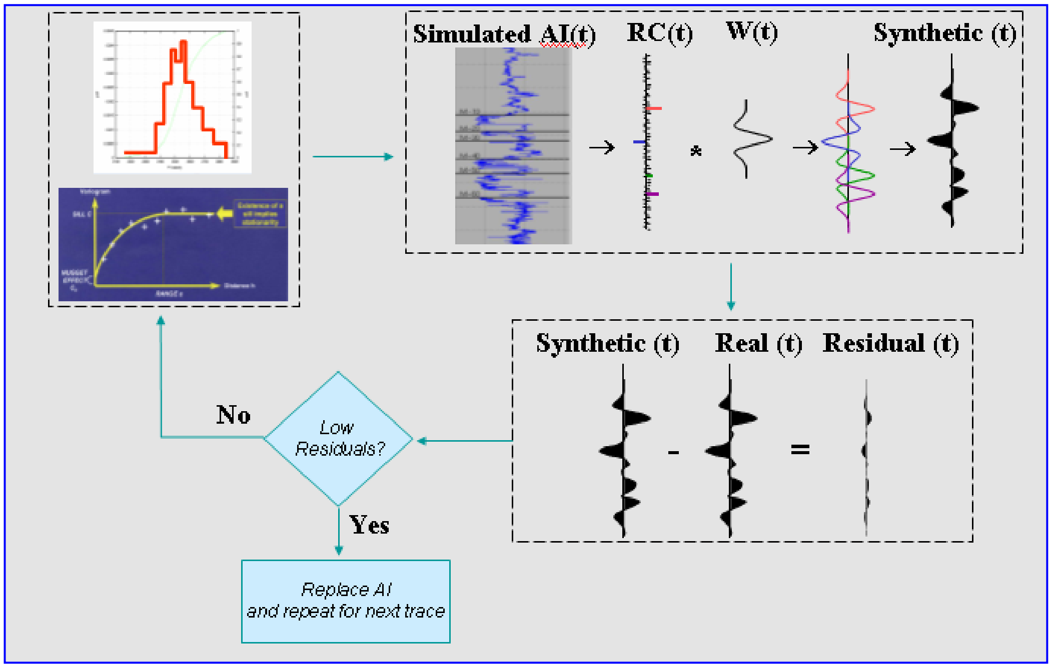

Figure 1.20: Post-stack stochastic inversion scheme. The traditional geostatistical inversion algorithm simply accepts or discards simulations at individual grid points depending upon whether they produce synthetic seismograms approximately equal to those of the input seismic. Two statistical parameters are used as input to stochastic simulation: the histogram and the variogram of acoustic impedance values.

Two statistical parameters are used as input to stochastic simulation: the histogram and the variogram of acoustic impedance values. Histograms of wellbore data are used to estimate and adjust probability distribution functions (PDFs), which the random realizations have to satisfy.

The variogram function statistically quantifies the variance of the difference between parameter values as a function of their distance (Haas and Dubrule, 1994). In the vertical direction, variograms are estimated from wellbore measurements and in the horizontal direction variograms are estimated from acoustic impedance values derived by trace-based inversion (Torres-Verdin et al., 1999).

Stochastic inversion is additionally used to generate multiple equiprobable models of reservoir properties such as lithology and porosity based on the acoustic impedance results. These equiprobable models honor not only the spatial detail provided by the well data but also the complexity and heterogeneity of the reservoir between the wells as defined in the previously generated impedance model possessing a higher vertical resolution than the seismic data.

Finally, geostatistical inversion results in a set of simulations, the variation of which can be used to make probability maps. Therefore, this technique provides an estimate of the uncertainty associated with the interpolation, hence allowing risk assessments.

1.15 SUMMARY

This chapter presented a general description of the geologic setting associated with the study area. Regional stratigraphic studies of the deepwater Miocene depositional history in the central Gulf of Mexico indicate that the M-series reservoir sands of the Marco Polo Field can be genetically associated with the Miocene MCAVLU Submarine Fan System. Core data analysis indicates that these reservoir sands have been initially described as stacked, progradational lobes within an overall fan complex. An initial depositional model suggests terminal lobes within a basin floor fan complex.

Chapter 2: AVA Deterministic Inversion

2.1 INTRODUCTION

The main objective of this chapter is to analyze and interpret pre-stack seismic amplitude data acquired in the Marco Polo hydrocarbon field based on deterministic inversion techniques. We are specifically concerned with a small portion of the Marco Polo Field where hydrocarbon-bearing sands pertain to the "M" series and are buried at depths of between 3500 and 3800 m.

In an effort to improve reservoir development of the study area we resorted to amplitude information of pre-stack seismic data to quantify the vertical and lateral extent of the main turbidite reservoirs. We first conducted amplitude versus angle (AVA) sensitivity analysis based on well-log data, and subsequently applied AVA simultaneous one-dimensional (1D) seismic inversion to generate three-dimensional (3D) spatial distributions of lithology/fluid-sensitive modulus attributes.

2.2 AVA FLUID/LITHOLOGY SENSITIVITY ANALYSIS

We used well-log measurements to assess the AVA behavior of the M-series sand reservoirs, and to determine the sensitivity of modulus attributes to variations of lithology and fluid content. This methodology involved the following techniques: (1) petrophysical analysis, (2) cross-plot analysis, (3) Biot-Gassmann fluid substitution, (4) AVA reflectivity modeling, and (5) numerical simulation of synthetic gathers.

2.2.1 Petrophysical Analysis

Standard petrophysical evaluation techniques were applied to generate curves of volume of shale, effective porosity, effective water saturation, and permeability. The methodology used for petrophysical analysis consisted of the following 7 steps:

(1) Generation of volume of shale (Vsh) curves from gamma ray logs using Larionov's equation for Tertiary clastic rocks (Dresser Atlas, 1992).

(2) Density porosity computation for a dual mineral (sand-matrix, shale) and single fluid (brine) model.

(3) Vsh-correction of density and neutron porosity logs.

(4) Effective porosity computation from average of Vsh-corrected density and neutron porosity logs.

(5) Simultaneous computation of effective water saturation and fluid-corrected effective porosity using the Simandoux model (Bassiouni, 1994) and the dual mineral (sand-matrix, shale) and dual fluid (brine, hydrocarbon) porosity model through an iterative optimization process.

(6) Generation of irreducible water saturation curves.

(7) Permeability computation from effective porosity and irreducible water saturation curves using the Tixier model (Bassiouni, 1994).

Core data were consistently used throughout the process to calibrate and validate computed curves. Figure 2.1 shows an example of the porosity, water saturation, and permeability results for control well # 1. Additionally, lithotype (sand/shale) logs were generated by combining multiple lithology-sensitive logs such as volume-of-shale, density, p-wave velocity, and s-wave velocity.

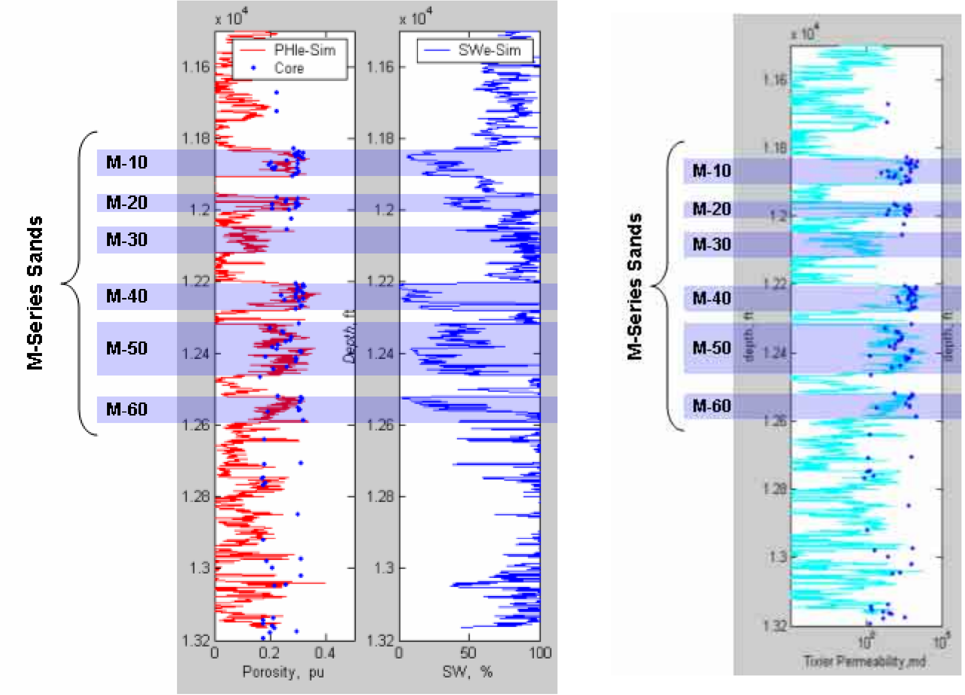

Figure 2.1: Example of curves generated from the petrophysical analysis. (a) Porosity (red) and water saturation (blue); (b) Permeability. Blue dots represent core data.

2.2.2 Cross-Plot Analysis

A detailed cross-plot analysis was performed to corroborate the existence of intrinsic correlations between elastic properties (P-velocity, S-velocity, and density) and petrophysical variables such as porosity and water saturation (Figure 2.2).

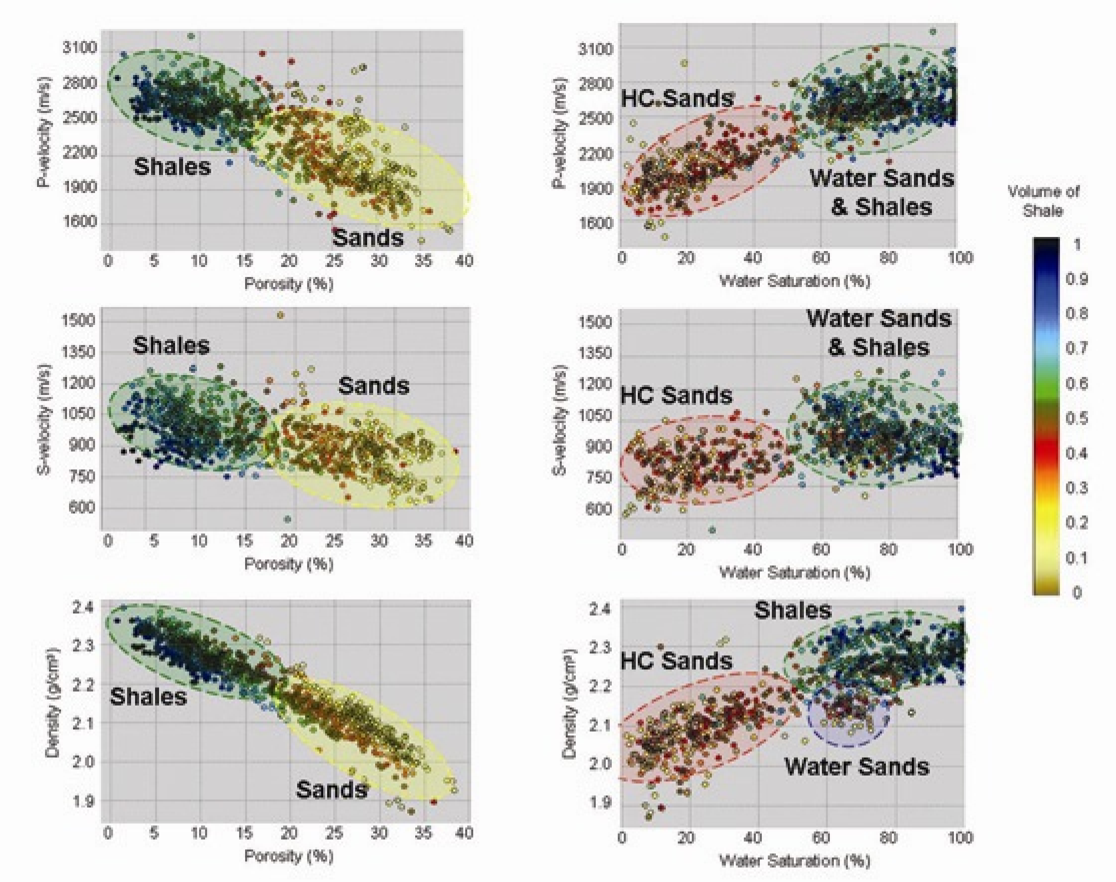

Figure 2.2: Cross-plot analysis corroborating the existence of correlations between elastic and petrophysical variables. From left to right: (1) elastic properties (Vp, Vs, ρ) vs. Porosity, (2) elastic properties (Vp, Vs, ρ) vs. water saturation. Color code represents volume-of-shale (Vsh).

Subsequently, P- and S-impedance (Ip and Is, respectively) being the product of the density times P- and S-velocity, respectively, were calculated from dipole-sonic and density logs. Then, we applied the "lamba-mu-rho" method introduced by Goodway et al. (1997) to generate fluid and lithology sensitive modulus attributes LambdaRho ($\lambda\rho$) and MuRho ($\mu\rho$), which are defined as the product of the Lame petrophysical parameters (λ and μ) times the bulk density (ρ), respectively. These modulus attributes were computed and cross-plotted with P- and S-impedance logs using

$$\lambda\rho = I_P^2 - 2I_S^2 , \tag{2.1}$$

and

$$\mu\rho = I_S^2 . \tag{2.2}$$

The effectiveness of this cross-plotting technique is based on the fact that $\lambda\rho$ is primarily sensitive to fluid content, lithology, and porosity, whereas $\mu\rho$ is primarily sensitive to lithology. Figure 2.3 shows a LambdaRho vs. MuRho cross-plot constructed with well-log data acquired along the M-series sands. Hydrocarbon-bearing sands are associated with relatively low values of $\lambda\rho$ and $\mu\rho$ whereas shales exhibit a completely opposite behavior characterized by relatively high values of $\lambda\rho$ and $\mu\rho$. Water-bearing sands, on the other hand, exhibit the low values of $\mu\rho$ characteristic of sands, whereas $\lambda\rho$ values (mostly fluid sensitive) are similar to those of shales.

2.2.3 Biot-Gassmann Fluid Substitution

We performed fluid substitution analysis to quantify the influence of saturating fluids on the acoustic properties of the “M-series” reservoir sands. This was accomplished using Biot-Gassmann’s theory (Biott, 1956; Gassmann, 1951) and assuming constant porosity values of 20, 25, and 30%. Results are shown in Figure 2.4, indicating that P-velocity, P-impedance, and LambaRho decrease with an increase of hydrocarbon saturation. This behavior is corroborated by the petrophysical analysis of well-log data, specifically from the M-series vertical interval (including encasing shales) and gathered from multiple wells (Figure 2.5).

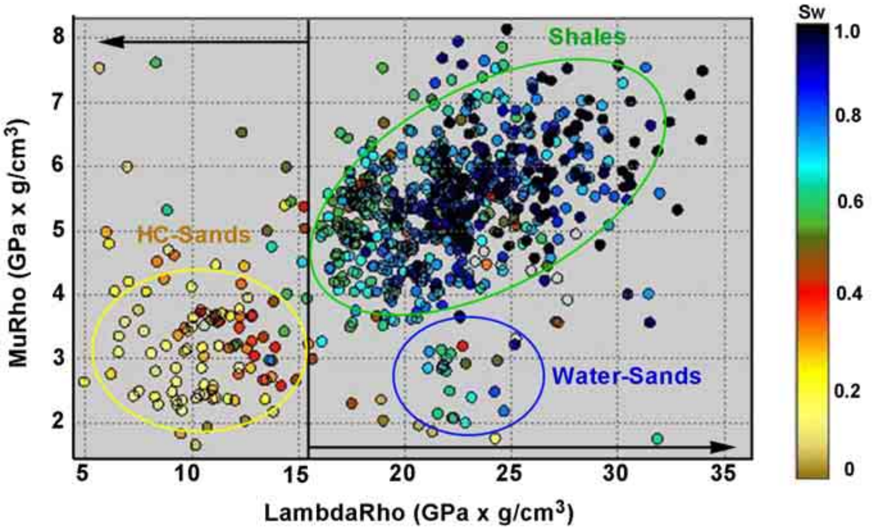

Figure 2.3: Cross-plot of LambdaRho (λρ) and. MuRho (μρ) constructed with the well-log data shown in Figure 1(b). Sands and shales are readily discriminated on the basis of μρ; sands are associated with low-values of μρ. Hydrocarbon-bearing sands can be differentiated from water-bearing sands and shales using λρ; hydrocarbon-bearing sands are associated with the lowest values of λρ.

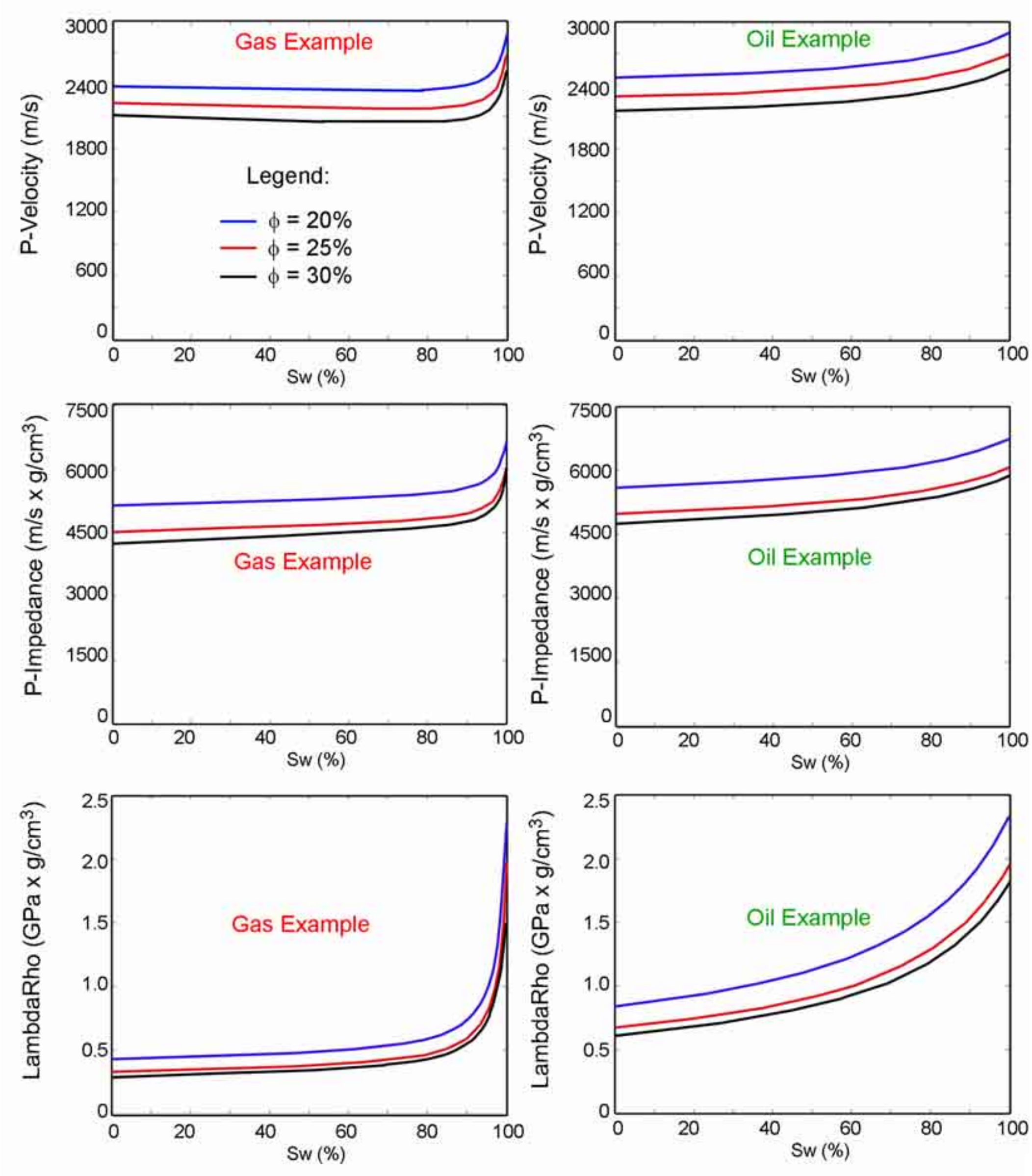

Figure 2.4: Biot-Gassmann fluid substitution exercise indicating that Vp, Ip, and $\lambda\rho$ decrease with an increase of hydrocarbon (oil /gas) saturation; the rate of decrease is a function of porosity. $\lambda\rho$ is considered anexcellent fluid discriminator since its relative change from 100% water saturation to 100% hydrocarbon saturation is larger than the corresponding relative change of either Vp or Ip.

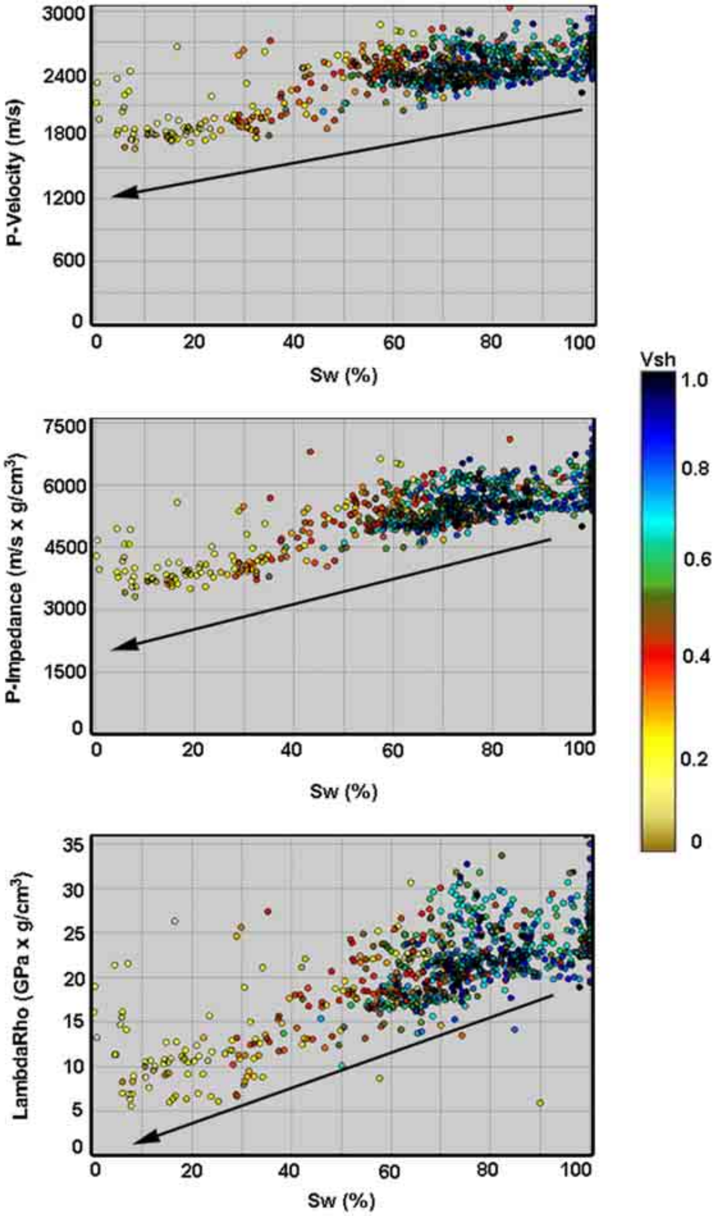

Figure 2.5: Cross-plots of water saturation and Vp, Ip, and λρ, generated from well-log data. Sample points are color coded based on the corresponding value of volumetric shale concentration. This exercise corroborates Biot-Gassmann predictions: oil-bearing sands are associated with relatively low values of Vp, Ip, and λρ.

2.2.4 AVA Reflectivity Modeling

Well-log data in combination with Zoeppritz equations were used to simulate variations of PP reflectivity with angle of incidence at the top of the M-10 reservoir. The latter interface is a shale/gas-sand contact. Results from this exercise are shown in Figure 2.6(a). The simulated AVA reflectivity is negative at normal incidence (R_0) and its absolute value increases with angle. This behavior corresponds to the characteristic AVO response of Class III sands as defined by Rutherford and Williams (1989). Class III AVO sands are usually undercompacted and unconsolidated and, consequently, are associated with impedance values lower than those of the embedding shale as well as with larger negative values of R_0.

2.2.5 Numerical Simulation of Synthetic Gathers

We simulated one-dimensional, normal moveout (NMO)-corrected synthetic gathers using well-log data acquired in an oil-producing well. Simulated gathers are the result of the convolution between a previously extracted wavelet and the well-log AVA reflectivity series. These reflectivity series were computed from Vp, Vs, and density logs using the Knott-Zoeppritz equations (Aki and Richards, 1980). Figure 2.6(c) shows results from the simulation of 1D NMO-corrected synthetic gathers. Consistent with the results of AVA reflectivity modeling, the synthetic gather simulated at the top of the M-10 reservoir sand exhibits a clear increase of amplitude with angle of incidence. This typical Class-

III AVO behavior is corroborated by the measured angle gathers shown in Figure 2.6(b).

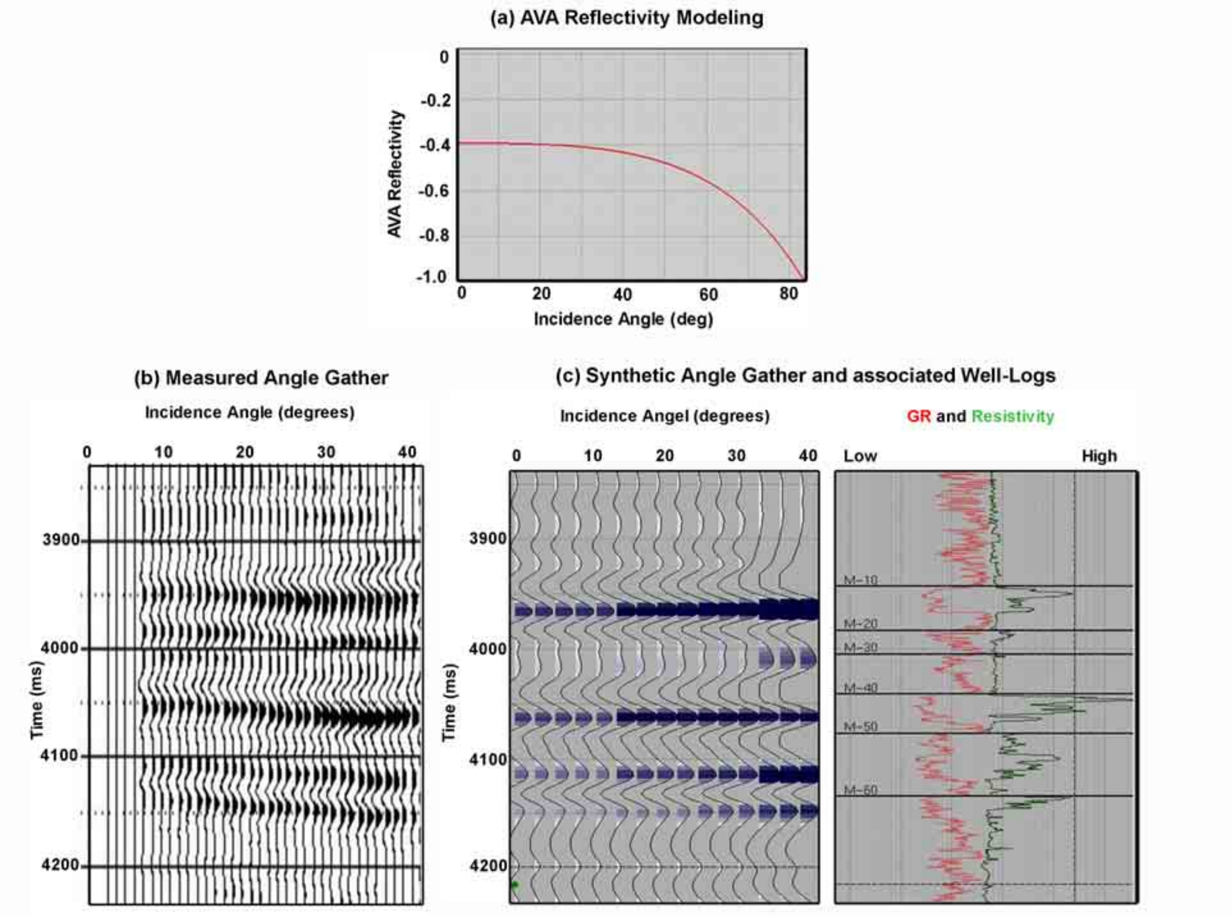
(a) AVA Reflectivity Modeling

(b) Measured Angle Gather

(c) Synthetic Angle Gather and associated Well-Logs

Figure 2.6: (a) Reflectivity modeling of the Shale/M-10 hydrocarbon-sand interface, (b) measured angle gather, and (c) synthetic angle gather. Both reflectivity and seismic amplitudes increase with an increase of angle of incidence (typical Class-III AVO behavior).

2.3 AVA SIMULTANEOUS INVERSION

Our inversion methodology consisted of: (1) partial-angle stacking and time alignment, (2) low-frequency modeling, (3) angle-dependent wavelet estimation, (4) 1D AVA-Constrained Sparse-Spike (CSSI) simultaneous inversion, (5) quality control of inversion parameters, and (6) extraction of petrophysical attributes.

2.3.1 Seismic Amplitude Data

Seismic amplitude measurements were sampled at 4 ms and have a frequency band of 6-70 Hz, with a central frequency of 20 Hz. For an average P-velocity of 2500 m/s, the expected vertical seismic resolution is approximately 18 m. The 3D survey in the Marco Polo Field consisted of 254 cross-lines spaced at 25 m intervals (6.35 km), and 320 in-lines spaced at 20 m intervals (6.4 km). This acquisition amounted to 81,280 traces over an area of approximately 40.64 km^2. The measured CMP gathers were migrated and corrected for NMO using a pre-stack time-domain migration algorithm. In this dissertation, we assume that the migrated and NMO-corrected CMP gathers are devoid of multiple and transmission effects and can be accurately described as the superposition of two-layer responses of a stack of horizontal layers. Further, we consider only PP reflectivity events in the analysis of pre-stack seismic amplitude variations. These assumptions are justified by the quality control performed on the migrated and NMO-corrected CMP gathers.

2.3.2 Partial-Angle Stacking and Time Alignment

The version of the 1D inversion algorithm implemented in this study assumes input seismic amplitude data organized into partial angle stacks (PAS). Therefore, special processing of the pre-stack seismic amplitude data was performed prior to 1D inversion. We used a ray tracing algorithm to transform the pre-stack seismic amplitude data from the offset domain to the incidence-angle domain, and generated four partial-angle stacks using the NMO-corrected and migrated offset-gathers and the migration-velocity field. The angle range available from the seismic amplitude data was 6 to 46 degrees; each partial-angle stack was generated using a 10-degree constant range. Final partial stacks included the following near, mid, far, and ultrafar angle ranges: [6-16], [16-26], [26-36], and [36-46]. In addition, small time-shift corrections were applied to the partial-angle stacks in order to reduce event misalignment due to processing errors such as residual NMO corrections.

2.3.3 Low-Frequency Modeling

Low-frequency volumes of P-Impedance, S-Impedance, and density are required for 1D trace-based inversion because the low-frequency information needed to include the compaction trend (0-6 Hz in our case) is not available from the seismic amplitude data. Additionally, low-frequency volumes are used to guide the soft-trend constraints imposed by the 1D inversion algorithm. We generated these volumes with the weighted lateral interpolation of well logs using the geological model as guiding framework. The geological model was constructed based on the horizon interpretation of the tops of the main geological formations. Finally, the interpolated models were low-pass filtered with a cut-off frequency of 6 Hz to generate the final low-frequency property volumes.

2.3.4 Angle-Dependent Wavelet Estimation

The estimation of AVA wavelets within the target time interval was performed with deterministic techniques. Well-log data are combined with the partial-angle stacks to directly estimate the corresponding angle-dependent wavelets using Knott-Zoeppritz equations. Basically, the angle-dependent reflectivity is derived from the P-sonic, S-sonic, and density well logs, using the angle range assigned to the partial angle stack being considered. Subsequently, a best least-squares wavelet is computed from this reflectivity and the seismic amplitude data following the method of White (1980).

2.3.5 1D AVA-CSSI Simultaneous Inversion

The 1D deterministic inversion of partially-stacked seismic amplitude data used in this dissertation is based on the "Amplitude-Versus-Angle – Constrained Sparse Spike Inversion" (AVA-CSSI) algorithm developed by Fugro-Jason. As described in the Appendix, the inversion algorithm minimizes an objective function that combines L_1-norms of reflectivity with L_2-norms of seismic amplitude data misfit, subject to value-range constraints (Debeye and van Riel, 1990; Pendrel and van Riel, 1997). The AVA-CSSI inversion algorithm combines all the available CMP gathers to estimate the corresponding 1D time-domain distributions of P-impedance, S-impedance, and density. This trace-based inversion algorithm is an extension to non-zero offsets of a previously published post-stack (zero-offset) constrained sparse spike inversion (Z0-CSSI) method (Debeye and van Riel, 1990). In the Z0-CSSI algorithm, a single stacked seismic section is inverted into a 1D time distribution of normal-incidence acoustic impedance (AI) (Debeye and van Riel, 1990; Pendrel and van Riel, 1997; Latimer et al., 2000), whereas in the AVA-CSSI algorithm multiple partial-angle stacks (PAS) are simultaneously inverted into 1D time distributions of P-impedance (I_p), S-impedance (I_s) and density (ρ). The inversion algorithm simulates the seismic amplitude measurements with 1D convolution based on the Zoeppritz (Koefoed, 1962) or Aki and Richards (1980) equations for two-layer AVO reflectivity.

The main CSSI inversion parameters include: (a) a stabilization parameter "alfa" (α) which enforces a tradeoff between data misfit (low seismic amplitude residuals) and sparsity of reflectors (and associated reflectivities) and (b) the "merge frequency cut-off", which is used to merge the band-limited inversion results with the low-frequency component interpolated from well-log data. These inversion parameters were chosen based on a sensitivity analysis of inversion results that included the following performance criteria: (1) high cross-correlation between synthetic (inversion derived) and measured seismic amplitude data; and (2) high model-space cross-correlation between inverted and measured elastic properties at well locations. The aligned partial-angle stacks (corresponding to near, mid, far, and ultra-far angle ranges), were simultaneously inverted via AVA-CSSI making use of the previously estimated angle-dependent wavelets and the low-frequency volumes of elastic properties. Inversions focused exclusively on PP reflectivities (incident-reflected P-waves). Final products were volumes of I_p, I_s, and ρ obtained from separate 1D inversions of CMP gathers (Figures 2.7 and 2.8).

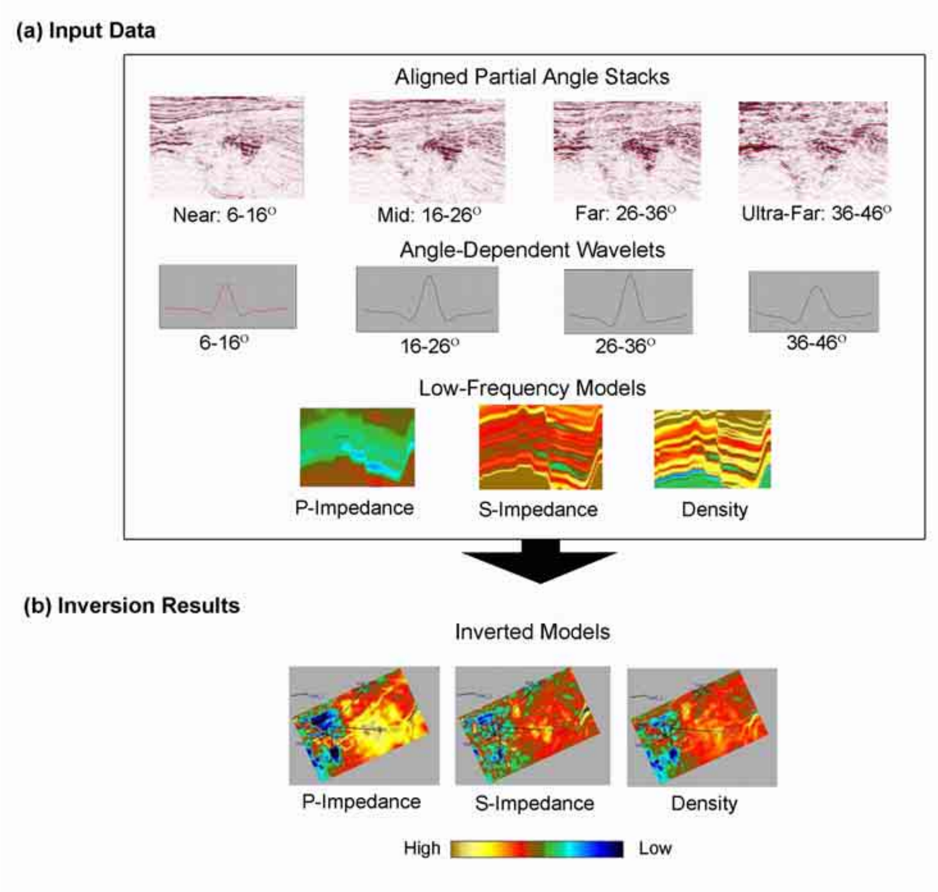

Figure 2.7: Schematic description of the AVA simultaneous inversion methodology: (a) Input data: four partial-angle stacks with the corresponding wavelets (extracted from elastic impedance logs), and low-frequency models of P-impedance, S-impedance, and density (generated from the horizon-guided interpolation of well-log data). Inversion results consist of full-band volumes of P-impedance, S-impedance, and density. Panel (b) shows RMS maps of these properties within the M-10 reservoir.

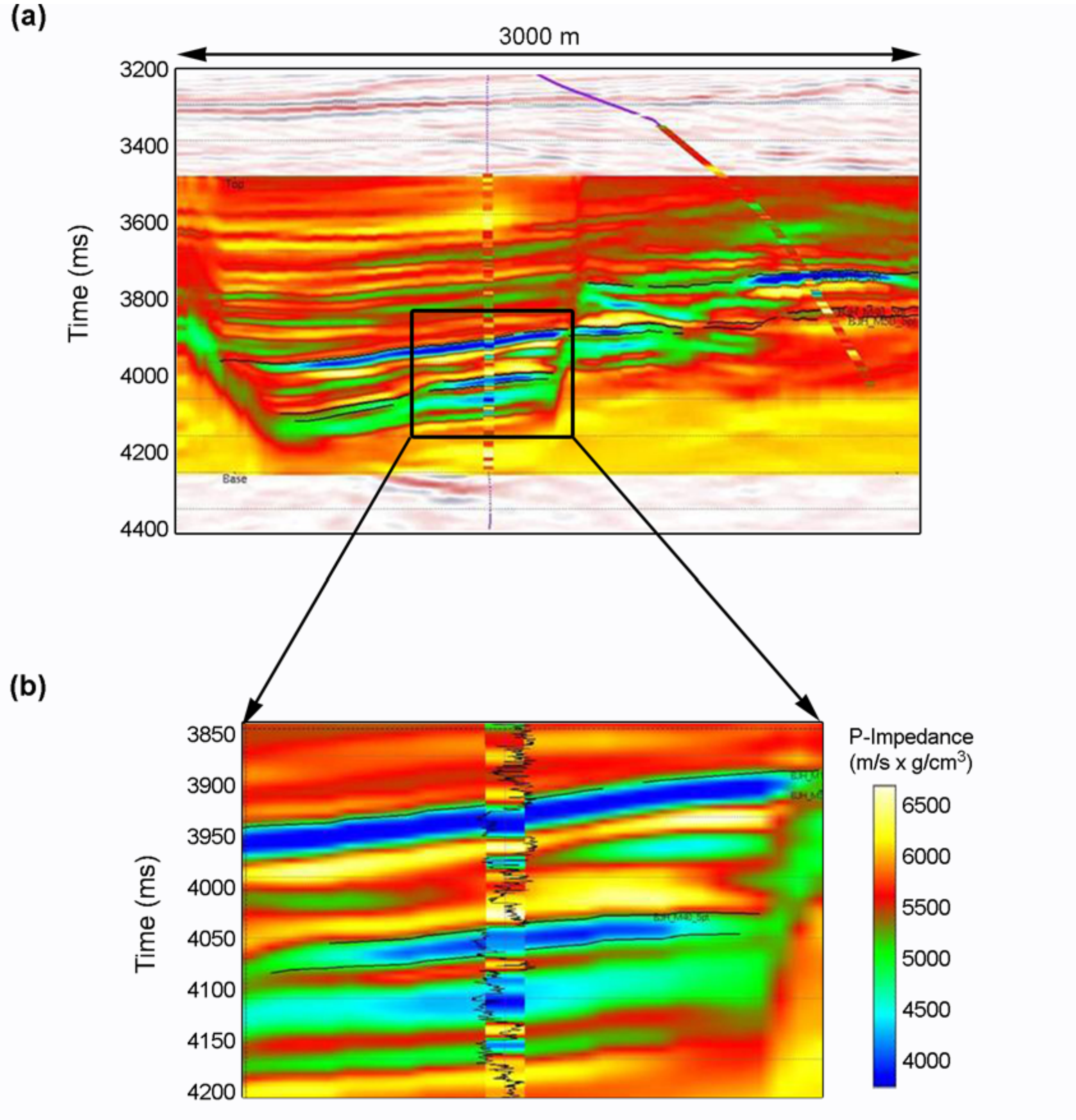

Figure 2.8: AVA-CSSI acoustic impedance results: (a) Acoustic impedance (Ip) section intersecting the exploratory well and one of its side-tracks. Hydrocarbon-bearing sand units coincide with the lowest values of Ip; (b) enlarged view around the vertical well, with overlying Ip (low-pass filtered) and gamma-ray logs (wiggle) included to emphasize the degree of vertical resolution obtained with AVA-CSSI inversion.

AVA-CSSI generated acoustic impedances are very similar to those obtained from previous post-stack inversion tests (Z0-CSSI); however, a significant improvement in the vertical resolution of the estimated P-impedance (compared to well-log AI) is achieved with AVA simultaneous inversion (Figure 2.9). This relative gain in vertical resolution is attributed to the fact that pre-stack (or partially stacked) seismic amplitude data include AVA information that is not preserved in the fully-stacked seismic amplitude data.

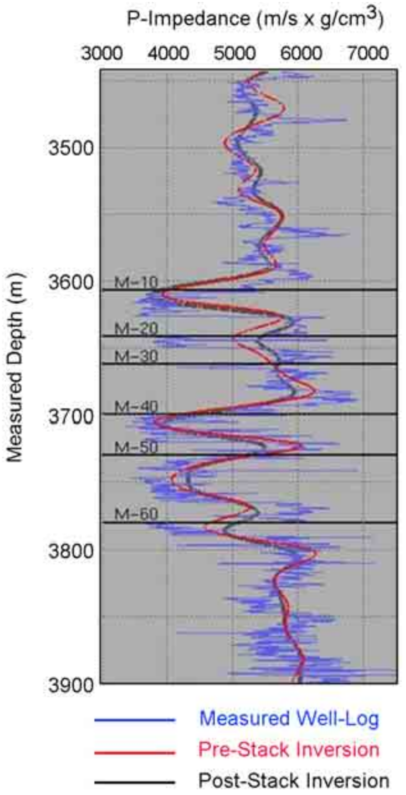

Figure 2.9: Comparison between post-stack (black) and pre-stack (red) inverted acoustic impedance (Ip) and well-log Ip (blue).

2.3.6 Quality Control of Inversion Results

The accuracy and reliability of the 1D inversion results was quantified in four ways: (a) with a sensitivity analysis of inversion residuals, (b) with a perturbation analysis of all of the inversion parameters, (c) with inversion exercises performed on multiple combinations of angle ranges, and (d) with tests on “blind” wells (wells not included as part of the input data for the inversions).

2.3.7 Extraction of Petrophysical Attributes

During this final phase, the two main inversion products, P- and S-impedance, were used to generate volumes of the fluid and lithology sensitive modulus attributes $\lambda\rho$ and $\mu\rho$ using equations (1) and (2). Figure 2.10(b) is a 3D view of the root-mean-square (RMS) attribute of $\lambda\rho$ for the M-10 reservoir overlaying a structural map in seismic time at the top of the same reservoir (Figure 2.10a). In this project, the $\lambda\rho$ attribute, which is primarily sensitive to the rock’s fluid component, is extremely valuable in the delineation of hydrocarbon-bearing rocks. As indicated by the Biot-Gassmann fluid substitution exercise, replacement of water by hydrocarbon in water-saturated sands decreases the values of Vp, Ip, and $\lambda\rho$. Accordingly, wells with confirmed hydrocarbon presence (shown with green lines in Figure 2.10(b) are located within the boundaries of low $\lambda\rho$ anomalies, whereas dry or water-wells (shown with blue lines in Figure 2.10b) coincide with high $\lambda\rho$ anomalies. Figure 2.10(c) is a 3D graphical rendering of low-$\lambda\rho$ geobodies associated with the best hydrocarbon-producing areas across the M-series sands. Such low-$\lambda\rho$ geobodies were extracted from the previously computed $\lambda\rho$ volume using a cut-off of 16 GPa x g/cm^3.

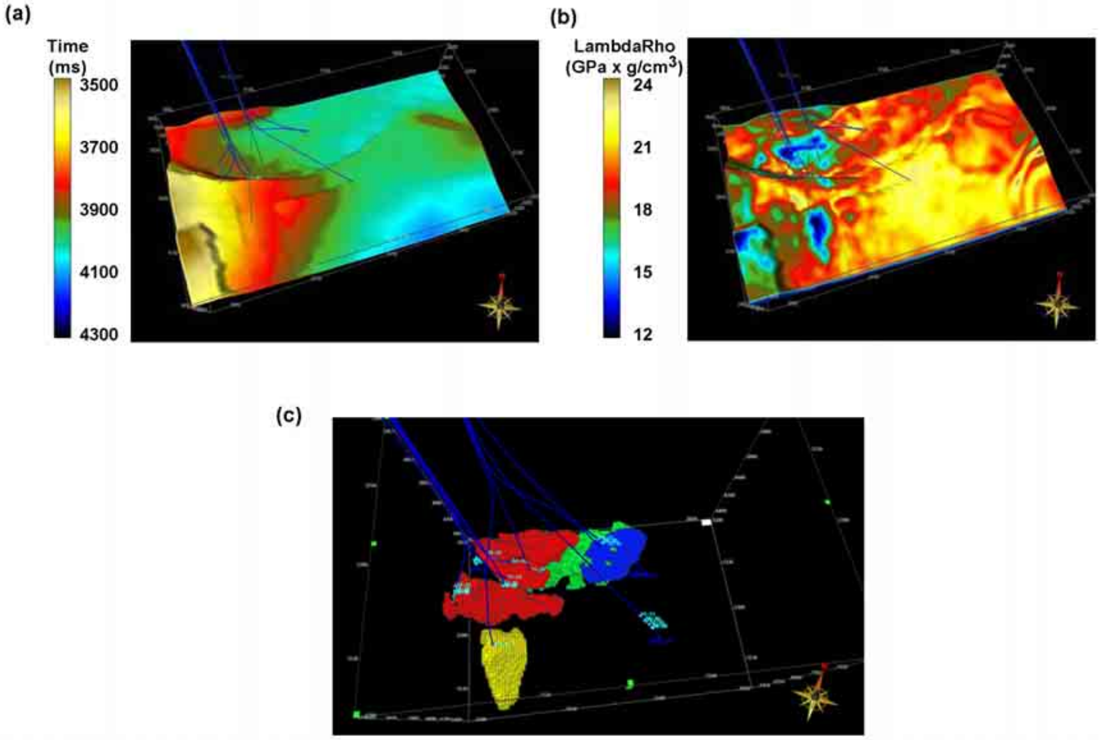

Figure 2.10: (a) Structural map in seismic time of the top of the "M-10" reservoir; (b) RMS map of $\lambda\rho$ for the M-10 reservoir overlying the same structural map shown in (a); (c) Geobodies captured with low values of $\lambda\rho$ correspond to M-series sands (different colors identify non-connected geobodies). Most hydrocarbon-prospective areas coincide with zones of low $\lambda\rho$ values. Blue lines represent well trajectories. The spatial coverage considered in the figures is approximately 8 km^2.

High-porosity geobodies associated with the best hydrocarbon-prospective zones were extracted from an AI-derived porosity volume. A linear relationship between porosity and AI inferred from well-log data was applied to transform the inverted AI volume into a pseudo-porosity volume (Figure 2.11a); subsequently, a cut-off of porosity >28% (Figure 2.11b) was applied to the volume in order to isolate high-porosity geobodies associated with the best hydrocarbon-prospective areas across the M-series sands. Figure 2.11(c) is the final 3D rendering of the high-porosity geobodies resulting from this exercise.

2.3.8 Integration and Geologic Interpretation of Inversion Results

Previous interpretations from regional stratigraphic/depositional studies (Galloway et al., 2000; Combellas, 2003), indicate that the M-series turbidite deposits of the Marco Polo Field are genetically linked to the Western submarine fan of the Miocene MCAVLU Submarine Fan System. Accordingly, initial geological interpretation of core data indicated that the depositional environment consisted of deepwater turbidites associated with terminal lobes.

By integrating the information rendered by core data, the characteristics of the channel/lobe depositional model introduced by Galloway and Hobday (1996) (Figure 2.12a), and the geomorphologic visualization achieved with 1D pre-stack inversion results (Figure 2.12b), the M-series reservoir can be conclusively described as stacked turbidite lobes within an overall fan complex.

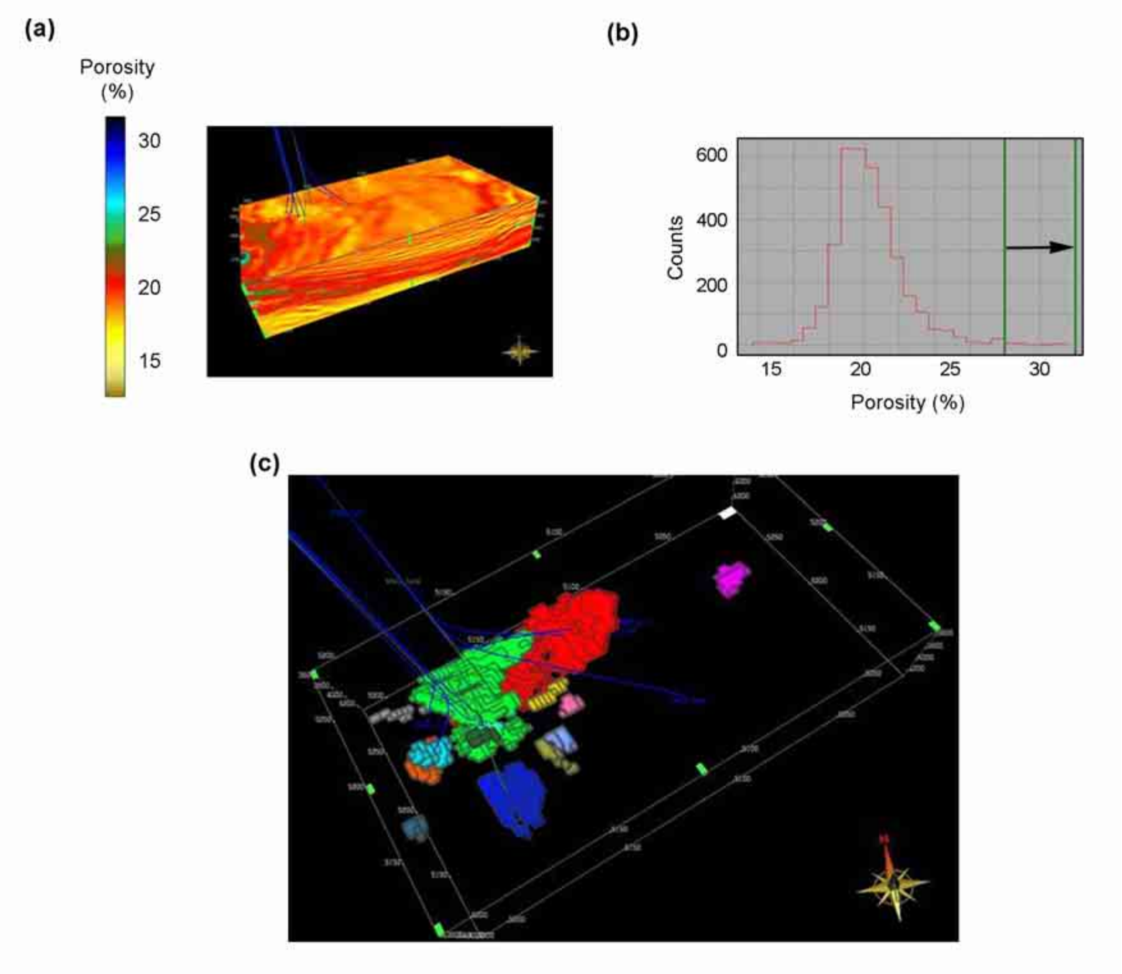

Figure 2.11: Porosity from P-impedance (Ip): (a) Porosity volume calculated with a linear relationship between porosity and Ip inferred from well-log data. (b) Histogram of computed porosity values indicating the range of porosity values considered for reservoir delineation (porosity > 28 %). (c) 3D visualization of geobodies captured from zones that exhibit low values of Ip within the “M”-Series reservoirs (different colors are used to indicate non-connectivity between geobodies). The spatial coverage considered in the figures is approximately 8 km^2.

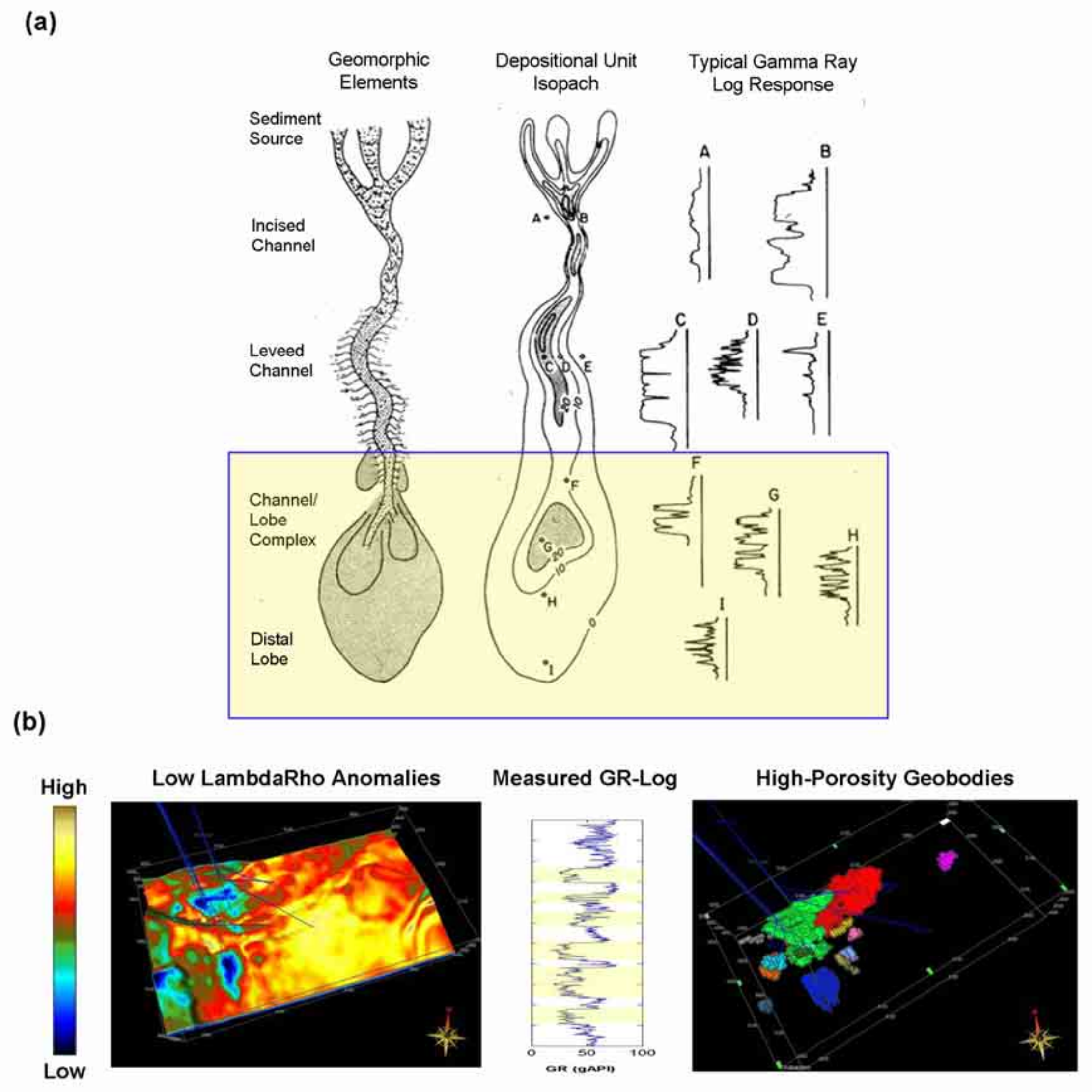

Figure 2.12: (a) Depositional model: Geomorphic elements, depositional isopach unit, and typical well-log responses of a channel-lobe complex (modified from Galloway and Hobday, 1996); and (b) Deterministic inversion results. From integration of the above information, the M-series reservoirs can be interpreted as stacked turbidite lobes.

2.4 SUMMARY

This chapter describes the successful application of amplitude-versus-angle (AVA) one-dimensional inversion of pre-stack seismic amplitude data to detect and delineate deepwater hydrocarbon reservoirs in the central Gulf of Mexico.

Detailed AVA fluid/lithology sensitivity analysis was conducted to assess the nature of AVA effects in the study area based on well-log data. Standard techniques such as cross-plot analysis, Biot-Gassmann fluid substitution, AVA reflectivity modeling, and numerical simulation of synthetic gathers were part of the AVA sensitivity analysis. Cross-plot and Biot-Gassmann analyses indicate significant sensitivity of acoustic properties to fluid substitution. AVA reflectivity and angle-gather modeling indicate that the shale/sand interfaces represented by the top and base of the M-10 reservoir are associated with typical Class III AVA responses due to relatively low-impedance gas-bearing sands. Consequently, one-dimensional pre-stack seismic inversion provided accurate and reliable quantitative information about the spatial distribution of lithology and fluid units within the turbidite reservoirs based on the interpretation of fluid/lithology-sensitive modulus attributes.

From the integration of inversion results with analogous depositional models, the M-series reservoirs were interpreted as stacked terminal turbidite lobes within an overall fan complex. This interpretation is consistent with previous regional stratigraphic/depositional studies.

Chapter 3: Sensitivity Analysis of Data Factors Controlling AVA Deterministic Inversion

3.1 INTRODUCTION

Estimation of spatial distributions of elastic parameters from pre-stack seismic amplitude data is a subject of contemporary interest to exploration and reservoir geophysicists alike. It is customarily assumed that pre-stack migration algorithms yield CMP gathers that can be regarded as the superposition of the time-domain response of two-layer oblique plane-wave reflections of a stack of horizontal layers (Koefoed, 1962; Aki and Richards, 1980). Subsequently, the migrated CMP gathers are subject to interpretation methods such as amplitude-vs.-offset (AVO) amplitude analysis to estimate petrophysical properties of layers from variations of seismic amplitude with angle of incidence (Rutherford and Williams, 1989; Castagna and Backus, 1993).

A yet more sophisticated approach consists of directly estimating elastic properties of layers from the full-wave amplitude response measured by migrated CMP gathers (Kormendi and Dietrich, 1991; Mallick, 1999; Sen and Roy, 2003). The latter methods employ inversion techniques that assume accurate knowledge of the frequency spectrum of the plane-wave source originating the reflections. Inversion results consist of one-dimensional (1D) distributions of elastic parameters (or combinations of elastic parameters) that best fit the measured pre-stack seismic amplitudes under some metric (Pan and Phinney, 1989; Kormendi and Dietrich, 1991; Mallick, 1999; Sen and Roy, 2003). A plethora of 1D inversion procedures have been reported in the open technical literature that consider multiple variations of the forward modeling, stabilization, and non-uniqueness components of the estimation (Sen and Stoffa, 1991; Xia et al., 1998; Pendrel et al., 2000; Roy et al., 2004).

There is no doubt that the performance and reliability of 1D inversion techniques used for the interpretation of pre-stack seismic amplitude data largely depend on (a) the quality and field acquisition parameters used to measure raw seismic reflections, and (b) the quality and reliability of the pre-stack migration method applied to raw seismic measurements (especially the preservation of seismic amplitudes and the influence of the input smooth volumes of P-wave velocity). However, even in the presence of noise-free and perfectly migrated seismic amplitude data, the question remains whether 1D inversion procedures accurately and reliably estimate vertical variations of elastic properties as otherwise measured, for instance, with borehole logging tools.

The objective of this chapter is to appraise the accuracy and reliability of the inversion of pre-stack seismic amplitude data to estimate 1D distributions of P-wave impedance, S-wave impedance, and density. To this end, we consider a state-of-the-art deterministic inversion algorithm that operates on normal-moveout (NMO) corrected pre-stack seismic data organized in the form of partial-angle stacks (PAS). This inversion algorithm includes the most important components of most deterministic inversion algorithms published in the open technical literature and hence provides a convenient means to appraise the accuracy and reliability of the inversion process in general. We focus our attention on synthetic and recorded pre-stack seismic amplitude data acquired in unconsolidated clastic sediments from the Marco Polo Field (Figure 3.1).

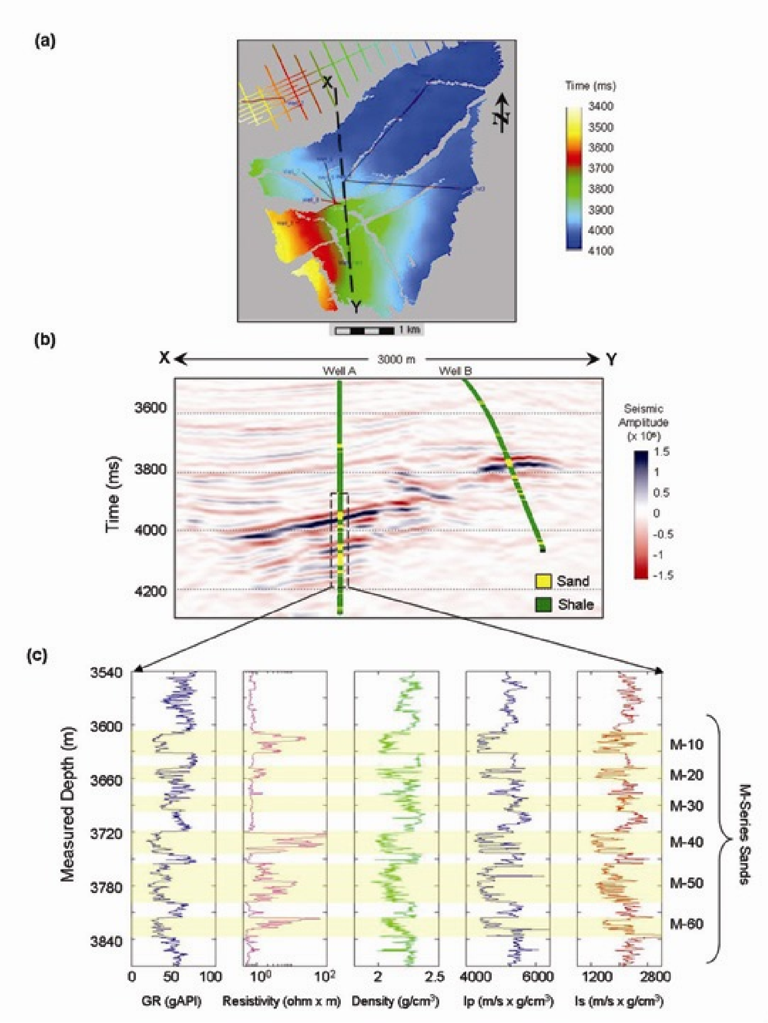

Figure 3.1: Time structural map of the Marco Polo Field including well locations and a seismic-time horizon (top of the M-10 reservoir). (b) Seismic cross-section in time with lithotype well logs indicating the vertical interval of the M-series sands. (c) Example of wireline logs acquired in the vertical control well shown in Panel (b). Well-log measurements evidence the characteristic low density, P-impedance (*Ip*), and S-impedance (*Is*) values across the hydrocarbon-bearing M-series sands.

One-dimensional AVA deterministic seismic inversion has been successfully applied in numerous case studies associated with conventional and non-conventional reservoirs involving siliciclastic and carbonate settings (Madiba and McMechan, 2003a,b). Several deterministic and stochastic inversion projects have been conducted to characterize the M-series hydrocarbon reservoirs in the Marco Polo Field (Contreras et al., 2005). However, a detailed analysis of data-related factors controlling the reliability of AVA deterministic seismic inversion remains necessary to quantify the relative advantages and pitfalls of the technique. In an effort to appraise the reliability and non-uniqueness of pre-stack seismic inversion products we performed a detailed sensitivity analysis on the main data-related factors controlling the inversion algorithm. We first conducted forward modeling and inversion of synthetic data, and subsequently applied AVA simultaneous inversion to recorded seismic amplitude measurements.

Even though the inversion of pre-stack seismic amplitude data entails the analysis of a multitude of factors related to algorithmic performance and limitations of the input data, in this dissertation we chose to focus the analysis on data-related factors such as quality of the stacking velocity function, angle-range selection, alignment of seismic PAS, and wavelet estimation. All other parameters associated with the implementation of the inversion algorithm have been kept invariant. Moreover, in an effort to maintain the influence and bias of inversion parameters to a minimum, we did not enforce artificial or empirical correlations between P-velocity, S-velocity, and/or density when performing the inversion.

3.2 1D AVA-CSSI SIMULTANEOUS INVERSION

As described in chapter 2, the 1D deterministic inversion of partially-stacked seismic amplitude data considered in this dissertation is based on the "Amplitude-Versus-Angle – Constrained Sparse Spike Inversion" (AVA-CSSI) algorithm, developed by Fugro-Jason (Debeye and van Riel, 1990; Pendrel and van Riel, 1997; Pendrel et al., 2000). This inversion algorithm considers each pre-stack CMP gather separately and estimates 1D distributions of P-wave impedance, S-wave impedance, and density by minimizing the quadratic difference between the numerically simulated and the recorded seismic amplitudes subject to value-range constraints. Stabilization of the inversion against presence of noisy seismic amplitudes is performed by controlling the amplitude of reflectivities and the clustering of reflectors.

The inversion algorithm assumes that (a) the input CMP gather has been properly migrated and corrected for NMO effects, (b) time is measured as two-way vertical travel time, (b) the input pre-stack seismic amplitude measurements can be described as the superposition of time-dependent PP isotropic two-layer plane-wave reflections, (c) the input pre-stack seismic amplitudes are devoid of multiple reflection effects, (d) transmission and dispersion amplitude effects are negligible, and (e) the frequency spectrum of the input wavelet is constant with time. Specific technical details about the inversion algorithm are given in the Appendix. In what follows, we adhere to the above assumptions and leave a sensitivity study of errors in these assumptions as the subject of a future research study.

The inversion algorithm is an extension of non-zero offsets of the post-stack (zero-offset) constrained sparse spike inversion (Z0-CSSI) method. In Z0-CSSI, a single stacked seismic section is inverted into a 1D distribution of normal incident acoustic impedance (AI) (Debeye and van Riel, 1990; Pendrel and van Riel, 1997; Latimer et al., 2000). In the case of AVA-CSSI, multiple partial-angle stacks (PAS) are simultaneously inverted into 1D distributions of P-impedance (Ip), S-impedance (Is), and density (ρ). Numerical simulation of AVA seismic amplitudes is performed with a convolutional model based on isotropic two-layer plane-wave Zoeppritz reflectivity equations (Koefoed, 1962).

The main AVA-CSSI inversion parameters include: (a) a stabilization parameter "alfa" (α) which enforces a tradeoff between data misfit (low seismic amplitude residuals, sparsity (density) of reflectors, and amplitude of the associated reflectivities, and (b) the "merge frequency cut-off", which is used to merge the band-limited inversion results and the low-frequency component interpolated from well-log data. These inversion parameters were chosen based on a sensitivity analysis of inversion results that included the following performance criteria: (1) high correlation between synthetic (inversion derived) and recorded seismic amplitude data; and (2) high model-space correlation between inverted and measured elastic properties along well trajectories.

3.3 FORWARD MODELING AND INVERSION OF SYNTHETIC DATA

We generated synthetic pre-stack seismic amplitude data using well-log data, angle-dependent wavelets, and the structural/stratigraphic embedding of the

Marco Polo Field. Initially, 3D models of elastic properties (P-Impedance, S-Impedance, and density) were numerically interpolated from well-log data honoring the structural/stratigraphic geological model. Subsequently, the elastic models were used to produce four synthetic PAS for the angle intervals [5-10°], [10-15°], [15-20°], and [20-25°], via AVA reflectivity modeling with Knott-Zoeppritz's two-layer reflectivity equations and by subsequent convolution with the corresponding angle-dependent wavelets (Figure 3.2). The wavelets used in this exercise were estimated from recorded PAS in order to consider realistic amplitude and frequency values, and to make the synthetic inversion results comparable to subsequent inversion tests on recorded seismic amplitude data. The extracted wavelets have a frequency range of 0-70 Hz and a central frequency of approximately 20 Hz.

In order to appraise inversion pitfalls, the same angle-dependent wavelets and wells used to generate the synthetic data were input to the inversion. Figure 3.3 is a comparison of the initial models of elastic properties used for the generation of synthetic pre-stack seismic amplitude data and the inverted 1D distributions of the same parameters. The similarity between initial and inverted models, quantified through the cross-correlation factor, is high for the case of P-impedance, and relatively lower for the cases of S-impedance and density. This exercise suggests that even in the most ideal scenario (isotropic media assumption, noise-free seismic data, wide-angle coverage, and precise knowledge of angle-dependent wavelets and low-frequency models) density distributions are not accurately reconstructed by the inversion, whereas P- and S- impedance distributions remain the most reliable results. Such a behavior is attributed to the intrinsic non-uniqueness of the inversion.

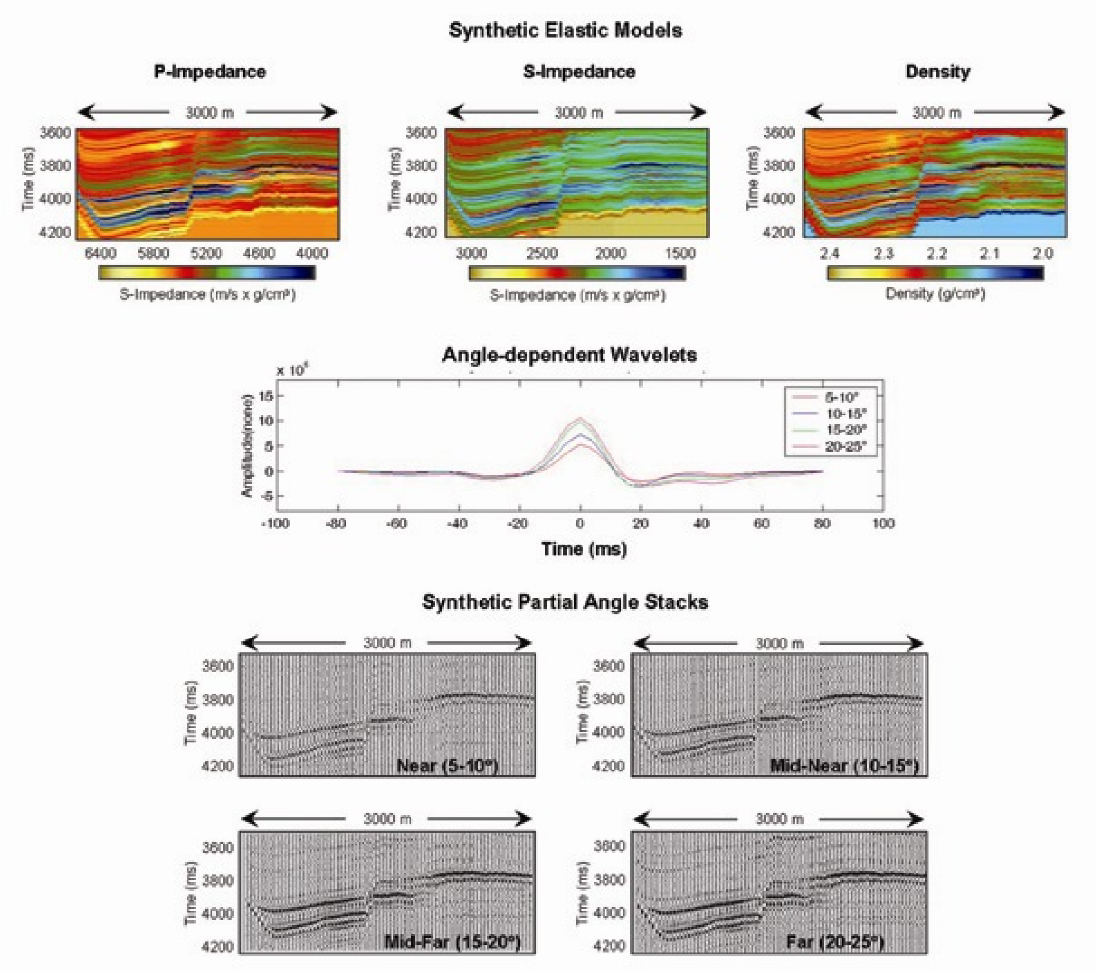

Figure 3.2: Forward modeling of synthetic pre-stack seismic amplitude data: elastic property models (Ip, Is, and ρ), angle-dependent wavelets, and PAS.

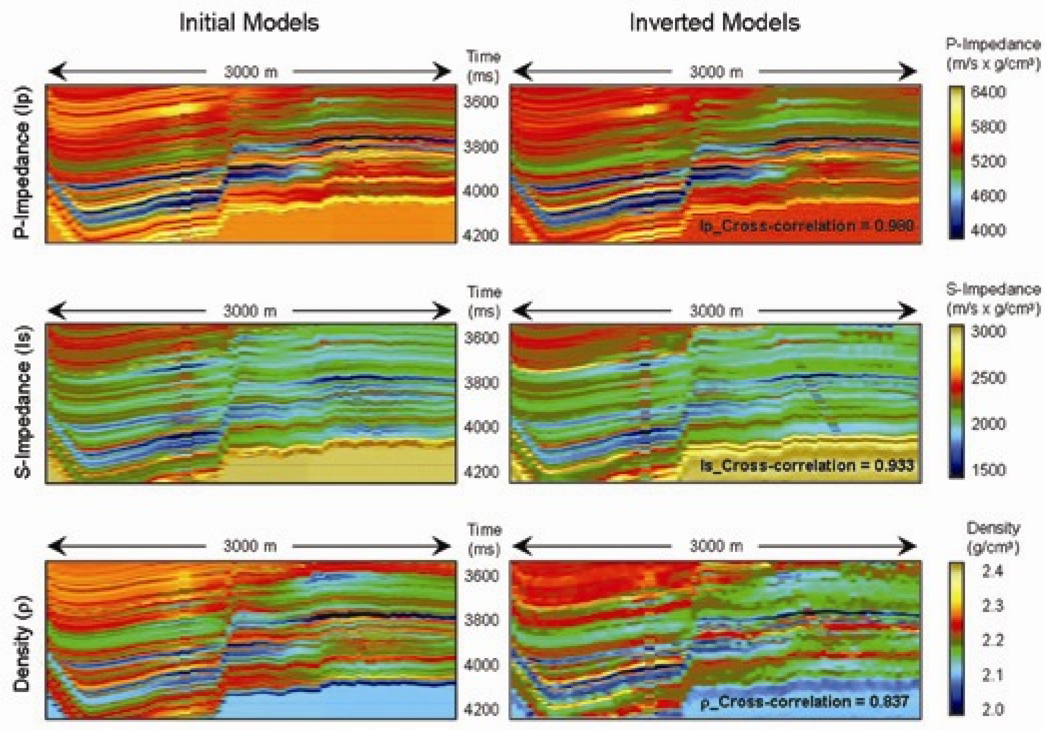

Figure 3.3: Comparison between the initial models of elastic properties used for generation of synthetic seismic data and their inversion results.

3.3.1 Sensitivity Analysis of Angle Coverage

AVA-CSSI inversion was conducted using between one and four PAS to assess the effect of angle coverage on the inversion results. Figure 3.4 shows the inverted P-impedance, S-impedance, and density pseudo-logs extracted at the well location A (Figure 3.1) when two, three, and four PAS are input to the inversion. Well location A was selected for quality control tests throughout this chapter because of the availability of high-quality well-log data common to vertical exploratory wells and because anisotropic effects on P- and S-wave impedances are negligible (this is not necessarily the case along deviated well trajectories). In addition, Figure 3.4 shows the low-pass filtered (0-6 Hz) logs used to generate the low-frequency component of the elastic properties not available from seismic amplitude data and interpolated from well logs. The panels in Figure 3.4 indicate that the low-frequency models numerically interpolated from well-log data only provide the "trend" information required for absolute (full-band) property computation, and that relative (band-limited) information generated from inversion is the main factor providing high-frequency information (6-60 Hz) and high vertical resolution. Accordingly, the vertical resolution of the inverted S-impedance and density pseudo-logs, which are dependent on far-angle reflectivity information, monotonically increases as more far-angle stacks are input to the inversion. On the other hand, P-impedance, which depends solely on normal-incidence reflectivity information, is properly resolved from inversion of near-angle seismic amplitude data.

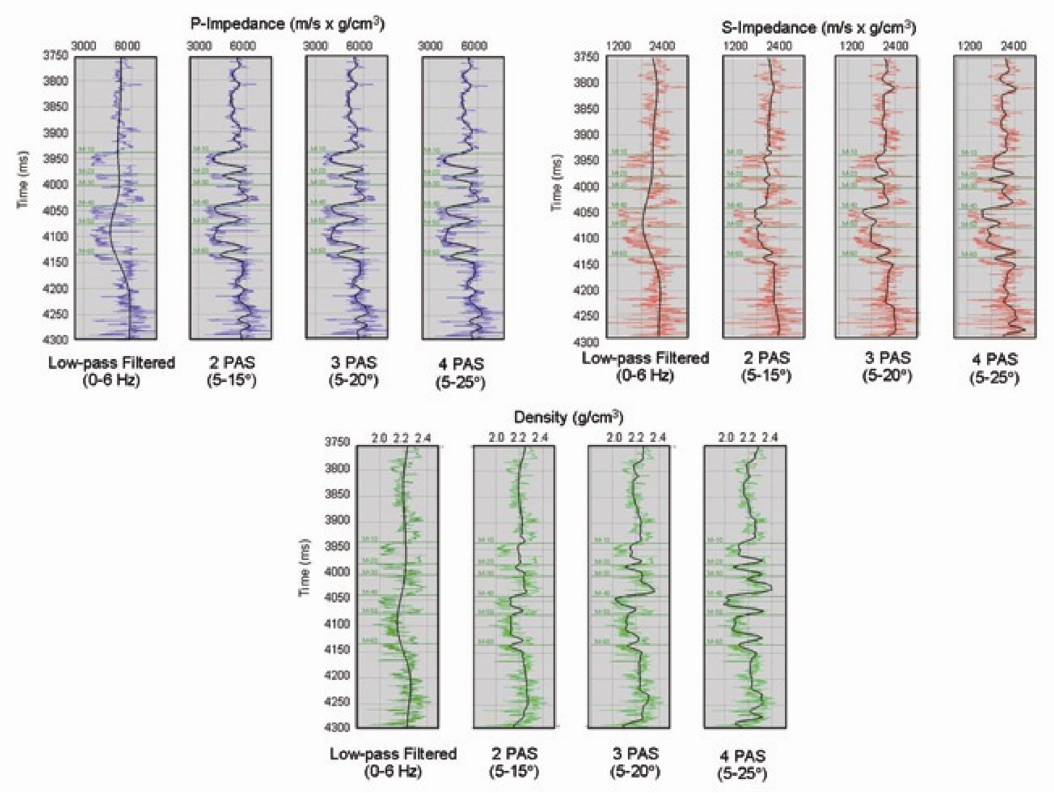

Figure 3.4: Sensitivity of 1D inversion results to angle coverage. Inverted P-wave impedance, S-wave impedance, and density pseudo-logs extracted at well location A. From left to right for each property: the first panel shows the low-pass filtered (0-6 Hz) pseudo-log representing the low-frequency component or trend information not recovered from seismic amplitude data inversion and provided by well-log data; subsequent panels show the inverted pseudo-logs obtained with two, three, and four PAS, respectively.

Figure 3.5 shows the sensitivity analysis of angle coverage based on inverted S-impedance and density cross-sections for increasing ranges of angle coverage. As emphasized by the results shown in Figure 3.4, P-impedance results are not significantly affected by angle coverage and therefore are omitted from consideration in this example. In Figure 3.5, the label "Corr" quantifies the cross-correlation between the original 1D distribution of parameters and the inverted distribution of the same parameters. The vertical resolution of the inverted distributions of S-impedance and density progressively increases as more far-angle stacks are input to the inversion. We remark that the improvement of inversion results is exclusively attributed to the increase of angle coverage since all of the algorithm-related parameters (such as the stabilization parameter "alfa" and the merge frequency) were kept invariant after being selected through sensitivity analysis on the inversion performance criteria; no artificial or empirical correlations were enforced between P-wave velocity, S-wave velocity, and/or density to produce the results shown in Figure 3.5.

The examples above indicate that the vertical resolution of the inverted distributions of S-impedance and density can be improved by including more far-angle stacks into the inversion. This improvement is attributed to the increase of degrees-of-freedom and consequent reduction of non-uniqueness associated with the inclusion of far-angle seismic amplitude data.

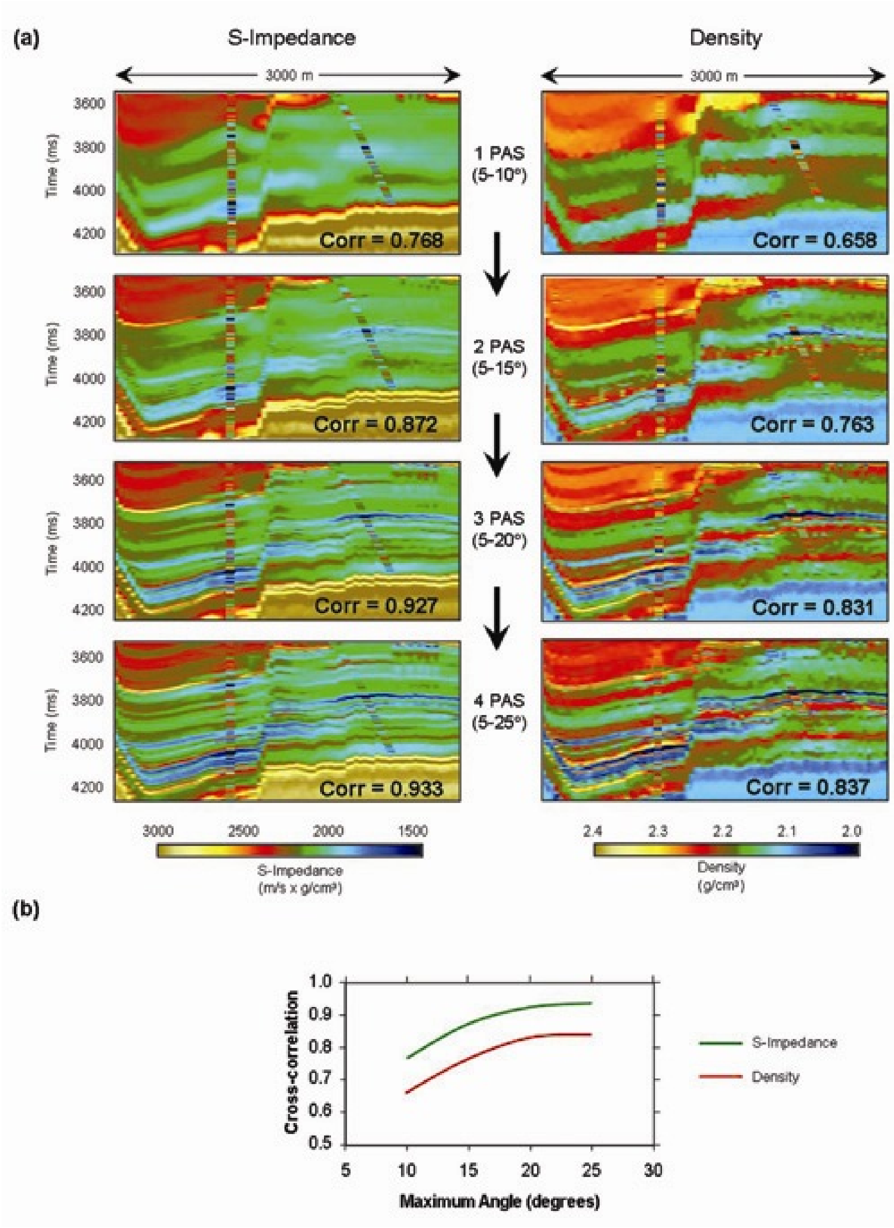

Figure 3.5: Sensitivity of 1D inversion results to angle coverage. Inverted S-impedance and density cross-sections for increasing ranges of angle coverage. The term “Corr” quantifies the cross-correlation between the original model and every inverted model. The accuracy (vertical resolution) of the inverted distributions of S-impedance and density progressively increases as more far-angle stacks are input to the inversion.

3.3.2 Sensitivity Analysis of Wavelets

In order to determine the sensitivity of the inversion results to potential inaccuracies in the description of the wavelets, we applied slight perturbations to the phase and amplitude of the angle-dependent wavelets used to simulate the measurements. The inversions were subsequently performed with the perturbed wavelets to assess the influence of wavelet uncertainty.

Figure 3.6 describes the results from three inversion tests conducted for this sensitivity analysis: (1) using the original wavelets; (2) applying a phase change of 45° to all the wavelets; and (3) applying a scaling factor of 1.5 to all the wavelets. Figure 3.7 shows the results obtained from this exercise in the form of pseudo-logs extracted at well location A. When using the original wavelets (Test 1), the cross-correlation between well-log measurements and the inverted pseudo-logs (model-space cross-correlation) is relatively high for all of the inverted elastic properties, and the order of reliability is as expected: P-impedance followed by S-impedance, and finally density. On the other hand, when a phase change of 45° is applied to all wavelets, the cross-correlation in model space slightly decreases for P-impedance but remains almost invariant for S-impedance and density; additionally, a slight time-shift of about 2-4 ms is observed on all of the pseudo-logs when compared to the inversion results of Test 1. The average cross-correlation in data space (between the input seismic amplitude data and the synthetic PAS generated from inversion results) does not significantly decrease. Finally, when a 1.5 scale factor is applied to all the wavelets, both the data and model space cross-correlations are similar to those obtained for Test 1; only a slight amplitude decrease is observed on all the pseudo-logs when compared to the inversion results of Test 1.

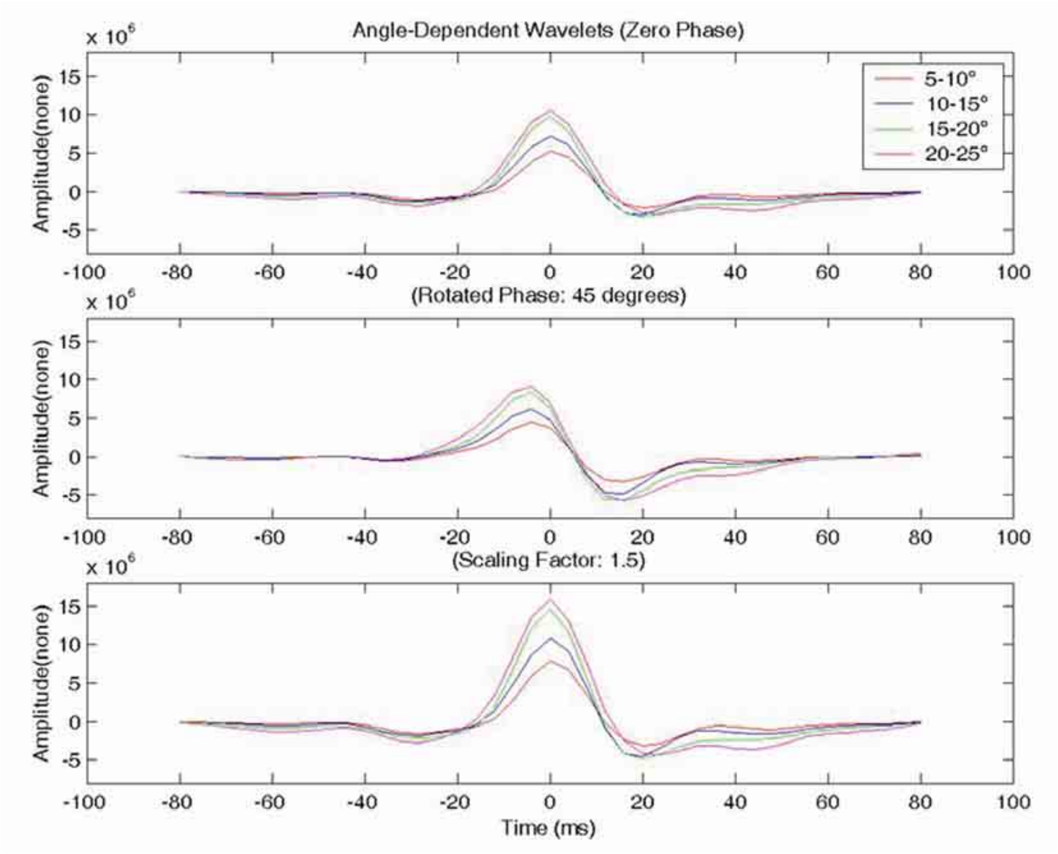

Figure 3.6: Wavelets used for the sensitivity analysis on angle-dependent wavelets. Three inversion tests were conducted: (1) using the original wavelets; (2) applying a phase change of 45° to all wavelets; and (3) applying a scaling change of 1.5 to all wavelets.

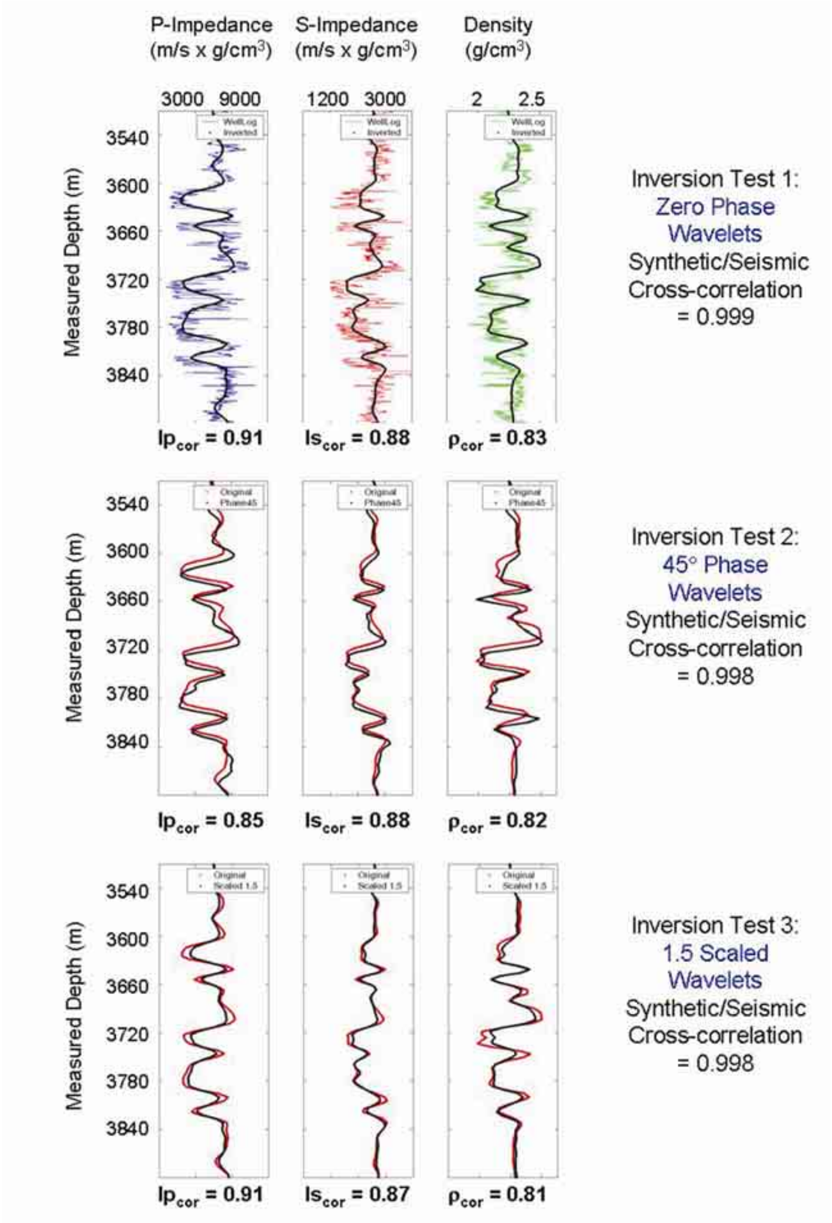

Figure 3.7: Results of the sensitivity analysis on angle-dependent wavelets. Three inversion tests were conducted: (1) using the original wavelets; (2) applying a phase change of 45° to all wavelets; and (3) applying a scaling change of 1.5 to all wavelets.

3.4 AVA SIMULTANEOUS INVERSION OF SEISMIC AMPLITUDE MEASUREMENTS

Seismic amplitude measurements considered in this chapter were sampled at 4 ms and have a frequency band of 6-70 Hz, with a central frequency of 20 Hz. The measured CMP gathers were migrated and corrected for NMO using Kirchhoff pre-stack time-domain migration. In this research, we assume that the migrated and NMO-corrected CMP gathers are devoid of multiple and transmission effects, are not affected by elastic anisotropy, and can be accurately described as the superposition of two-layer plane-wave responses of a stack of horizontal layers. Further, we consider only isotropic PP reflectivity events in the analysis of pre-stack seismic amplitude variations. These assumptions are justified by the quality control previously performed on the migrated and NMO-corrected CMP gathers.

We used a ray-tracing algorithm to transform the pre-stack seismic amplitude data from the offset domain to the incidence-angle domain. We then generated four PAS using the NMO-corrected and migrated offset-gathers and the migration-velocity field. The angle range available from the seismic amplitude data was 6 to 46 degrees; each partial-angle stack was generated using a 10-degree constant range. Final PAS included the following angle ranges: [6-16], [16-26], [26-36], and [36-46].

Given that P- and S-wave sonic and density logs are used for wavelet estimation, low-frequency modeling, and quality control of inversion results through blind well tests, they must be accurately processed and corrected for environmental/borehole effects and invasion. We corroborated the reliability of well logs with quality-control logs such as caliper, tension, and delta-rho logs. Furthermore, synthetic S-wave sonic logs were computed from P-wave sonic logs using empirical Vp-Vs relations similar to those described by Greenberg and Castagna (1992), and compared against measured logs for additional quality control. As will be shown in the following inversion exercises, the excellent correlation found between trace-based inversion results and actual well-log measurements at control well locations (blind well tests) confirmed the reliability of well logs.

The final methodology for inversion of measured pre-stack seismic amplitude data consisted of partial-angle stacking, low-frequency modeling, angle-dependent wavelet estimation, and AVA-CSSI simultaneous inversion (Figure 3.8).

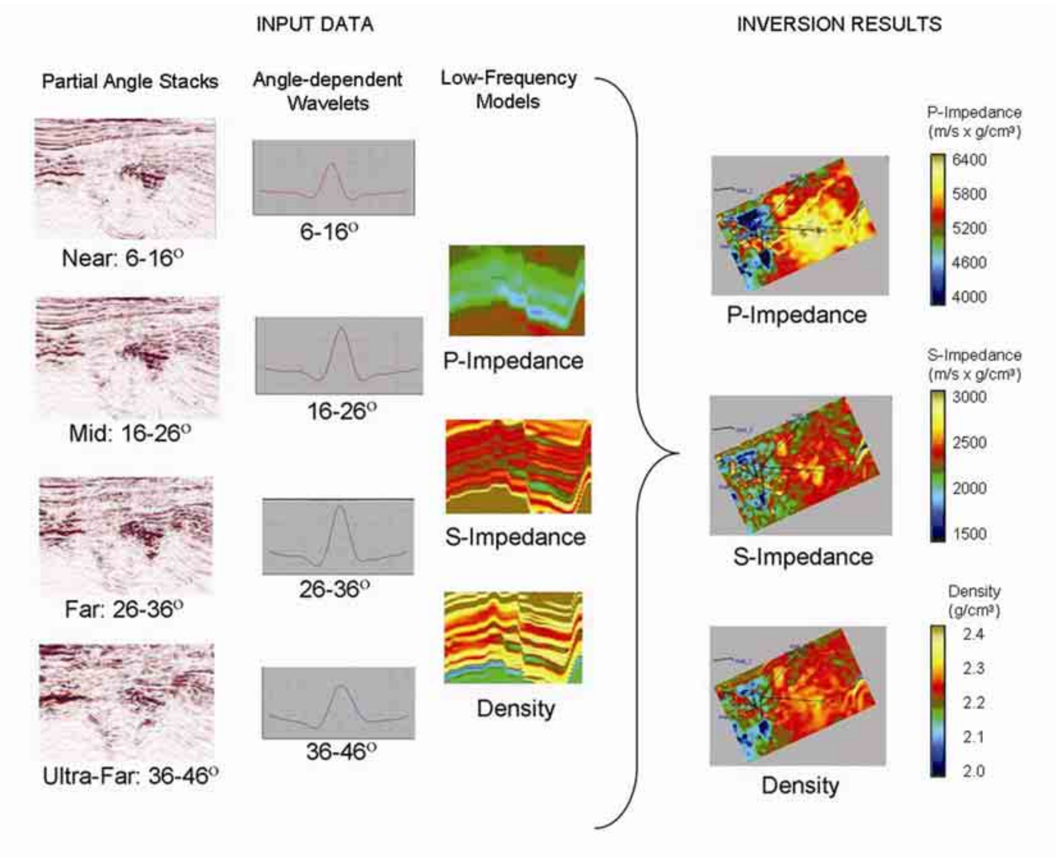

Figure 3.8: Schematic description of the AVA simultaneous inversion methodology: Input data: four partial-angle stacks with the corresponding wavelets (extracted from elastic impedance logs), and low-frequency models of P-impedance, S-impedance, and density (generated from the horizon-guided interpolation of well-log data). Inversion results consist of full-band volumes of P-impedance, S-impedance, and density; they are shown as RMS maps of these properties within the uppermost sand reservoir.

3.4.1 Residual NMO and Time Alignment

Small time-shift corrections were applied to the angle stacks in order to reduce the effect of event misalignment due to processing errors such as residual NMO (Figure 3.9). Subsequently, the corrected PAS were simultaneously inverted using the AVA-CSSI algorithm to quantify the effect of seismic amplitude misalignment on the results. As shown in Figure 3.10, the correction of residual NMO significantly improved the inversion results and uniformly decreased the data misfit for all the angle stacks (thereby increasing the cross-correlation between the measured seismic amplitudes and the synthetic seismic amplitudes simulated from the inversion results).

Figure 3.11 quantifies the improvement of the inversion results in both model and data spaces based on a blind-well test at well location A. In this dissertation, we use the term “blind” to designate wells that have been completely excluded in all phases of the inversion procedure, including wavelet estimation and low-frequency modeling, so they can be objectively used for quality control of inversion results. For the example described in Figure 3.11, the cross-correlation in model space increases by 5% for both S-impedance and density, whereas P-impedance remains almost unaffected by the alignment correction. The data fit is also increased by the residual-NMO and time alignment correction; such improvement is quantified by an increase of the seismic-to-synthetic cross-correlation of approximately 6%.

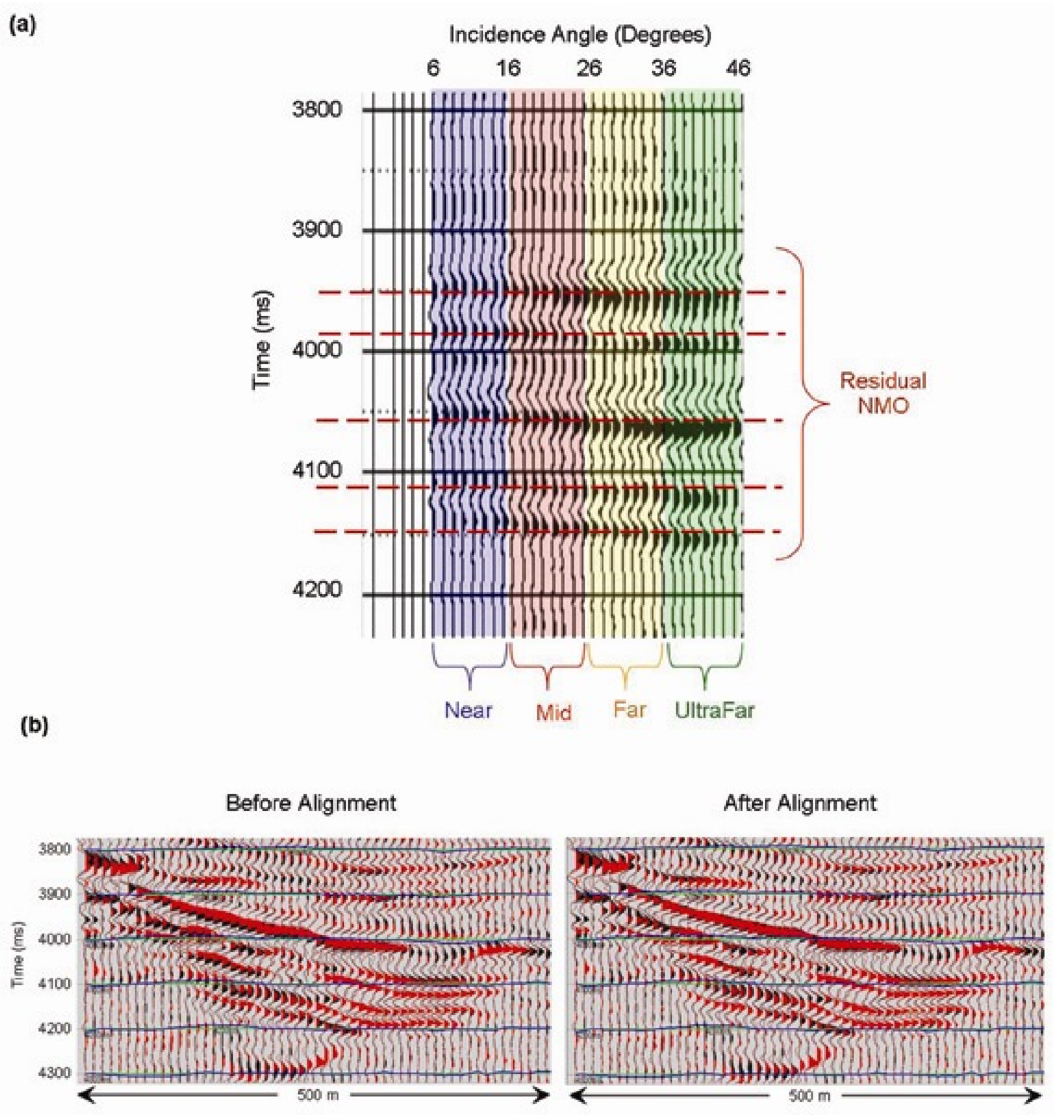

Figure 3.9: Residual NMO and time alignment. (a) Angle gathers showing residual NMO problems. (b) Example of a PAS before and after alignment (red wiggles); black traces represent to the post-stack seismic amplitude data used as the reference volume for time alignment.

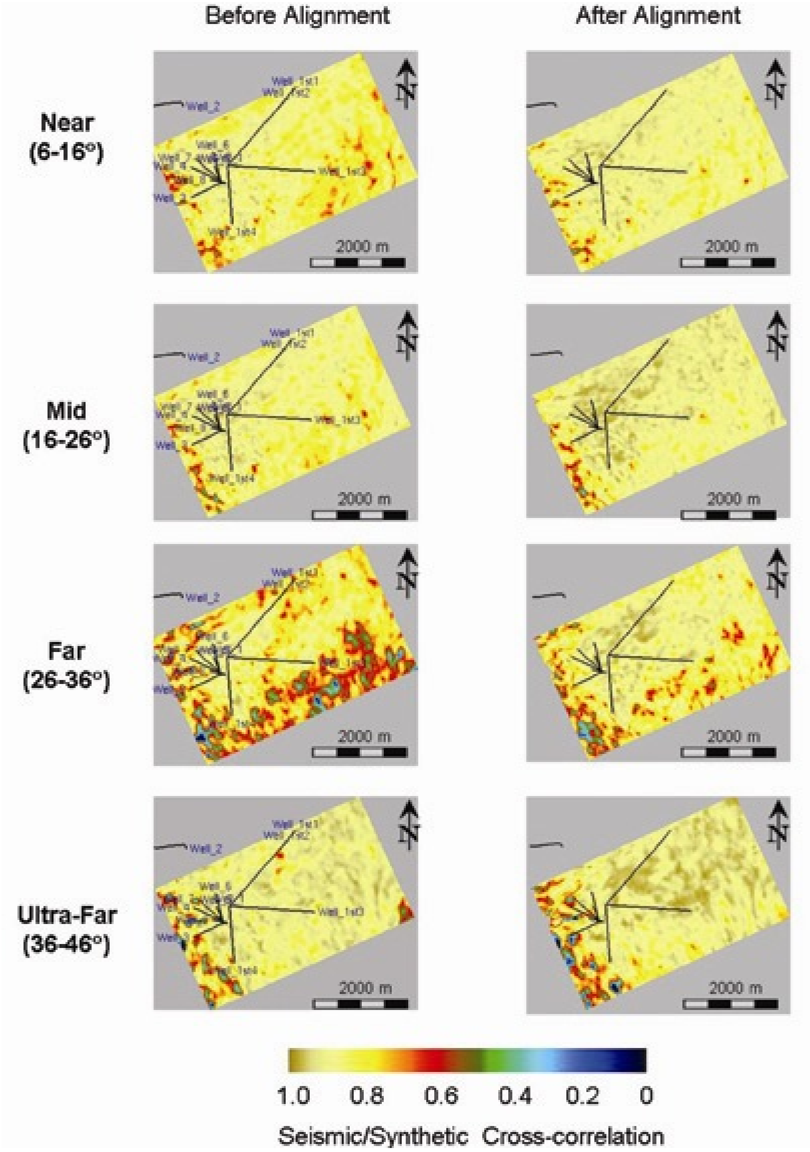

Figure 3.10: Residual NMO and time alignment: Maps of cross-correlation between measured and numerically simulated seismic amplitudes. Simulated seismic amplitudes were generated from 1D inversion results. Cross-correlations significantly improve after the alignment.

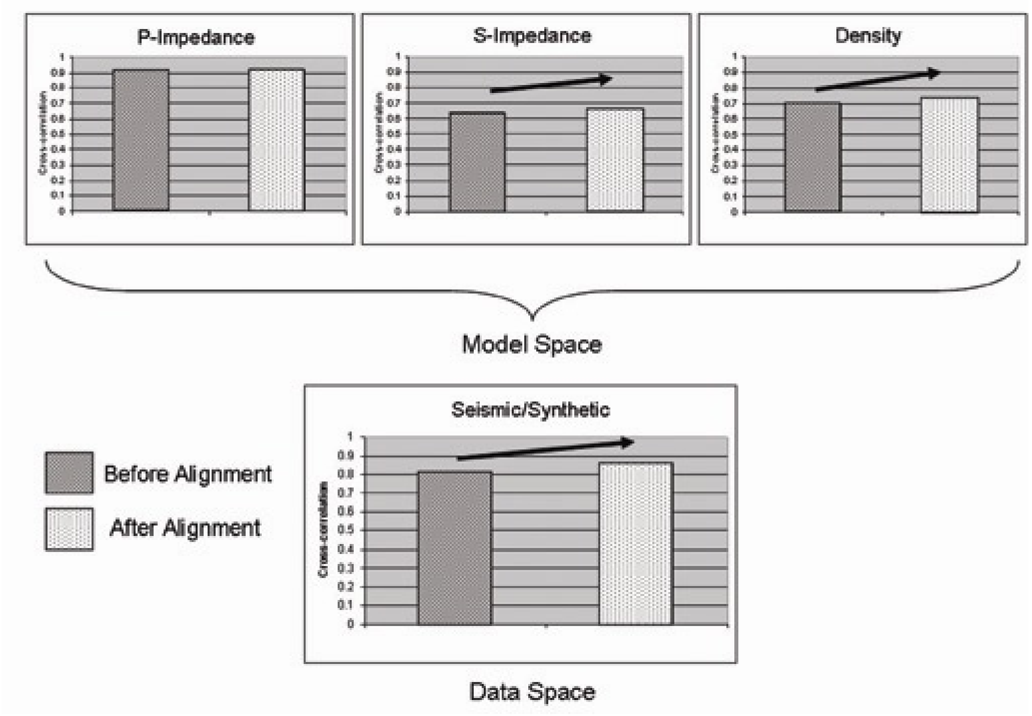

Figure 3.11: Sensitivity of 1D inversion results to residual NMO correction and time alignment: Inversion results are appraised in both model and data spaces.

3.4.2 Velocity Correction and Single-Angle Stacks

The P-wave velocity field used to generate the PAS via ray tracing was initially corrected to honor the shale velocity trend inferred from well logs. Such a correction caused an increase of the P-wave velocity, which in turn decreased the angle coverage from 46 to 35 degrees (Figure 3.12). Subsequently, 30 single-angle stacks were generated using the corrected velocity field for the following angle ranges: 5-6, 6-7, 7-8,…, 32-33, 33-34, and 34-35 degrees. The last 10 far-angle stacks were considered either noisy or devoid of significant signal and hence were excluded from further analysis. We proceeded to align (i.e., to correct for residual NMO) the final set of 20 single-angle stacks (SAS) (5-25 degrees) and to estimate the corresponding angle-dependent wavelets.

Lastly, AVA-CSSI was applied to the corrected seismic amplitude data and the inversion results were compared to the non-corrected inversion products. Figure 3.13 shows the results of this exercise in the form of P-impedance, S-impedance, and density pseudo-logs extracted at well location A, before and after applying the above-described corrections. The figure shows that the inverted S-impedance pseudo-log better resembles the measured well-log curve after applying the corrections. Similarly, density results improve after implementing the correction although not as significantly as in the case of S-impedance; P-impedance inversion results remain almost unaffected by the corrections. We note that, formally, a correction of the low-frequency P-wave velocity field requires a second pass on the migration algorithm before recomputing the corresponding PAS. While this is an interesting proposition that may impair the validity of the procedure described above to recompute the PAS, we leave this subject for detailed consideration in a future study.

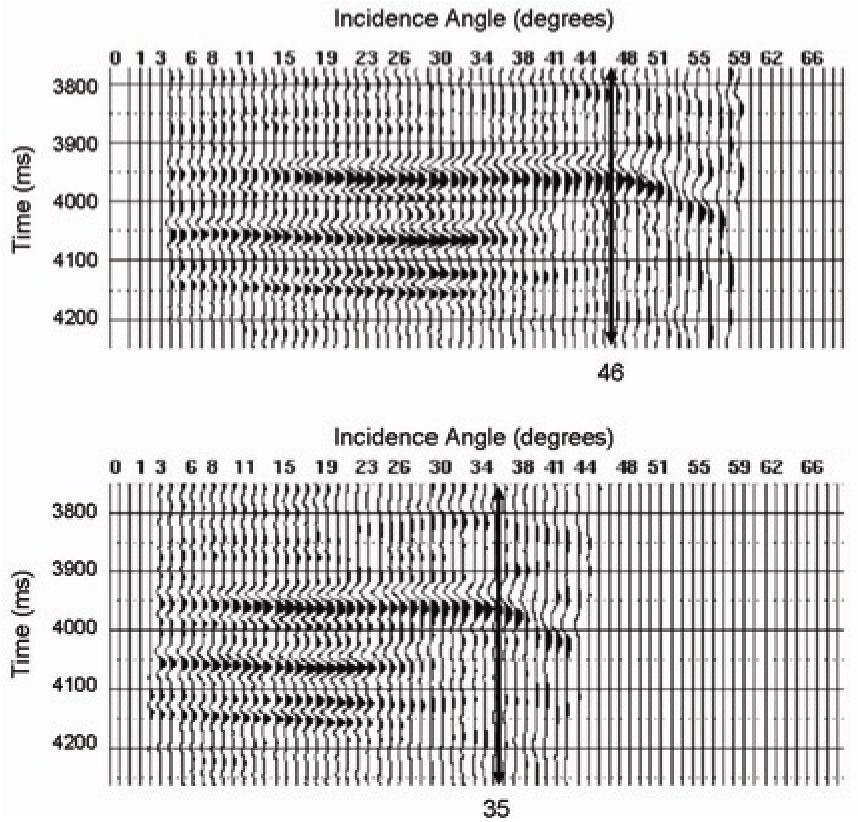

Figure 3.12: Sensitivity of inversion results to the P-wave velocity field used for partial-angle stacking: Angle gathers obtained from non-corrected (upper panel) and well-log-corrected (lower panel) P-wave velocity fields. Black arrows identify the maximum angle used in the inversion.

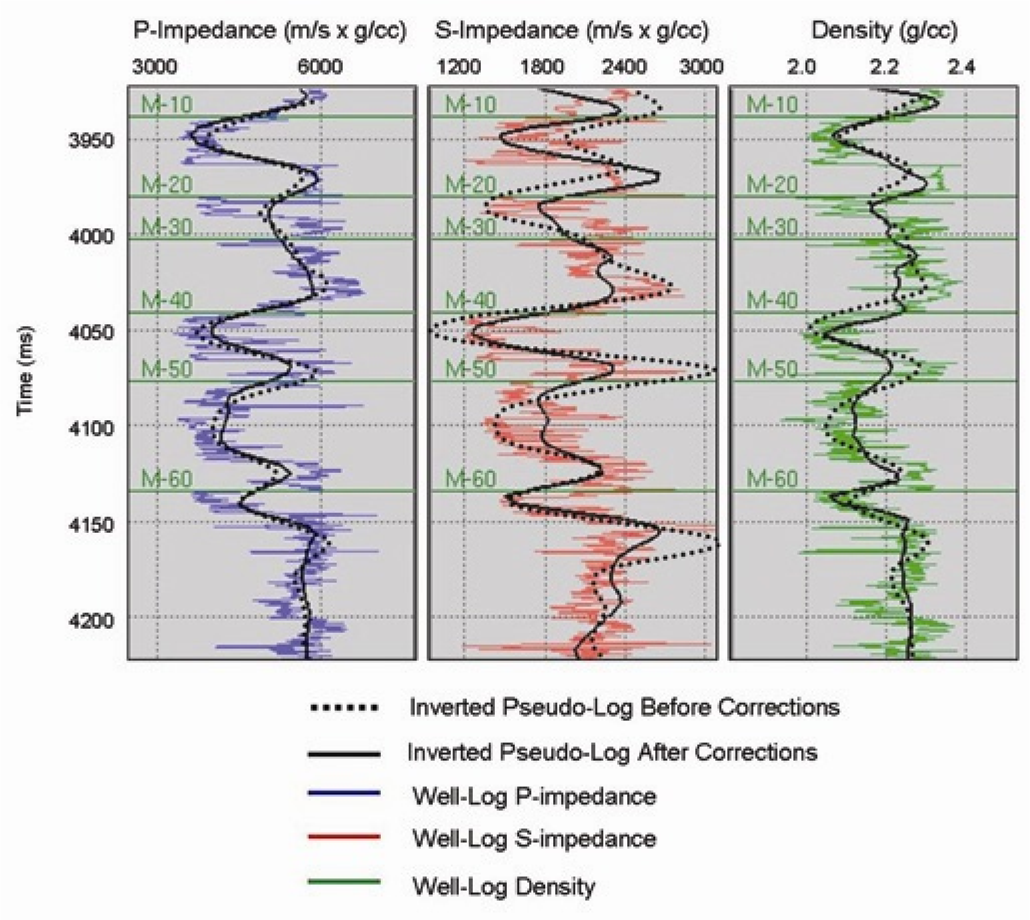

Figure 3.13: Inverted P-impedance, S-impedance, and density pseudo-logs extracted at the well location A (as shown in Figure 3.1), before and after applying the following three corrections: (1) P-wave velocities that match the well-log data, (2) 20 single angle stacks instead of 4 PAS, and (3) exclusion of far-angle data exhibiting low signal-to-noise ratios.

Previous studies indicate that some modulus attributes are more sensitive to fluid and lithology changes than simply P-impedance (Contreras et al., 2006). Therefore, we chose to compare the inversion results in the "*LambaRho*" domain (Figure 3.14), which is the product of the Lamé parameter *Lambda* (λ) and the density (ρ), and can be computed form the inverted P- and S-impedance models using the equation $\lambda\rho=Ip^2\text{-}2Is^2$ (Goodway et al., 1997) as described in Chapter 2. Corrected inversion products exhibit an increase of vertical resolution, which translates into better-delineated stratigraphic features than those obtained from non-corrected inversion results (e.g., the delineation of low $\lambda\rho$ intervals, associated with hydrocarbon-bearing sands, improves considerably after applying the correction). This result is also attributed to the widening of angle coverage and the increasing number of PAS input to the inversion.

As an extension of the above analysis, the P-wave velocity field used to generate the PAS was further corrected to honor the inverted velocity model obtained from the previously described inversion exercise. Since the final velocity field was low-pass filtered (0-3 Hz) to be used for partial-angle stacking through ray tracing, the new P-wave velocity field is equivalent to the "velocity trend" obtained from the low-frequency model initially generated from well-log data and the stratigraphic model. This new velocity correction causes the P-wave velocity field to simultaneously honor the well-log data and the stratigraphic embedding captured by the seismic inversion-based 3D geological model. In turn, the same velocity correction changed the angle coverage from 5-35 to 2-32 degrees.

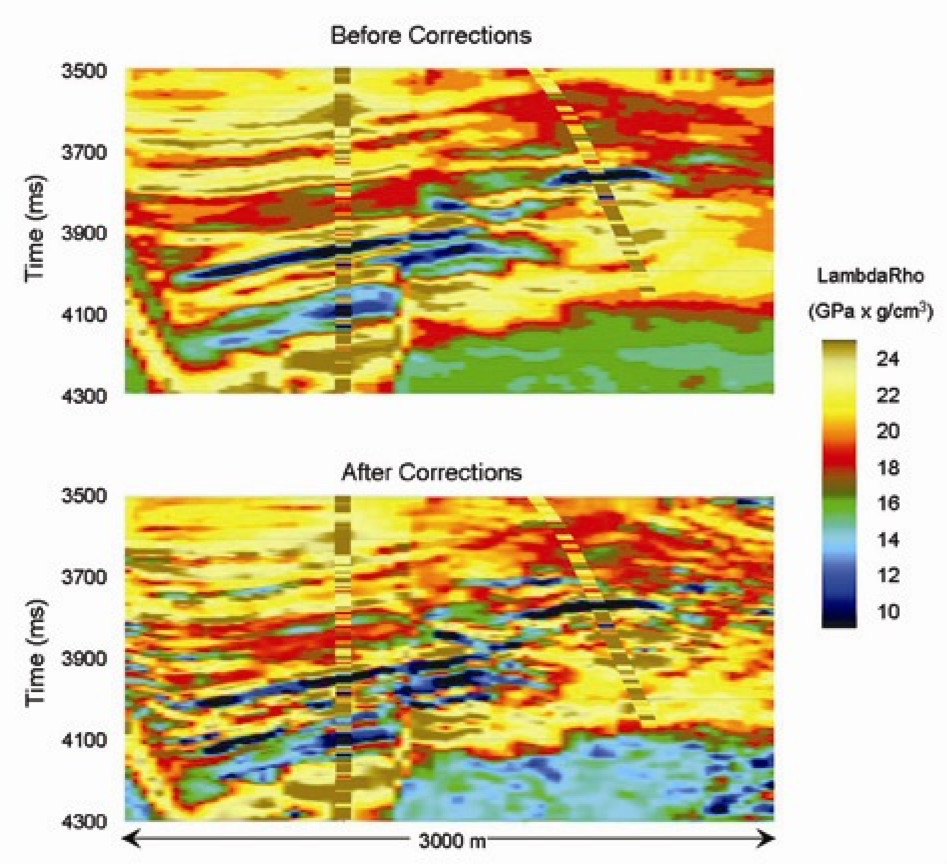

Figure 3.14: Inversion results in the LambdaRho domain: (upper panel) obtained from non-corrected data; lower panel: results obtained by applying the following three corrections: (1) P-wave velocities that match the well-log data, (2) 20 single angle stacks instead of 4 PAS, and (3) exclusion of far-angle data exhibiting low signal-to-noise ratios.

Subsequently, 30 single-angle stacks were generated using the corrected P-wave velocity field for the following angle ranges: 2-3, 3-4, 4-5,…, 29-30, 30-31, and 31-32 degrees. We then repeated the previous procedure in order to generate additional sets of 6 and 3 PAS for the following angle ranges: [2-7, 7-12, 12-17, 17-22, 22-27, 27-32] and [2-12, 12-22, 22-32] degrees, respectively. Next, we proceeded to align (i.e., to correct for residual NMO) the final sets of 30, 6, and 3 angle stacks (all with a range of 2-32 degrees) and to estimate the corresponding angle-dependent wavelets.

The sets of partially-stacked seismic amplitude data described above were used to analyze the effect of both angle coverage and number of PAS on the inversion results. In other words, we sought to determine the optimum maximum angle and number of angle-stacks by analyzing the inversion results in both model (well-blind tests) and data spaces (cross-correlation of synthetic and recorded seismic amplitude data).

Figure 3.15 shows the results obtained from the sensitivity analysis of inversion results to the combined influence of maximum partial-stack angle and number of PAS. As expected, P-impedance results remain almost unaffected by angle range and number of PAS; however, both S-impedance and density cross-correlations significantly improve (5-15%) when the number of PAS increases from three to six; a slight improvement ensues (1-3%) when 30 PAS are included in the set of input data. Similarly, the S-impedance and density cross-correlations monotonically increase with maximum angle up to an “optimum” angle of approximately 24°, where they reach a maximum improvement of approximately

30% to 40% and thence begin to progressively deteriorate despite the fact that angle coverage has increased to 32°. Data space cross-correlations show an initial improvement followed by a decrease, especially in the cases of 6 and 30 PAS; however, the range of improvement in data space is lower than 10%.

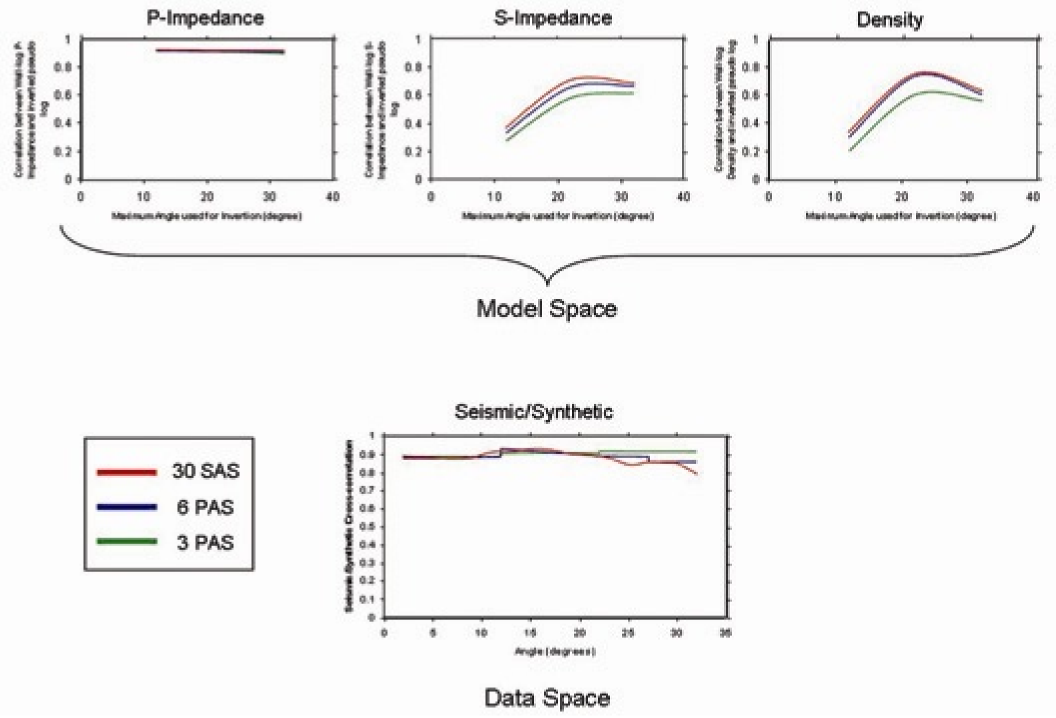

Figure 3.15: Simultaneous sensitivity analysis on maximum angle used for inversion and number of partial-angle stacks.

This exercise suggests that detailed sensitivity analysis on the number of PAS is required for optimal inversion results. In addition, we conclude that single-angle stacking is preferred over angle-range stacking for high-quality (low signal-to-noise ratio) seismic amplitude data sets. Sensitivity analysis of inversion results to the maximum stacking angle indicates a decrease of the vertical resolution of the inversion results after the "optimum" maximum angle is reached. This anomalous behavior is due to the low signal-to-noise ratios of far-angle seismic amplitude data.

Tables 3.1 and 3.2 summarize the results obtained from the different sensitivity analyses conducted on synthetic and measured seismic amplitude data, respectively. Exercises with synthetic data indicate that the vertical resolution of the inversion results initially improves with an increase of maximum stack angle. By contrast, exercises with recorded seismic amplitude data indicate that presence of noise in far-angle stacks decreases the vertical resolution of the inversion results.

Table 3.1: Summary of the sensitivity analysis on data-related factors controlling AVA simultaneous inversion of synthetic PAS. Optimum factors (associated with the highest cross-correlation values) are highlighted in boldface.

Factor	**Model Space (Measured/Pseudo Logs Cross-Correlation)**			**Data Space (Seismic/Synthetic Cross-correlation)**
	P-impedance	**S-impedance**	**Density**	
Maximum Angle, using Partial Angle Stacks (PAS)				
1 PAS (5-10°)	0.966	0.768	0.658	0.994
2 PAS (5-15°)	0.966	0.872	0.763	0.999
3 PAS (5-20°)	0.966	0.927	0.831	0.999
4 PAS (5-25°)	**0.966**	**0.933**	**0.837**	**0.999**
Wavelet Perturbation				
Case 1: No Change	**0.910**	**0.880**	**0.830**	**0.999**
Case 2: Phase Change = 45 °	0.850	0.880	0.820	0.998
Case 3: Scaling Factor = 1.5	0.910	0.870	0.810	0.998

Table 3.2: Summary of the sensitivity analysis on data-related factors controlling AVA simultaneous inversion of recorded partially-stacked seismic data. Optimum factors (associated with the highest cross-correlation values) are highlighted in boldface.

Factor	**Model Space (Measured/Pseudo Logs Cross-Correlation)**			**Data Space (Seismic/Synthetic Cross-correlation)**
	P-impedance	**S-impedance**	**Density**	
Maximum Angle, using Single Angle Stacks (SAS)				
10 SAS (2-12°)	0.912	0.372	0.342	0.916
20 SAS (2-22°)	**0.916**	**0.701**	**0.756**	**0.910**
30 SAS (2-32°)	0.913	0.686	0.636	0.885
Number of Seismic Angle Stacks (Constant angle range: 2-32°)				
3 PAS	0.898	0.614	0.563	0.906
6 PAS	0.908	0.669	0.612	0.894
30 SAS	**0.913**	**0.686**	**0.636**	**0.885**
Velocity Correction				
Before Correction	0.871	0.569	0.600	0.859
After Correction	**0.913**	**0.660**	**0.742**	**0.860**
Time Alignment of Partial Angle Stacks				
Before Alignment	0.913	0.640	0.689	0.815
After Alignment	**0.917**	**0.660**	**0.742**	**0.860**

3.5 SUMMARY

This chapter considers Amplitude-versus-Angle (AVA) simultaneous one-dimensional inversion of synthetic and recorded seismic amplitudes to appraise the influence of several data factors controlling the vertical resolution, reliability, and non-uniqueness of the estimated distributions of elastic properties. Detailed sensitivity analysis of synthetic amplitude data indicates that, even in the most ideal scenario (perfectly migrated data, isotropic media assumption, noise-free seismic amplitude data, availability of far-angle coverage, and precise knowledge of angle-dependent wavelets and low-frequency components) input elastic models used to generate the synthetic seismic amplitudes are not accurately reconstructed by the inversion. This result is attributed to the intrinsic non-uniqueness of the inverse problem. The order of reliability of the inverted properties is P-impedance, followed by S-impedance, and bulk density. Additionally, the availability of sufficient far-angle coverage remains crucial for the reliable estimation of one-dimensional distributions of S-impedance and bulk density. We show that time alignment of partial-angle stacks for correcting residual NMO effects significantly improves the vertical resolution of the estimated spatial distributions of elastic parameters and consistently decreases the data misfit. Finally, we find that the reliability of the inverted distributions of elastic parameters can be substantially improved by (1) increasing the preserved AVA information via multiple single-angle stacks, (2) correcting the P-wave velocity field for partial-angle stacking, and (3) excluding far-angle data with low signal-to-noise ratios.

Chapter 4: AVA Stochastic Inversion: Algorithm Description and Sensitivity Analysis

4.1 INTRODUCTION

The main objective of this chapter is to describe, through detailed sensitivity analysis, the main characteristics and potentialities of a novel stochastic inversion algorithm that integrates pre-stack seismic data, well logs, geological information, and geostatistical data into multiple, equi-probable, and high-resolution reservoir models of elastic and petrophysical properties. The field data example considered to this end is Anadarko's Marco Polo deepwater development project.

Conventional geostatistical techniques used to fill the spatial gap between well locations rely heavily on sequential simulation (Chilés and Delfiner, 1999). The disadvantage of these procedures is that the *a-priori* assumptions about spatial smoothness and continuity heavily bias the simulated properties. Moreover, tests with blind wells usually yield poor correlations even with the use of external drift constraints such as seismic attributes.

On the other hand, well logs exhibit a radial length of investigation shorter than 3 m and hence provide limited indication of lateral extent and continuity of reservoir flow units. In the past, post-stack seismic amplitude data have been used to fill the spatial gap between sparse well locations (Torres-Verdin et al., 1999). However, post-stack seismic amplitude data respond solely to acoustic impedance (the product of bulk density and P-wave velocity) and, therefore, cannot always uniquely discriminate between spatial variations of porosity, layer thickness, shale concentration, and fluid saturation. Pre-stack seismic amplitude data, on the other hand, are sensitive to S-wave velocity and bulk density in addition to P-wave velocity. The additional sensitivity provides the degrees of freedom necessary to interpret lateral variations of pre-stack seismic amplitude in terms of spatial variations of petrophysical properties and flow-unit thickness.

In an effort to appraise the reliability of AVA stochastic inversion products we performed a detailed sensitivity analysis of the main factors controlling the inversion algorithm. We first described the main characteristics of the stochastic inversion algorithm, and then applied AVA stochastic inversion to synthetic partial-angle stacks and recorded pre-stack seismic amplitude measurements. Finally, multiple realizations were produced and statistically evaluated to assess the non-uniqueness and uncertainty of the results.

4.2 AMPLITUDE VERSUS ANGLE (AVA) STOCHASTIC INVERSION

4.2.1 Inversion algorithm

The selection of the new stochastic inversion algorithm was motivated by the requirements that it should: (1) work iteratively on a fully filled grid; (2) be capable of working side by side with user-defined *a-priori* information; (3) produce predictable, high-quality results that can realistically be understood in the context of a well-defined conceptual model; and (4) deal thoroughly with the uncertainty left over after all the seismic amplitude data, well logs, and other available measurements have been taken into account.

The new stochastic inversion technique considered in this chapter is based on a Bayesian search criterion (Tarantola, 2005) that makes use of Markov-Chain Monte Carlo (MCMC) methods (Gilks et al., 1996) to progressively update elastic properties on the simulation grid. It combines the Gauss random field conceptual model underlying conventional geostatistics with iterative local updates of nonlinear minimization. Moreover, the inversion implements transformed Gaussian covariance matrices and efficient projection operations via fast Fourier transforms to populate petrophysical properties in the simulation grid. The algorithm additionally implements a geostatistically correct "semi-variogram constraint."

4.2.2 Simulated elastic properties and lithotypes

The MCMC inversion algorithm implemented in this dissertation can handle both post- and pre-stack seismic amplitude data. When post-stack seismic amplitude data are inverted the simulated property is P-impedance (I_P), also known as acoustic impedance (AI); whereas inversion of pre-stack amplitude data produces models of P-velocity (V_P), S-velocity (V_S), and density (ρ).

In addition to elastic properties, the stochastic inversion algorithm allows us to simulate lithological distributions. The lithotypes are generated using a novel approach that simulates continuous "lithology control fields", as special, non-physical base properties, and then derive lithotypes from them by thresholding. The mutual-thresholding approach consists of defining as many continuous lithology control fields as there are rock types, and then label the lithology of each grid cell to be the rock associated with the control field with the largest value at that point. The boundaries between bodies in the lithology cube are “contours” along which the largest two control fields take the same value.

One significant advantage of driving the lithology indirectly via a set of continuous fields is that it makes it possible to make non-local updates: block changes to the control field translate naturally into block changes to the lithology field, i.e., changes to body patterns and boundaries at more than one pixel. This is one of the key reasons why the new stochastic inversion algorithm is much better at inverting for lithology than commonly used algorithms based on indicator kriging: it can call whole bodies into existence in order to account for the seismic amplitude data, rather than attempting to piece them together point by point, via intermediate states that may actually impair the results.

The algorithm provides ways of specifying some quantitative properties the geoscientists believe the lithology field should have. One important quantitative property that can be specified based on the geoscientist criteria is the relative proportion in which each lithotype appears, also known as lithotype fraction. In the case of the mutual-thresholding model, the desired mix can be achieved by adjusting the relative means of the control fields.

The main difficulty with discrete simulation is that it is not possible directly to specify an exact indicator variogram. One alternative is to specify a variogram for the continuous field(s) underlying the simulation; however, the effect of the thresholding operation on the effective indicator variogram is to depress and sharpen it (i.e., making it a shorter variogram). Although indicator variograms are not in themselves a complete answer to the question of how to specify the lithology field, especially since the empirical variograms measured from widely spaced wells are very uncertain, they are nevertheless of interest to geoscientists. The proposed approach is obtaining indicator variograms by rapid simulation, via fast Fourier transform (FFT), to generate many unconditional simulations from the model and to compute indicator variograms from them.

4.2.3 Seismic amplitude and well-log data

The stochastic inversion algorithm described in this chapter requires the input pre-stack seismic amplitude data to be organized into aligned partial-angle stacks (PAS). Angle-dependent wavelets estimated from the PAS are also required for the forward modeling of the synthetic seismic data from the inverted elastic models through the convolutional model.

Knowledge of the noise-to-signal ratio of the seismic amplitude data is also required as an input, since the inversion algorithm does not stop when it achieves a particular degree of “convergence,” i.e. low seismic residuals; instead, it aims to make the residuals fluctuate within the statistical range defined by the user’s estimate of the noise-to-signal ratio.

Since the input well data are assumed to be accurately processed and corrected for environmental/borehole effects and invasion, they are considered to be “hard” data representing the “true” response of the earth; accordingly, it represents of the main components of the inversion algorithm and honored by the inversion solution.

As will be further explained in the next topic, well-log data are also used to assemble geostatistical information in the form of the joint probability distributions of elastic properties (Vp, Vs, and ρ).

Lastly, lithotype logs (sand/shale in our case), generated from lithology-sensitive logs such as volume-of-shale (Vsh), are necessary for discrimination of the elastic properties in lithologic groups.

4.2.4 Geostatistical data

As previously described, the geostatistical information is gathered in the form of 3D joint probability distribution functions (PDFs) of elastic properties (P-velocity, S-velocity, and density). Such PDFs are generated from well-log data using a lithotype-dependent multivariate statistical approach. The methodology consists of generating 1D sample histograms from well logs for each elastic and petrophysical property and then combining the information into layer- and lithotype-dependent multidimensional (3D) joint distributions (Figures 4.1 and 4.2). The aim of this methodology is to capture all the relationships and correlations between the three elastic properties (Vp, Vs, and ρ).

Additionally, variograms are used to describe the spatial variability of the elastic properties to be inverted. Sample variograms can be computed from well-log data and/or previously computed volumes of elastic properties. In addition, spatial information from 3D seismic amplitude data and geologic information can be incorporated in the final modeling of the variograms. Moreover, detailed sensitivity analysis is the preferred approach for the determination of the more suitable variogram type and optimum variogram elements such as lateral and vertical range.

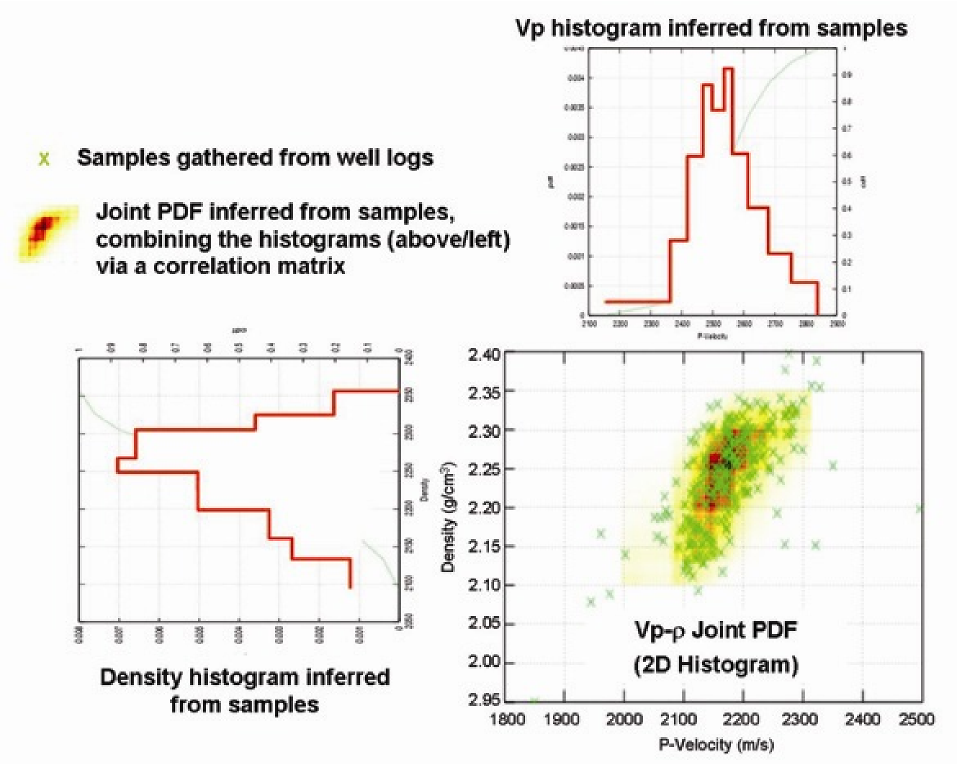

Figure 4.1: Example of a joint Vp-ρ probability density function (PDF) constructed from 1D sample histograms of the properties (above and left) via a correlation matrix. The samples are gathered from well-log data and then separated into lithotype groups.

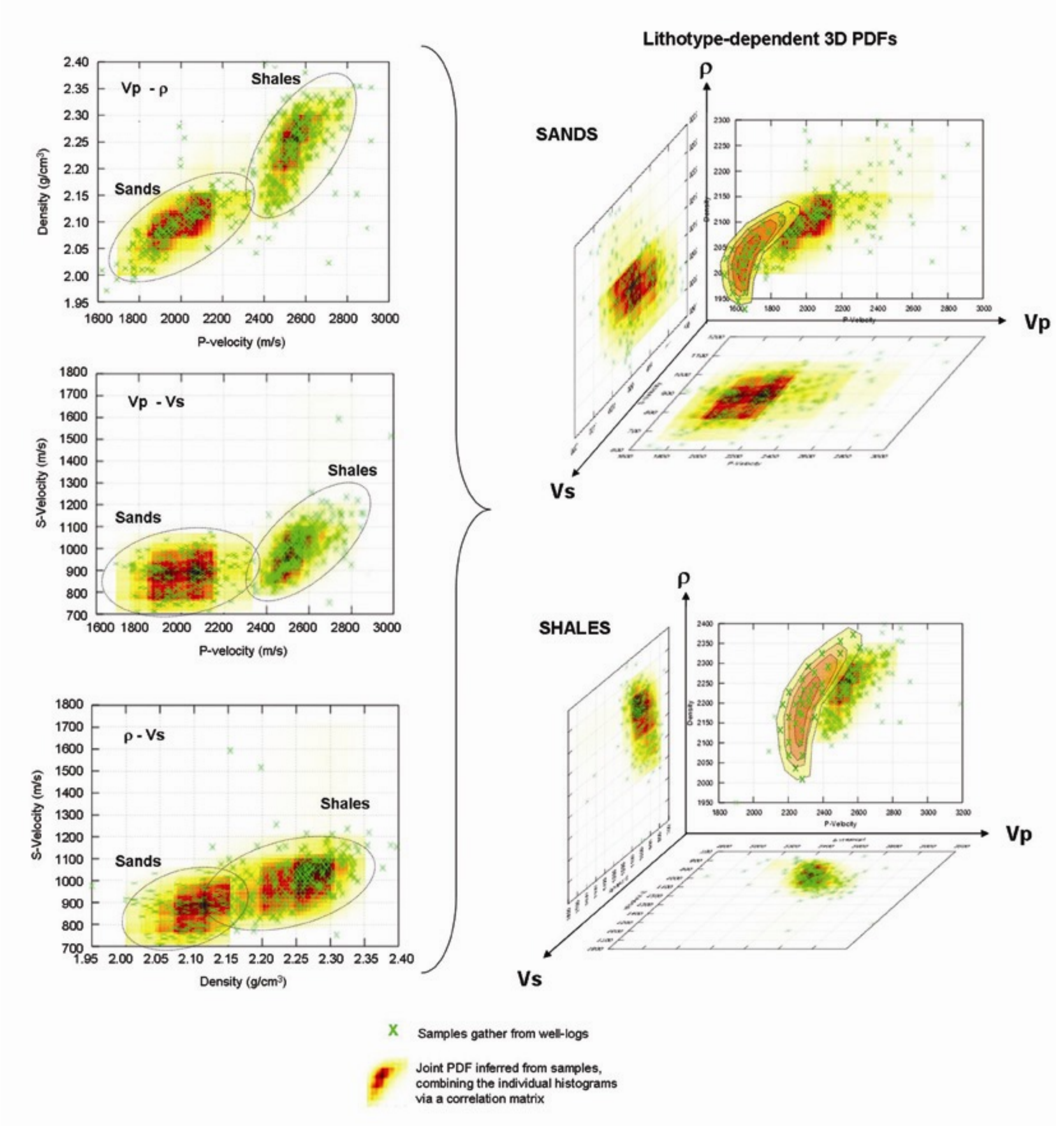

Figure 4.2: Example of multidimensional joint probability density functions (PDFs) constructed from well-log data. Crossplots represent Vp-ρ, Vp-Vs, and ρ-Vs 2D joint PDFs derived from 1D sample histograms; the statistics from both lithotypes (sands/shales) are simultaneously shown. 3D plots correspond to lithotype-dependent joint PDFs of elastic properties (Vp, Vs, and ρ) produced by integrating of the information to the right and discriminating between lithotypes.

4.3 SYNTHETIC DATA EXAMPLE

Synthetic pre-stack seismic amplitude data were generated using well-log data, angle-dependent wavelets, and the structural/stratigraphic embedding of the Marco Polo Field. Initially, 3D models of elastic properties (P-velocity, S-impedance, and density) were numerically interpolated from well-log data following a structural/stratigraphic geological model that enforced a 4-ms micro-layering as the sampling rate. Subsequently, the elastic models were used to produce four synthetic PAS for the angle intervals [5-10°], [10-15°], [15-20°], and [20-25°], via AVA reflectivity modeling with Knott-Zoeppritz's two-layer reflectivity equations and by subsequent convolution with the corresponding angle-dependent wavelets (Figure 4.3).

The wavelets used in this exercise were estimated from recorded PAS in order to consider realistic amplitude and frequency values, and to make the synthetic inversion results comparable to subsequent inversion tests on recorded seismic amplitude data. The extracted wavelets have a frequency range of 0-70 Hz and a central frequency of approximately 20 Hz. In order to appraise inversion pitfalls, the same angle-dependent wavelets and wells used to generate the synthetic data were input to the inversion.

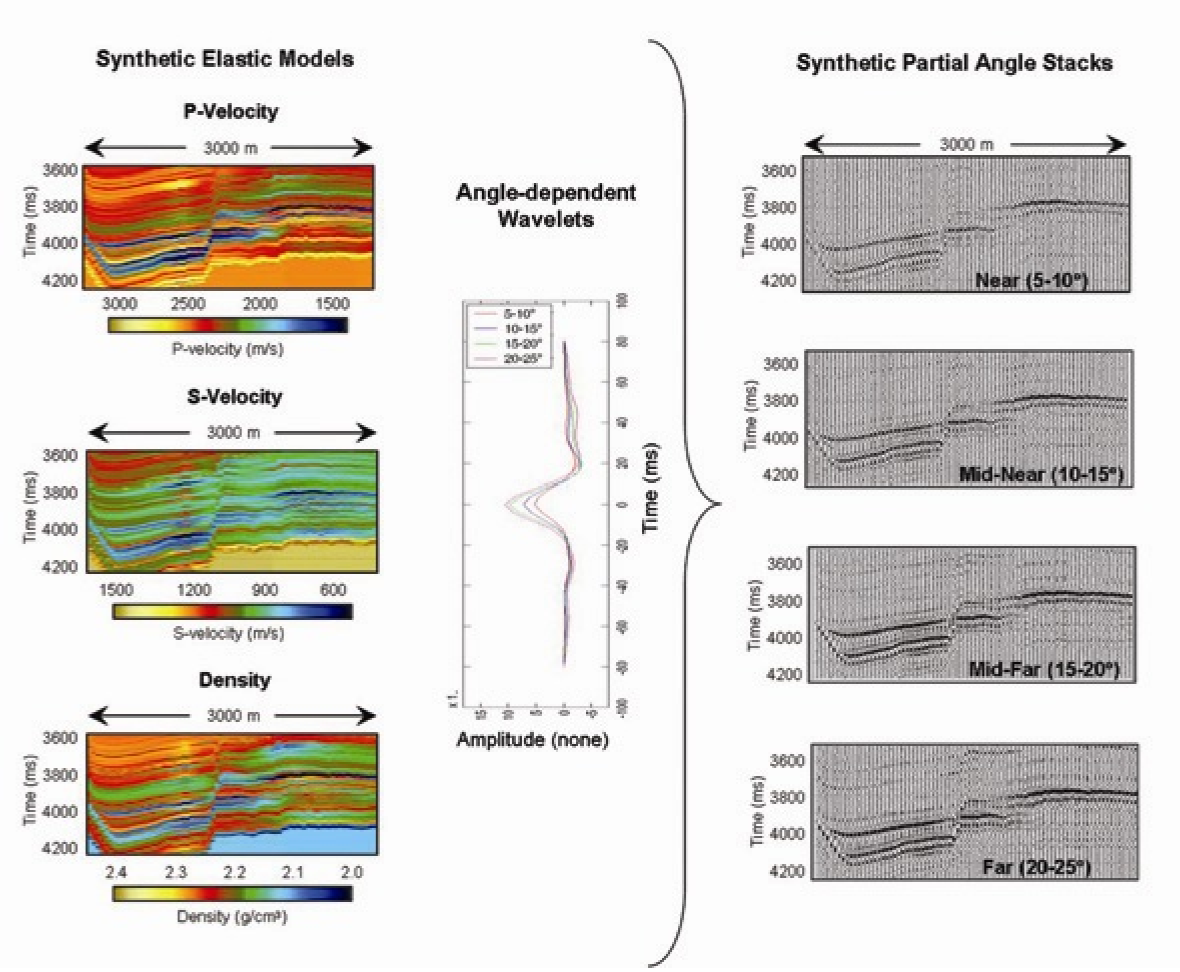

Figure 4.3: Forward modeling of synthetic pre-stack seismic amplitude data: elastic property models (Vp, Vs, and ρ), angle-dependent wavelets, and PAS.

The synthetic partial-angle stacks were simultaneously inverted with well logs using the previously described AVA stochastic inversion algorithm. The pre-stack stochastic inversion algorithm was implemented with the same stratigraphic/structural framework used for generation of the elastic models. Input data consisted of: (1) four partial-angle stacks and angle-dependent wavelets for the previously described angle ranges; (2) lithotype, Vp, Vs, and density logs for three well locations (one vertical and two deviated), and (3) well-log generated geostatistical information in the form of variograms and 3D PDFs of properties. The results of the AVA stochastic inversion consist of multiple, equi-probable, 3D distributions of elastic properties (Vp, Vs, and density) and lithotypes (sand/shale). Figure 4.4 is a schematic representation of the input data and inversion results previously described.

Finally, the main advantage of analyzing a synthetic data set is that the initial "true" elastic models, from which the seismic amplitude data was originated, are completely known; therefore, the accuracy of the inversion results can be reliably quantified in the model space, without relying on localized blind well tests. Multiple examples of this quantitative approach for quality control will be shown in the following sensitivity analyses.

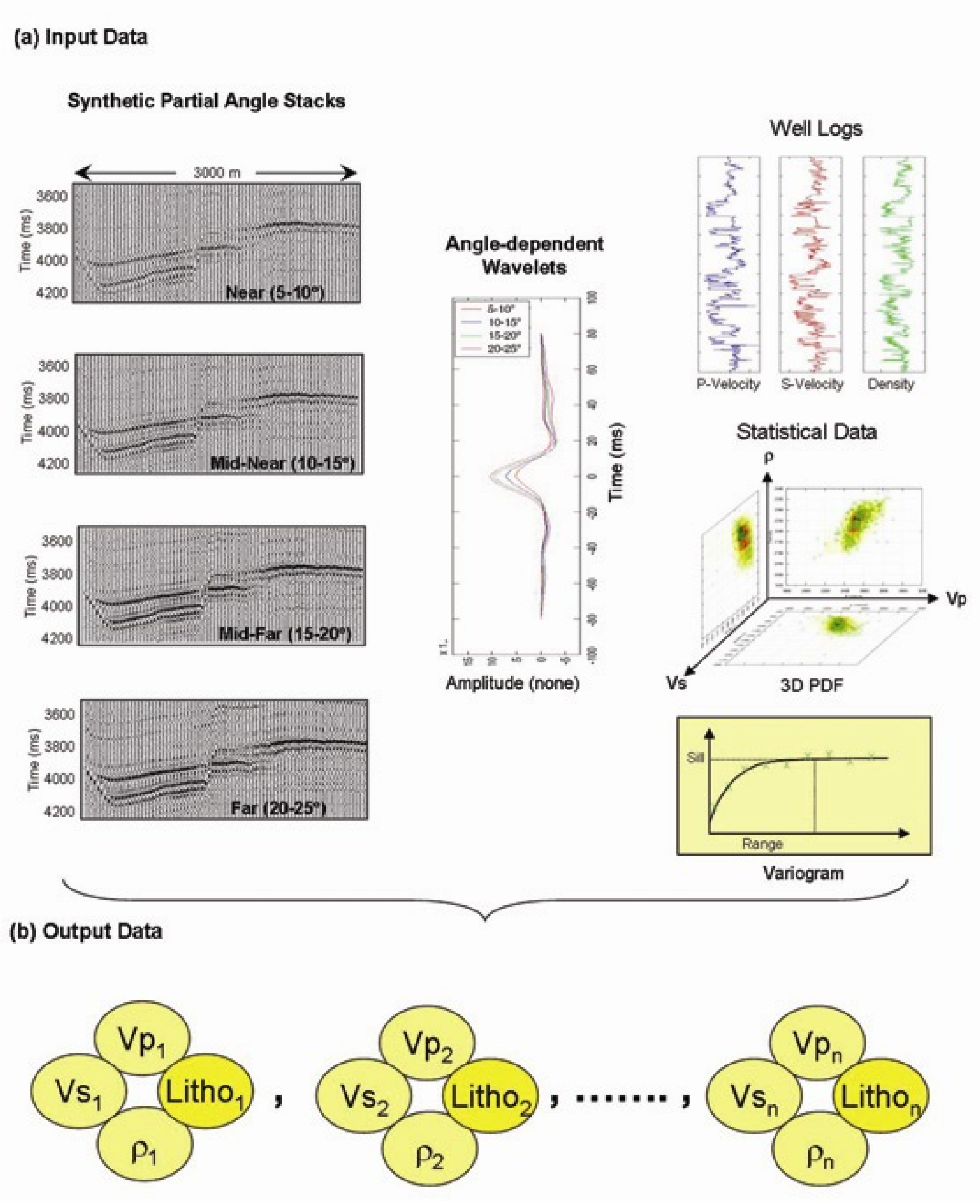

Figure 4.4: Schematic representation of the input and output data involved in pre-stack stochastic inversion: (a) Input data: partial-angle stacks, angle-dependent wavelets, well-logs of Vp, Vs, ρ, and lithotypes; and 3D PDF's of elastic properties and variograms (lithotype- and layer-dependents); (c) Outputs: multiple equi-probable volumes of Vp, Vs, ρ, and lithotypes.

4.3.1 Sensitivity analysis of elastic property transforms

The 3D joint probability distributions of elastic properties generated from well-log data represent the statistical information that define the range of possible elastic property values to be stochastically simulated as well as the intrinsic relationships among them. In that sense, the quality of the well-log data will directly affect the accuracy of those distributions, and consequently, the reliability of the inversion results.

In order to quantify the effect of 3D PDFs on the inversion results, a sensitivity analysis of the elastic property transforms was carried out using well-log data from different sets of wells. The maps shown in Figure 4.5 represent the average model space cross-correlation between the original "known" elastic models (used to generate the synthetic PAS) and their corresponding inverted models. In addition, this figure shows the average cross-correlation in the data space between the input seismic amplitude data (input synthetic PAS) and the analogous synthetic PAS generated from the inversion results.

Two different scenarios for PDFs generation were considered: (1) exclusively using logs from the well location A; and (2) simultaneously using the logs from the vertical well A and from all of the other deviated wells. The S-velocity and density cross-correlations significantly improve (about 8-10 %) when only the data from well A are used, whereas P-velocity and the data space correlations remain invariant. These results are attributed to the relatively higher log quality associated with vertical, exploratory wells such as well A, which are potentially less affected by anisotropic effects than deviated "side-track" wells.

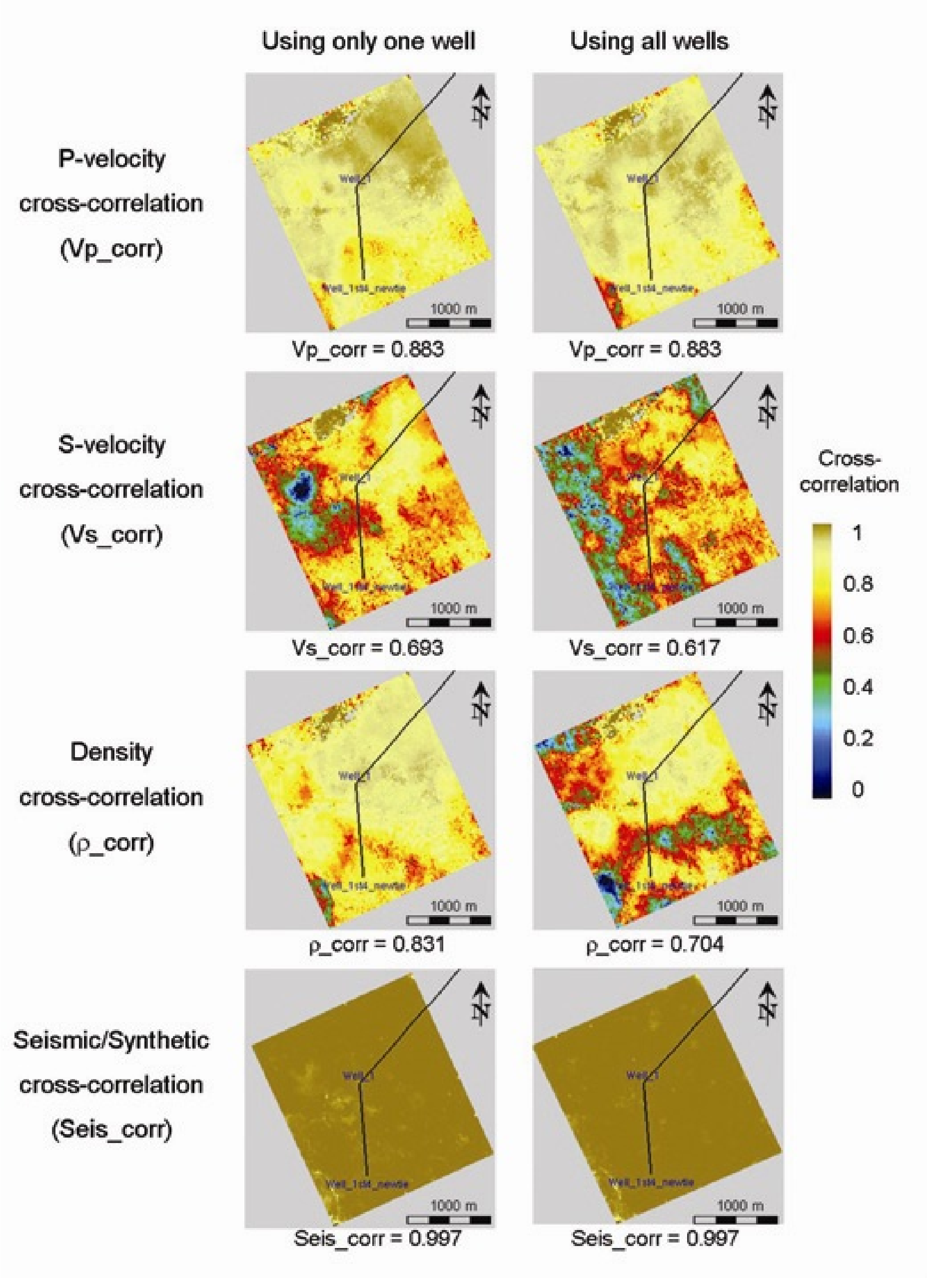

Figure 4.5: Sensitivity analysis of 3D PDFs. Maps represent the average cross-correlation between the original and inverted volumes in the model space (Vp, Vs, ρ) and data space (seismic/synthetic). Two case scenarios are considered: (1) when only one well is used to generate the 3D PDFs (left), and (2) if all wells are included (right).

4.3.2 Sensitivity analysis of inversion parameters

Inversion parameters such as lithotype fraction and variogram lateral range were analyzed in order to determine their effect on the inverted distributions of elastic properties.

The sensitivity analysis of lithotype fraction consisted of two opposite case scenarios: (1) sand = 20%, shale = 80%; and (2) sand = 80%, shale = 20%. Cross-correlation maps, similar to those described in the previous sensitivity analysis, were produced from the input and inverted models of elastic properties. As shown in Table 4.1, the results of this exercise demonstrate that an erroneous assumption of lithology proportions (case 2) can lead to a detriment of the inversion results, which is evidenced by a cross-correlation decrease of all the elastic properties (model space), and the seismic/synthetic cross-correlation (data space).

Similarly, the effect of the variogram lateral range was analyzed by considering four different values: (1) 500 m; (2) 1000 m; (3) 1500 m; and (4) 2000 m. We used the same mapping approach previously described and compared the average cross-correlation of elastic properties obtained from all the variogram lateral range values considered (Table 4.1). The results show that the effect of variogram lateral range on the inversion results is relatively low (less than 2% change) compared to that of lithotype range (up to 10% change).

Table 4.1: Summary of the sensitivity analysis on factors controlling joint stochastic inversion of synthetic PAS and well-logs. Optimum factors (associated with the highest cross-correlation values) are highlighted in boldface.

Factor	Model Space (Original/Inverted Models Cross-correlation)			Data Space (Seismic / Synthetic Cross-correlation)
	P-velocity	S-velocity	Density	
3D PDFs				
Case 1: From 1 well	**0.883**	**0.693**	**0.831**	**0.997**
Case 2: From all wells	0.883	0.617	0.704	0.997
Lithotype Fraction				
Case 1: **Sand = 20%; Shale = 80%**	**0.883**	**0.693**	**0.831**	**0.997**
Case 2: Sand = 20%; Shale = 80%	0.837	0.596	0.756	0.994
Variogram Lateral Range				
Case 1: 500 m	0.878	0.661	0.825	0.996
Case 2: 1000 m	**0.881**	**0.688**	**0.828**	**0.996**
Case 3: 1500 m	0.866	0.661	0.815	0.996
Case 4: 2000 m	0.868	0.693	0.813	0.996
Realizations				
Case 1: Seed Value = 1	**0.883**	**0.693**	**0.831**	**0.997**
Case 2: Seed Value = 2	0.866	0.659	0.817	0.996

4.3.3 Sensitivity analysis of realizations

The novel MCMC inversion algorithm implemented in this chapter can produce multiple equi-probable distributions of elastic properties and lithotypes that simultaneously honor all input data. A new but equally probable solution can be generated by simply selecting a different "seed value" in the users script of input parameters.

In order to quantify the variability of the inversion results due to the intrinsic non-uniqueness of the inversion problem, we ran two inversion tests using different seed values. Subsequently, we applied the cross-correlation mapping technique previously described, and the results of both the model and data spaces were included in Table 4.1. This exercise indicates that equally probable realizations can have about 2-4% variability in their accuracy in the model space, and lower than 0.1% in the data space.

4.4 FIELD DATA EXAMPLE

Seismic amplitude measurements considered in this field data example were the same described in previous chapters. In this study, we assume that the migrated and NMO-corrected CMP gathers are devoid of multiple and transmission effects, are not affected by elastic anisotropy, and can be accurately described as the superposition of two-layer responses of a stack of horizontal layers. Further, we consider only isotropic PP reflectivity events in the analysis of pre-stack seismic amplitude variations. We used a ray-tracing algorithm to transform the pre-stack seismic amplitude data from the offset domain to the incidence-angle domain, and generated four partial-angle stacks using the NMO-corrected and migrated offset-gathers and the migration-velocity field. The angle range available from the seismic amplitude data was 6 to 46 degrees; each partial-angle stack was generated using a 10-degree constant range. Final PAS included the following angle ranges: [6-16], [16-26], [26-36], and [36-46].

Since well log data are a crucial component of the proposed inversion methodology, they must be accurately processed and corrected for environmental/borehole effects and invasion. Accordingly, their reliability was corroborated analyzing quality-control curves such as caliper, tension, and delta-rho logs. Furthermore, synthetic S-wave sonic logs were computed from P-wave sonic logs using empirical Vp-Vs relations as those defined by Greenberg and Castagna (1992), and finally compared against measured logs for additional quality control.

4.4.1 AVA simultaneous stochastic inversion

Four partial-angle stacks were simultaneously inverted with well logs using the previously described AVA stochastic inversion algorithm. The pre-stack stochastic inversion algorithm was implemented with a stratigraphic/structural framework that enforced a 1-ms micro-layering as the sampling rate. Input data consisted of: (1) four partial-angle stacks and angle-dependent wavelets for the previously described angle ranges; (2) lithotype, Vp, Vs, and density logs, and (3) well-log generated geostatistical information in the form of variograms and histograms of properties (Figure 4.6a). The results of the AVA stochastic inversion, which consist of high-vertical-resolution (1 ms) 3D distributions of elastic properties (Vp, Vs, and density), and lithotypes (sand/shale), are shown in Figure 4.6(b).

Quality control of inversion results was conducted through blind well tests to validate the simulations of elastic property at known well locations. Figure 4.7 is a comparison between the inverted pseudo-logs of P-velocity. S-velocity, and density, extracted at the well location A, and the measured well-log curves at the same location. The thick blue curves represent the mean of 10 realizations, and the thin blue curves are the associated confidence intervals (+/- 1 standard deviation from the mean value). These curves closely match the actual well-log measurements (red curves) within the inversion frequency range, evidencing that the stochastic inversion of pre-stack seismic data accurately reconstructed elastic properties at well locations.

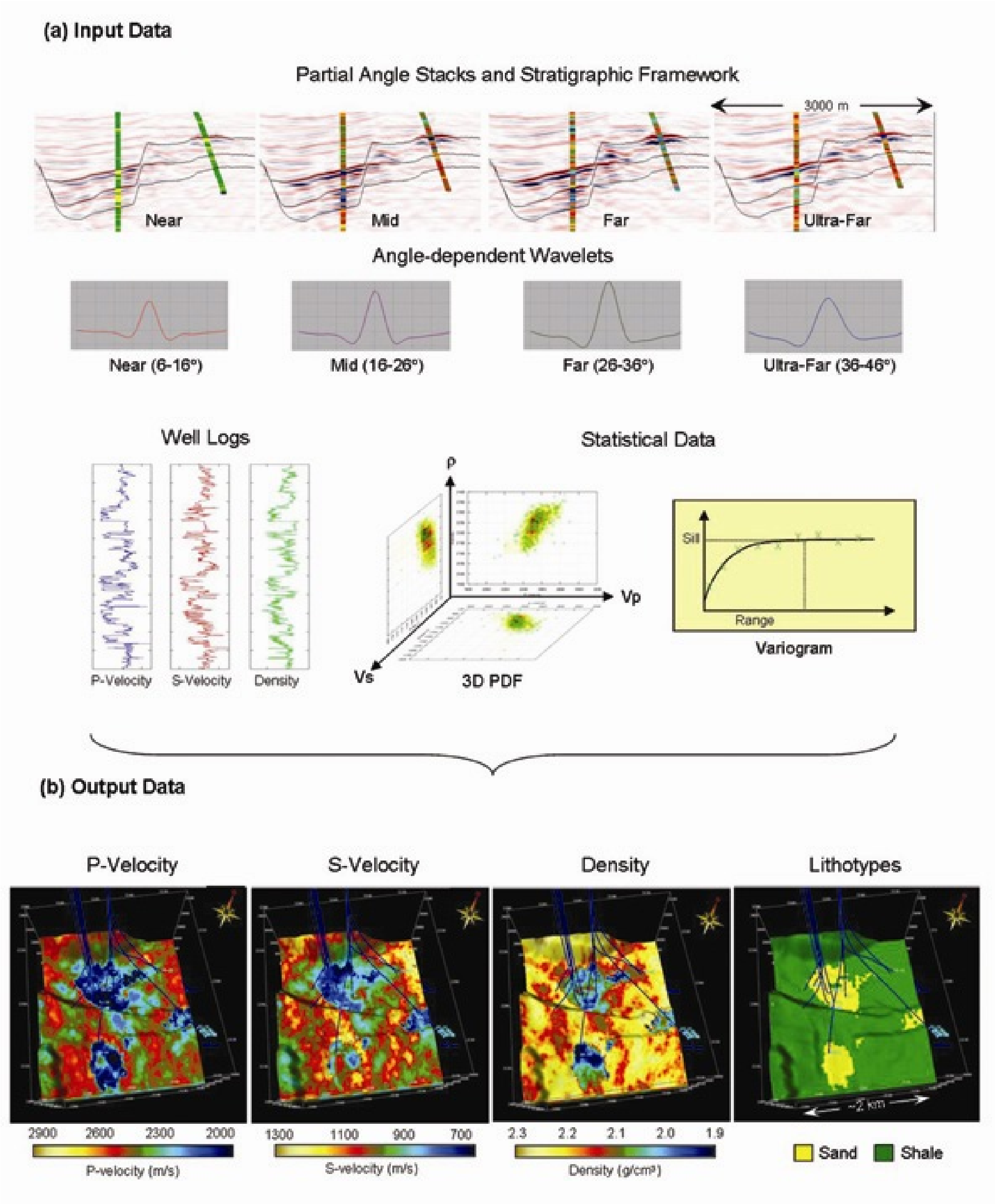

Figure 4.6: Schematic representation of the input and output data involved in pre-stack stochastic inversion: (a) Input data: partial-angle stacks, angle-dependent wavelets, well-logs of Vp, Vs, density, and lithotypes; and 3D PDF's of elastic properties and variograms (lithotype- and layer-dependents); (c) Outputs: volumes of Vp, Vs, density, and lithotypes.

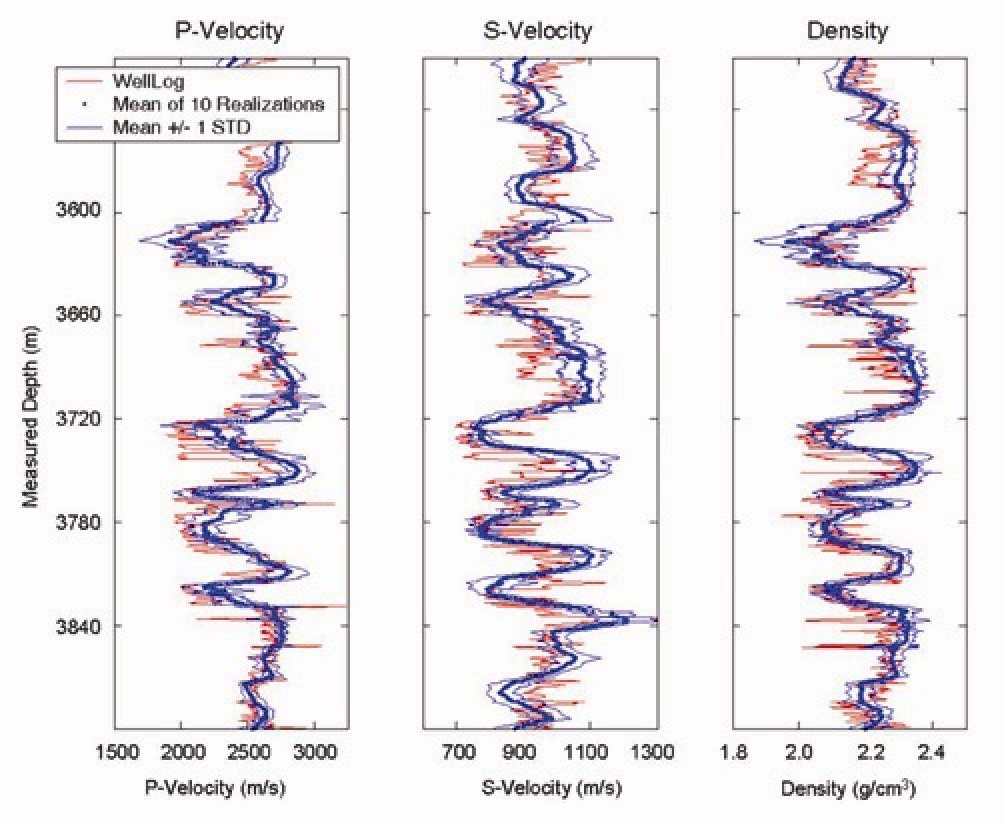

Figure 4.7: Quality control: blind well test performed to validate the elastic results at a known well location. The thick blue curves represent the mean of 10 realizations, and the thin blue curves are the associated confidence intervals (+/- 1 standard deviation from the mean value). These curves closely match the actual well-log measurements (red curves) within the inversion frequency range, evidencing that the stochastic inversion of pre-stack seismic data accurately reconstructed elastic properties at well locations.

4.4.2 Sensitivity analysis of inversion parameters

Another sensitivity analysis of inversion parameters was performed using post-stack seismic amplitude data. Parameters analyzed included: (1) variogram type, (2) variogram vertical/lateral range, (3) lithotype fraction, (4) noise level, (5) wavelet scaling, and (6) seed value for different realizations. This study indicated that reasonable variation of the assumed inversion parameters slightly affected the results. We found that selection of optimal inversion parameters can be achieved by using criteria such as the highest real/synthetic seismic cross-correlations (low residuals) as well as property distributions that follow the shape of seismic amplitude anomalies.

Figure 4.8 illustrates the results of the sensitivity analysis of variogram type. These figures evidence how Gaussian variograms produce smoother results than exponential variograms, which in turn generate more reliable results in the data space: lower residuals and higher seismic cross-correlation. Table 4.2 summarizes the different parameters considered for these sensitivity analysis and the optimum values selected.

The effect of the main inversion parameters such as lithotype fraction and variogram lateral range was further analyzed using pre-stack-seismic amplitude data. Figure 4.9 illustrates the effect of user-defined lithotype proportions on the simulated lithology distributions. Two case scenarios were considered: (1) using a lithotype fraction of 5% sand and 95% shale; and (2) using a lithotype proportion of 25% sand and 75% shale.

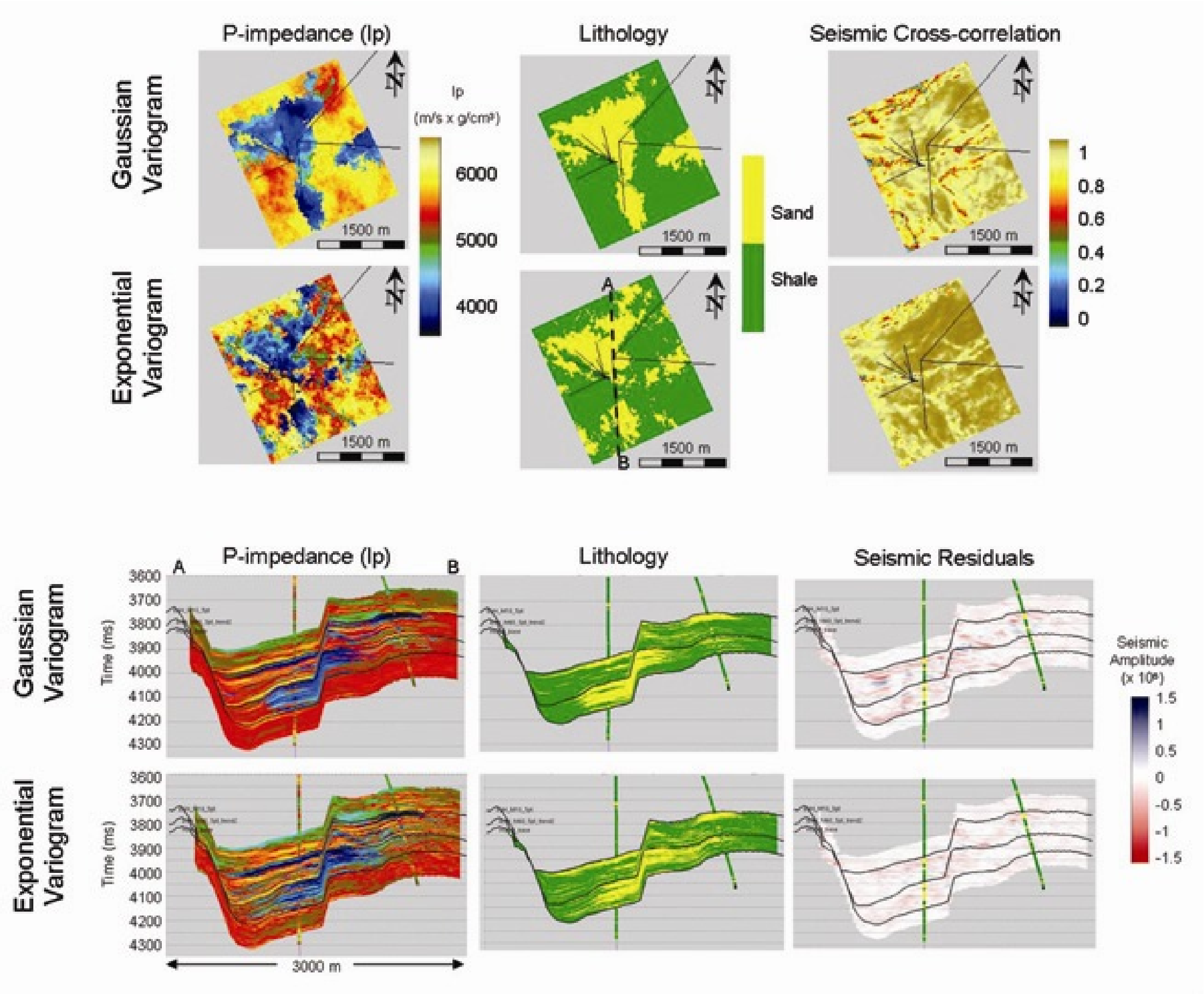

Figure 4.8: Results of the sensitivity analysis variogram type. Maps correspond to the M-10 reservoir sand, and black lines represent well trajectories. From left to right: (1) Ip, (2) lithotypes, and (3) cross-correlation between real and synthetic seismic amplitude data. Maps above correspond to Gaussian variograms and maps below to exponential variograms. All sections correspond to the arbitrary line A-B that links well A (vertical) and well B (deviated). From left to right: (1) Ip, (2) lithotypes, and (3) seismic residuals. As expected, Gaussian results are smoother than exponential outputs, which in turn have higher seismic cross-correlation.

Table 4.2: Summary of the sensitivity analysis of inversion parameters controlling joint stochastic inversion of measured post-stack seismic amplitude data and well-logs. Optimum values (associated with the highest cross-correlation values) are highlighted in boldface.

INVERSION PARAMETER	VALUES ANALYZED
Variogram Type	Gaussian **Exponential**
Variogram Lateral Range (m)	250 500 **1000** 1500 2000
Variogram Vertical Range (ms)	60 100 **150** 200
Seismic Noise Level (dB)	-1 -5 **-10** -15 -20
Wavelet Scaling	0.8 0.9 **1.0** 1.1 1.2
Lithology Fraction (% Sand / %Shale)	10 / 90 15 / 85 **20 / 80** 25 / 75 50 / 50
Realizations (Seed Value)	1 2 3 4 5

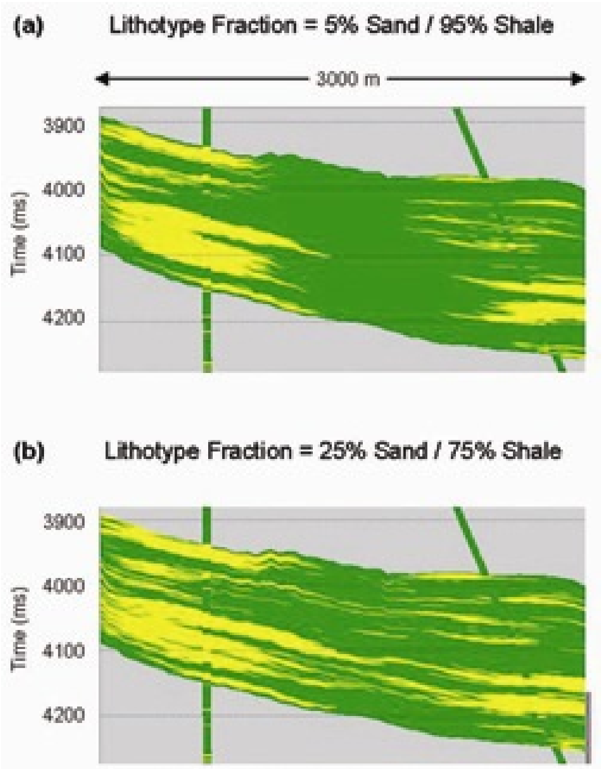

Figure 4.9: Sensitivity analysis to the inversion parameter "Lithotype Fraction": (a) Lithotype cross-section inverted for a 5% Sand / 95% Shale distribution, (b) Lithotype cross-section inverted for a 25% Sand / 75% Shale distribution. Inversion results are clearly affected by the choice of lithotype fraction parameter; however, the lateral extent and geometry of the thickest sand bodies remain almost constant; mostly thin sands are added by the inversion algorithm when increasing the assumed sand/shale ratio.

Inversion results are clearly affected by the choice of lithotype fraction parameter; however, the lateral extent and geometry of the thickest sand bodies remain almost constant; mostly thin sands are added by the inversion algorithm when increasing the assumed sand/shale ratio. Similarly, Figure 4.10 illustrates the effect of user-input variogram lateral range on the simulated lithology distributions. Two case scenarios were considered: (1) using a variogram lateral range of 500 m; and (2) using a variogram lateral range of 1000 m. Inversion results are clearly affected by the variogram lateral range; however, the lateral extent and geometry of the thickest sand bodies remain marginally affected by the choice of variogram.

4.4.3 Sensitivity analysis of seismic amplitude data type

Additionally, well blind tests were performed to compare lithotype simulations generated using post-stack data (only dependent on P-Impedance) and those obtained from pre-stack data (jointly conditioned by P-Velocity, S-Velocity, and density). Figure 4.11 shows that lithotype realizations generated using either post- or pre-stack seismic data are very similar when all the available well log information is included as input; however, well blind tests show that lithotype distributions at well locations are more accurately reconstructed with pre-stack inversion. We also found that the lateral extent of the sands for the case of pre-stack results is less affected by the exclusion of well log data in the input than for the case of post-stack inversion results. In addition, the results of the sensitivity analysis and blind tests evidence that the thickest sand units (thickness above the seismic resolution) are better reconstructed and are less affected by changes of inversion parameters than thin sand units.

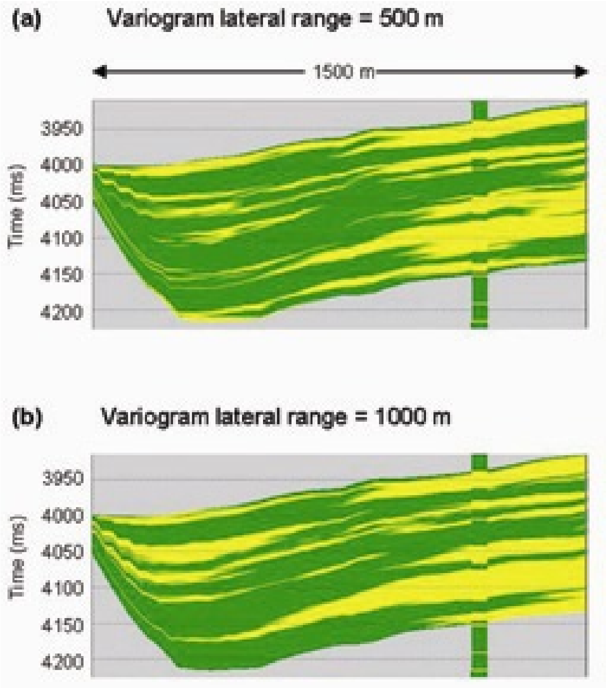

Figure 4.10: Sensitivity analysis to the inversion parameter "Variogram lateral range": (a) Lithotype cross-section inverted with a variogram lateral range of 500 m., (b) Lithotype cross-section inverted with a variogram lateral range of 1000 m. Inversion results are clearly affected by the variogram lateral range; however, the lateral extent and geometry of the thickest sand bodies remain marginally affected by the choice of variogram.

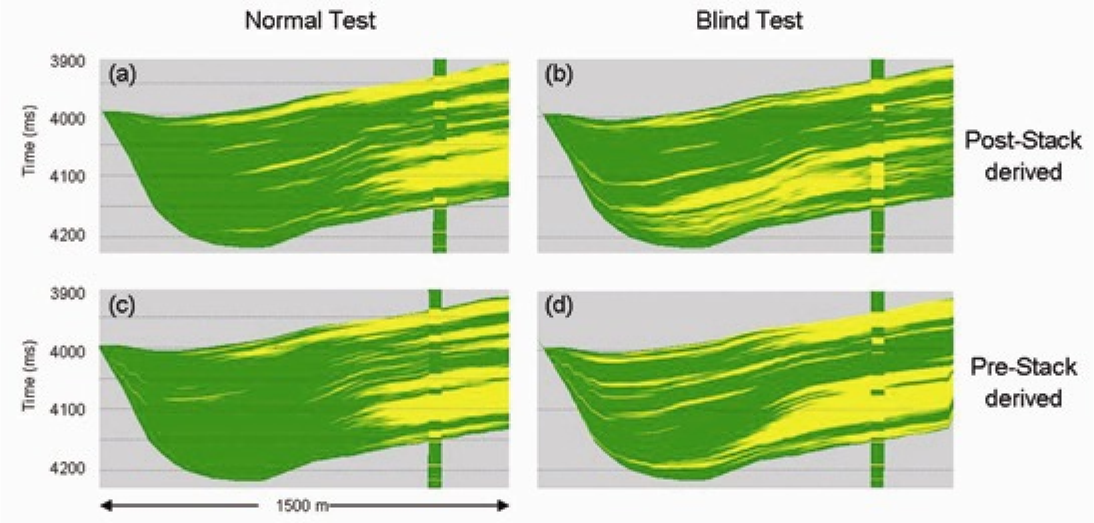

Figure 4.11: Lithotype distributions inverted from post- (a, b) and pre-stack seismic data (c and d). Normal tests (a, c) were produced including the vertical well as input data for the inversion; whereas blind tests (b, d) excluded the well from the input data. Well blind tests show that lithotype distributions along the well track are better reconstructed from pre-stack seismic data. Also, the lateral extent of the sands (normal vs. blind test) is more consistent for the case of pre-stack seismic data.

4.4.4 Co-simulation of petrophysical properties

Conventional approaches for generating 3D distributions of petrophysical properties from post-stack seismic inversion consist of co-simulation of one petrophysical property (i.e., porosity) from the inverted acoustic property (i.e., P-impedance) by enforcing a geostatistical correlation between them. However, pre-stack stochastic inversion results consist of three elastic properties (Vp, Vs, and density), which are, in turn, dependent on medium physical properties such as lithology, porosity, and pore fluid content (Castagna and Backus, 1993). This provides additional degrees of freedom to enforce several statistical correlations between more than one elastic and petrophysical property.

When cross-plotting three properties (such as Vp, Vs, and porosity), the clusters associated with each lithofacies appear as three-dimensional clouds, comprising samples from a 3D joint probability distribution. Projection of this distribution onto the sides of the diagram yields the corresponding 2D joint distributions (for Vp-Vs, Vp-porosity, and Vs-porosity). However, information is lost in the projection, and it is not necessarily possible to reconstruct the 3D distribution even from the full set of 2D distributions. In other words, there are correlations between the three properties that are not captured in the correlations between the three pairs, just as correlations between two properties are not captured by their 1D histograms.

Our approach consists of performing reservoir characterization on the basis of assumptions made on the multidimensional joint distribution of all the properties involved (elastic and petrophysical), rather than about their individual histograms or 2-component cross-plots. The more precisely we can represent the true shape of the joint probability distribution, the more accurate and less uncertain our predictions will be. For example, we may be able to make a better porosity prediction for a reservoir if we take into account both Vp and Vs, than if we derive porosity from either velocity on its own. And we will be able to image the sands better if we can rule out unlikely combinations of sand Vp, Vs, and ϕ, than if we look separately at Vp vs. Vs and Vs vs. ϕ.

The 3D spatial distributions of the main petrophysical properties (porosity, permeability, and water saturation) were generated via co-simulation of the AVA stochastic inversion results (Vp, Vs, and density) using the same multivariate statistical approach previously described. The methodology consisted of generating 1D sample histograms from well logs for each elastic and petrophysical property and then combining the information into layer- and lithotype-dependent multidimensional joint distributions. The aim of this methodology is to capture all the relationships and correlations among the six properties (Vp, Vs, density, porosity, permeability, and water saturation). Figure 4.12 is an example of the multidimensional (3D) joint probability distributions of elastic and petrophysical properties generated from well-log sampled histograms and used for pre-stack stochastic inversion. The same approach is used for petrophysical co-simulation by integrating 3 elastic and 3 petrophysical properties.

Figure 4.13 shows the spatial distribution of co-simulated petrophysical properties (porosity, permeability, and water saturation) obtained with the latter procedure. Since the statistical information is lithotype-dependent and the co-simulation focused only on sands, the resulting petrophysical distributions are constrained by the previously simulated lithologic (sand) models. Accordingly, the lateral extent of the sands is not affected by the petrophysical co-simulation.

Finally, blind well tests were performed to validate the petrophysical results at known well locations. These tests evidenced that the simultaneous use of the three elastic properties (Vp, Vs, and density) for co-simulation of petrophysical properties such as porosity is a reliable approach (Figure 4.14).

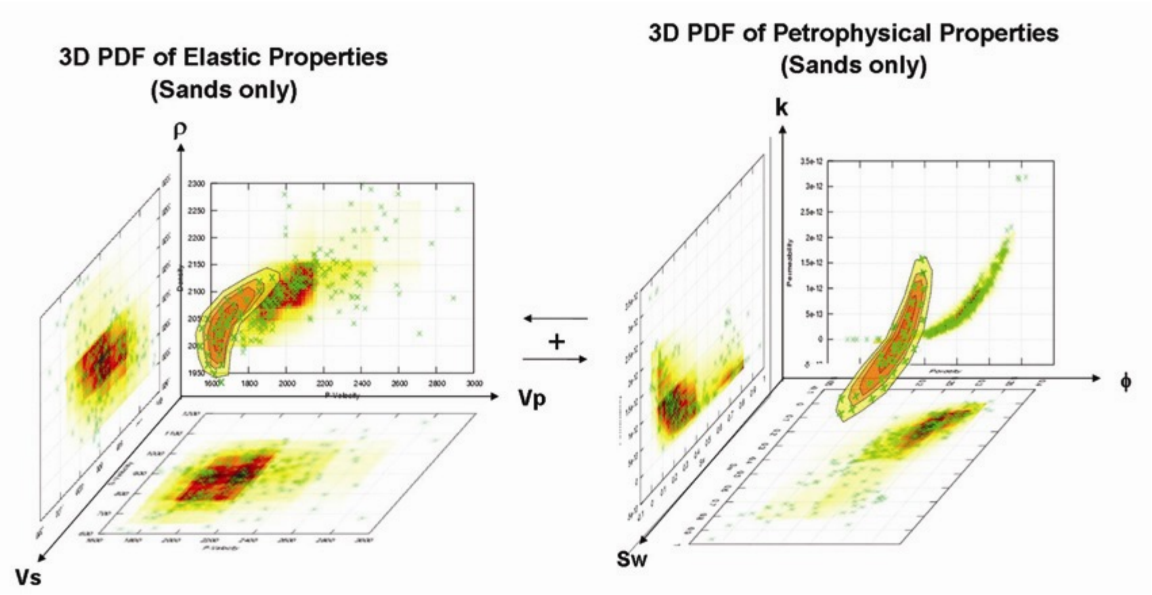

Figure 4.12: Schematic representation of lithotype-dependent 3D PDFs of elastic and petrophysical properties, generated exclusively for “sands”. The co-simulation of petrophysical properties is based on a similar approach that integrates all six properties into a non-graphical but numerically applicable 6D PDF.

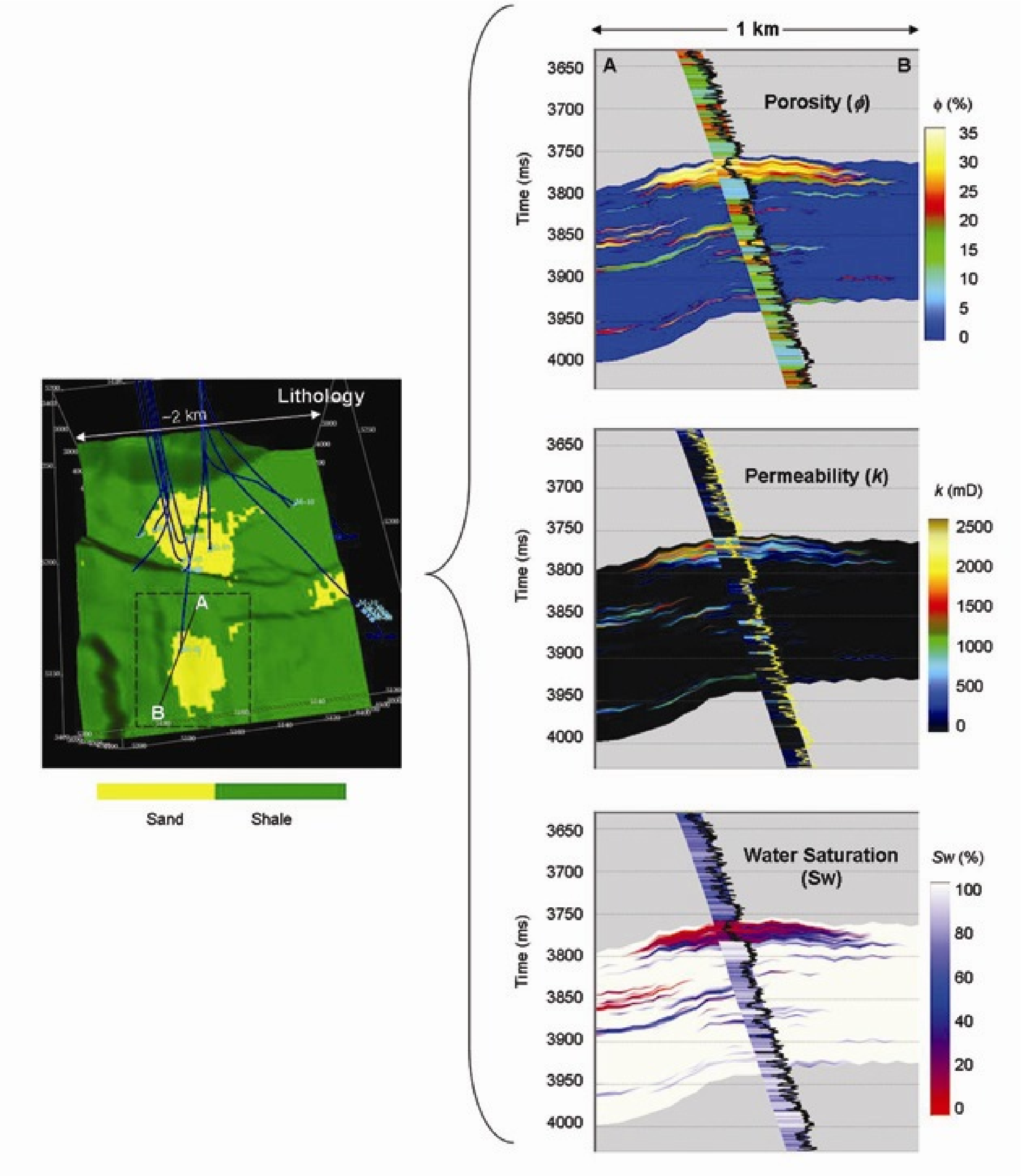

Figure 4.13: Cross-sections of co-simulated petrophysical properties (ϕ, k, and Sw) for the uppermost M-10 reservoir. Three-dimensional view represents one internal lithological microlayer associated with the M-10 reservoir. The spatial coverage is approximately 4 km^2.

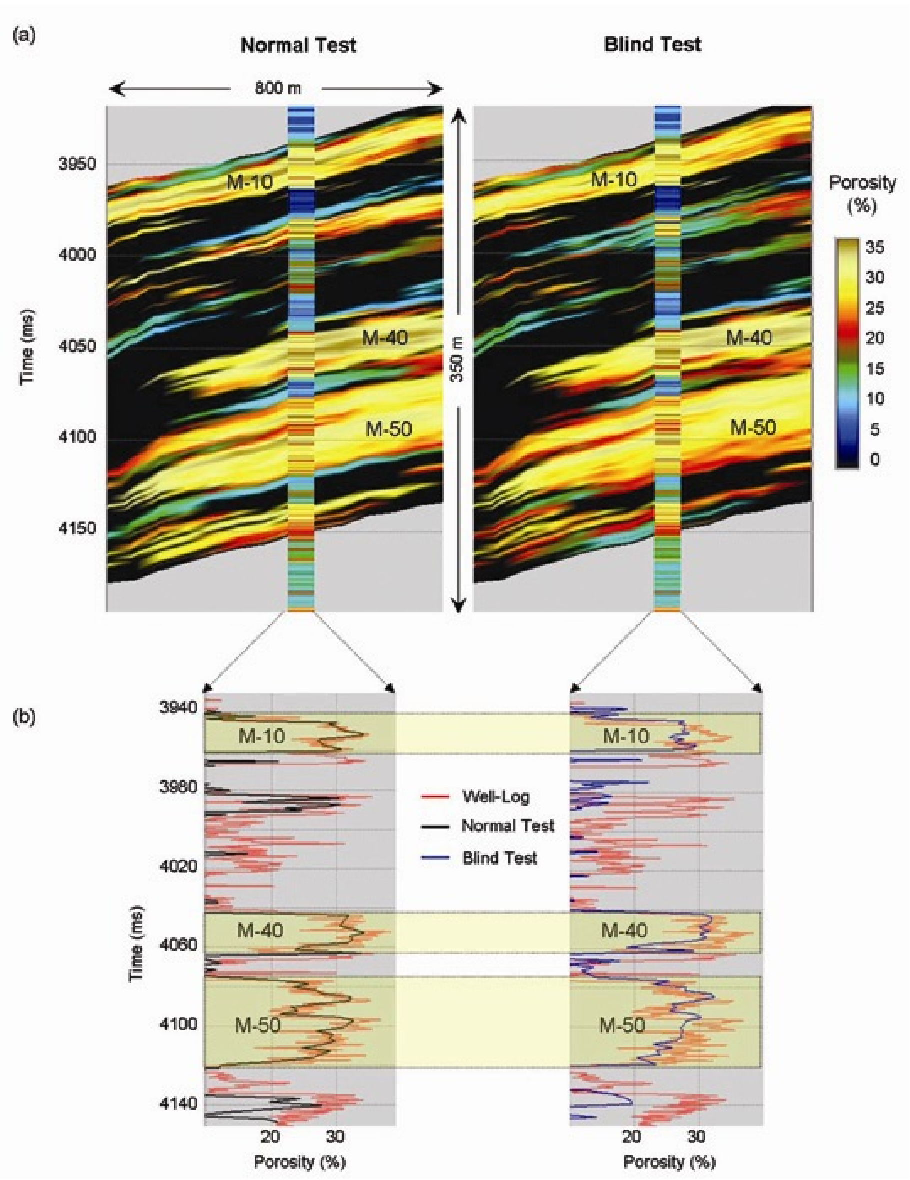

Figure 4.14: Porosity co-simulation tests in section view (a) and pseudo-log view (b). For normal test the well has been included as input for the co-simulation; whereas in blind test the well porosity log is not used for co-simulation. Thick and high-porosity sands are better co-simulated. Notice that the lateral extent of the sands is not affected by the petrophysical co-simulation.

4.4.5 Sensitivity analysis of elastic/petrophysical property correlations

In theory, the more precisely we can represent the true shape of the joint probability distribution, the more accurate and less uncertain our predictions will be. For example, we may be able to make a better porosity (ϕ) prediction for a reservoir if we take into account both Vp and Vs, than if we derive porosity from either velocity on its own. And we will be able to image the sands better if we can rule out unlikely combinations of sand Vp, Vs, and ϕ, than if we look separately at Vp vs. Vs and Vs vs. ϕ.

In order to test this hypothesis, porosity co-simulations using 2D, and 4D correlations were compared to assess the effect of including relationships between Vp, Vs, and density on the porosity predictions. Two-dimensional joint distributions consist of single relationships between Vp and Porosity, Vs and Porosity, and Density and Porosity, whereas 4D joint distributions consist of simultaneous relationships among Vp, Vs, density, and porosity (Figure 4.15). As illustrated in this figure, the size and spatial distribution of geobodies associated with porosity values greater than 25% clearly change when using PDFs of different dimensionalities. The inclusion of Vs and ρ information associated with 4D PDFs resulted in larger porosity geobodies than those generated from 1D PDFs. Additionally, Figure 4.16 illustrates the results of a well blind test associated with porosity co-simulations from different combinations of elastic parameters. The most accurate porosity predictions were obtained when using 4D PDFs. The inclusion of both Vs and ρ has clearly improved the estimated porosity log for the main reservoir sands.

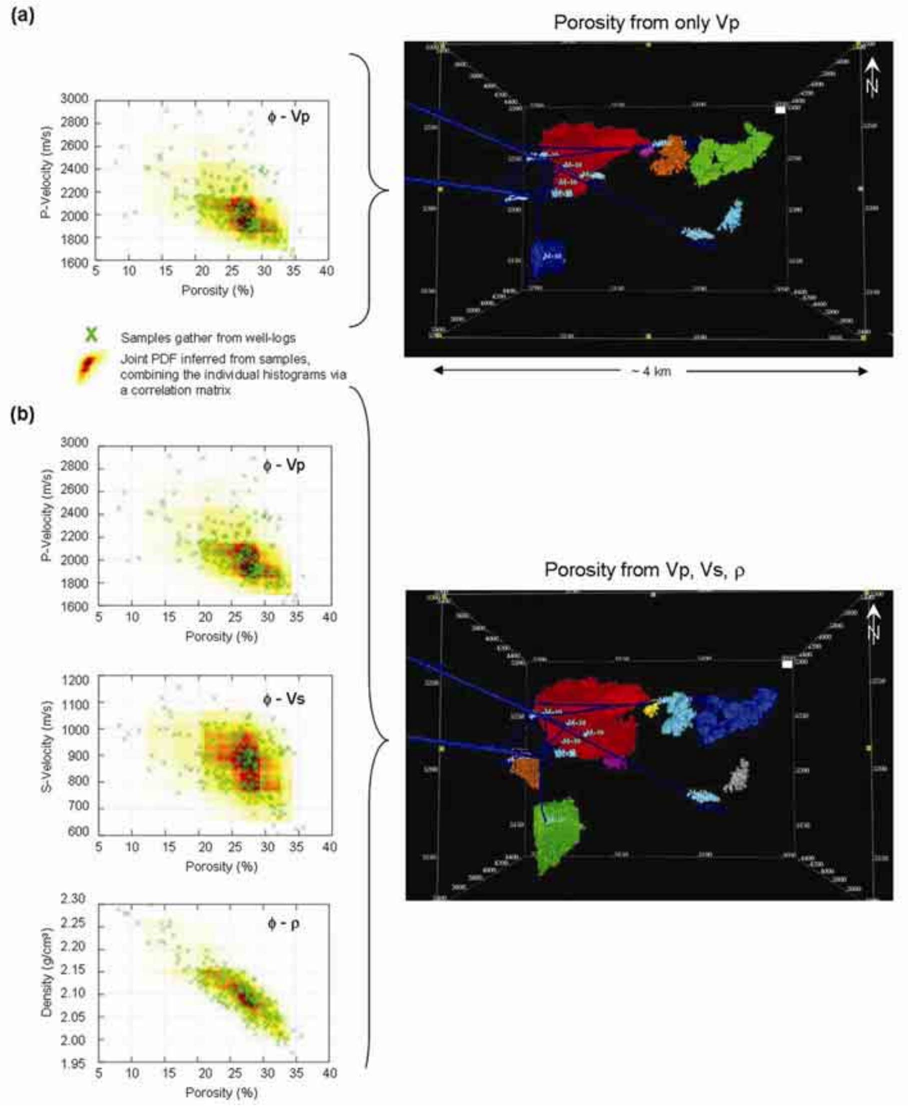

Figure 4.15: Results of the co-simulation tests using different combinations of elastic properties: (a) Porosity from only Vp, and (b) Porosity from Vp, Vs, and density. The crossplots to the left represent the joint PDF's used for co-simulation (Porosity-Vp, Porosity-Vs, and Porosity-Density, respectively). The 3D views to the right show the extracted M-10 reservoir geobodies associated with porosity values higher than 25%. Different colors identify individual non-connected geobodies, and blue lines represent well trajectories. The spatial coverage is approximately 4 km^2.

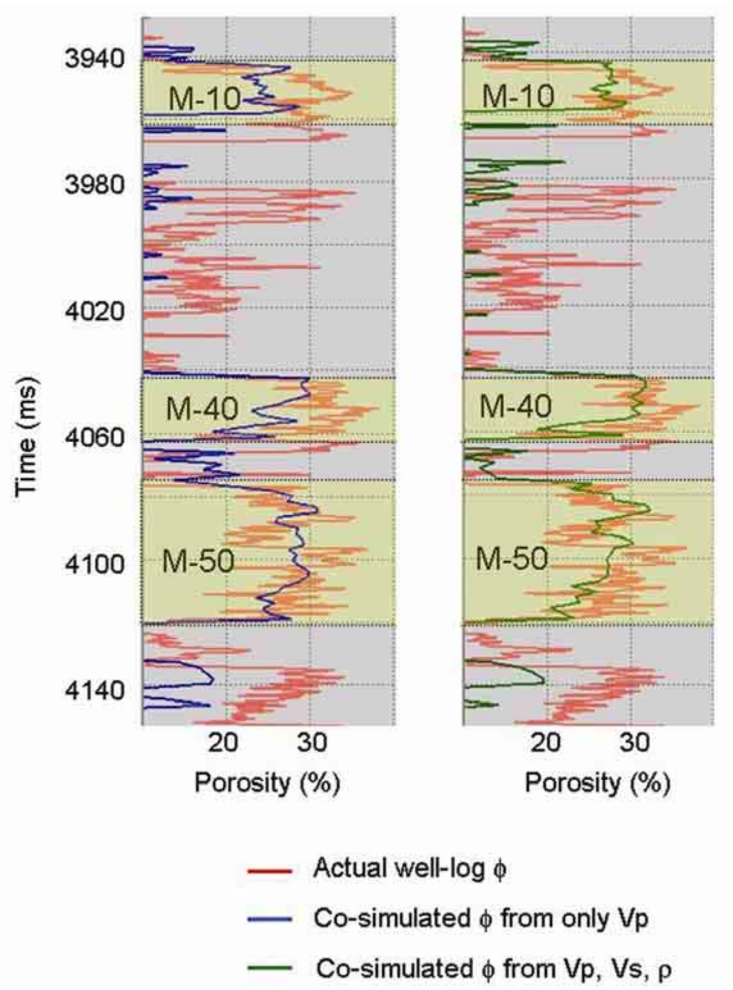

Figure 4.16: Well blind test associated with porosity co-simulations from different combinations of elastic parameters as shown in Figure 4.15: (1) Porosity simulation from only Vp (blue curve); (2) porosity simulation from Vp, Vs, and ρ (density, green curve). The red curve identifies the actual porosity log computed at the well location. The inclusion of both Vs and ρ has clearly improved the estimated porosity log for the main reservoir sands.

4.5 UNCERTAINTY ASSESSMENT

Uncertainty assessment of the petrophysical co-simulation was conducted by calculating the standard deviation of 30 porosity realizations (Figure 4.17). Results from this exercise confirm that the spatial range of uncertainty is consistent with the estimated lateral extent of sand units. The uncertainty monotonically increases away from well locations.

We remark that the petrophysical co-simulations are spatially limited by the sand boundaries defined in the initial lithotype volume. The spatial range of uncertainty associated with petrophysical co-simulations is primarily governed by the underlying non-uniqueness of the masking lithotype simulations. Specifically, different lithotype realizations are obtained from the inversion by only changing an arbitrary seed value. Subsequent petrophysical co-simulations are then affected by the uncertainty of the guiding spatial distributions of lithotype.

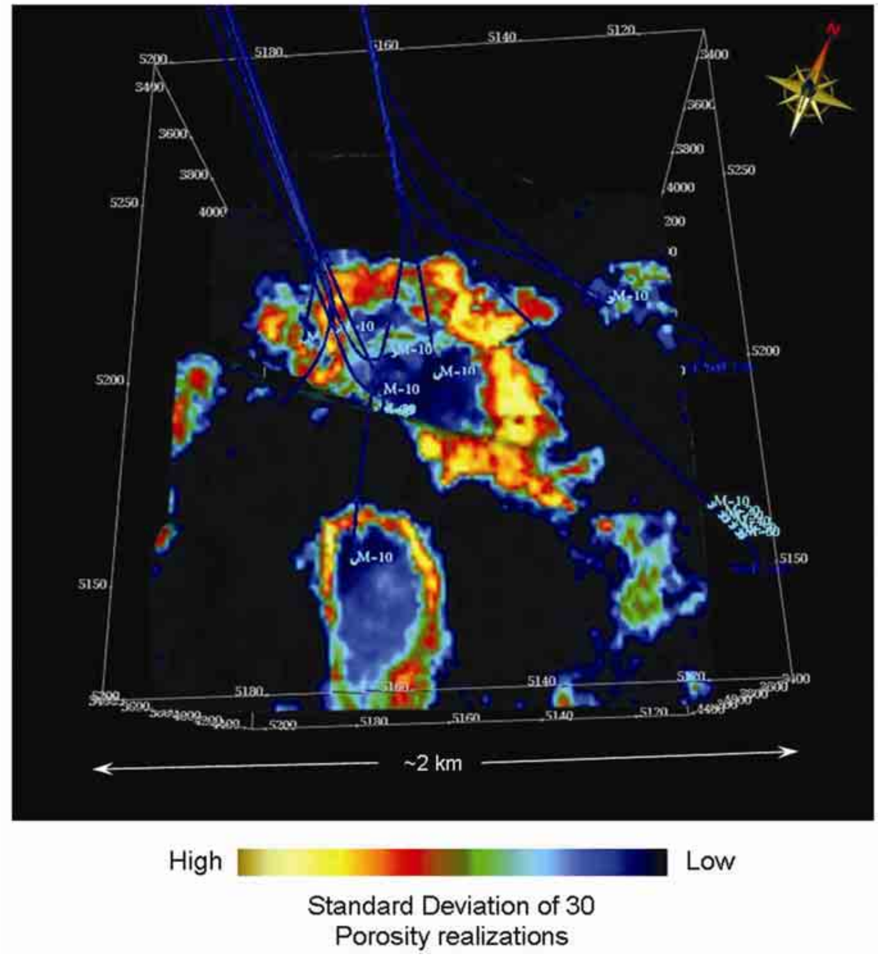

Figure 4.17: Uncertainty assessment of petrophysical co-simulations using the standard deviation of 30 porosity realizations. Blue intervals correspond to low uncertainty areas (low standard-deviation values). Three-dimensional view represents one internal microlayer associated with the M-10 reservoir; blue lines represent well trajectories. The spatial coverage is approximately 4 km^2.

4.6 SUMMARY

This chapter describes the successful implementation of a new algorithm for the joint stochastic inversion of well logs and multiple angle stacks of migrated pre-stack seismic amplitude data. The inversion algorithm is based on a Bayesian statistical search criterion implemented with fast Markov-Chain Monte Carlo updates. It implements *a-priori* measures of spatial correlation of the unknown distributions of elastic parameters over a specified structural and stratigraphic embedding. Results consist of spatial distributions of elastic properties with a vertical resolution intermediate between that of seismic amplitude data and well logs. In addition, the algorithm provides quantitative estimates of non-uniqueness based on the statistical distribution of multiple spatial realizations derived from random initial models. It is also possible to estimate lithology and petrophysical properties such as porosity and water saturation by enforcing multi-dimensional statistical correlations between elastic and petrophysical properties sampled from well-log measurements.

We describe results of a sensitivity analysis on the main factors controlling the inversion algorithm using synthetic and recorded seismic amplitude data from deepwater reservoirs located in the central Gulf of Mexico. Sensitivity analyses of resolution and non-uniqueness along blind-well locations corroborate the reliable estimation of elastic and petrophysical properties. The estimated distributions of lithotypes and elastic properties are marginally influenced by both the choice of inversion parameters and the assumed measures of spatial correlation.

Chapter 5: Application of AVA Stochastic Inversion for High-Resolution Reservoir Characterization

5.1 INTRODUCTION

The main objective of this chapter is to apply the AVA stochastic inversion methodology previously descrived to the high-resolution reservoir characterization and petrophysical modeling of deepwater hydrocarbon reservoir from the central Gulf of Mexico. Tha basic idea is to assess the lateral continuity and spatial extent of M-series lithology and fluid units penetrated by wells using pre-stack seismic amplitude data.

As described in previous chapters, deterministic inversion techniques have been successfully used for reservoir delineation and lithology/fluid characterization in the study area. However, high-resolution stochastic 3D models of petrophysical properties and lithology remain necessary to build multiple equiprobable static reservoir models and to accurately assess the spatial continuity of fluid units away from wells.

In an effort to construct high-resolution stochastic reservoir models of elastic and petrophysical properties we resorted to amplitude information from 3D pre-stack seismic data and well logs. We first applied pre-stack stochastic inversion to generate volumes of elastic properties (Vp, Vs, density) and lithotypes, and then conducted petrophysical co-simulation based on the inverted elastic models and well-log-derived acoustic/petrophysical statistical correlations.

5.2 AVA SIMULTANEOUS STOCHASTIC INVERSION

Four partial-angle stacks were simultaneously inverted with well logs using the new AVA stochastic inversion algorithm previously described. The pre-stack stochastic inversion algorithm was implemented with a stratigraphic/structural framework that enforced a 1-ms micro-layering as the sampling rate.

Input data consisted of: (1) four partial angle-stacks and angle-dependent wavelets for the following angle ranges: [6-16], [16-26], [26-36], and [36-46]; (2) lithotype, Vp, Vs, and density logs, and (3) well-log generated geostatistical information in the form of variograms and histograms of properties (Figure 5.1a).

The results of the AVA stochastic inversion, which consist of high-vertical-resolution (1 ms) 3D distributions of elastic properties (Vp, Vs, and density), and lithotypes (sand/shale), are shown in Figures 5.1(b), 5.2, and 5.3.

Figure 5.2 shows three-dimensional views of the inverted elastic properties and lithotypes, corresponding to one internal microlayer associated to the uppermost sand reservoir (M-10). Additionally, cross-sections are included to illustrate the high-vertical-resolution of the results, as well as the lateral extent of the sand intervals, which are clearly identified by relatively low values of the three elastic properties. In addition, Figure 5.3 shows a graphical representation of the spatial distribution of lithotypes derived from pre-stack stochastic inversion. This 3D rendering particularly focuses on the filtered sand distribution (yellow geobodies) corresponding to the M-10 reservoir, and obtained from the mean of 6 realizations.

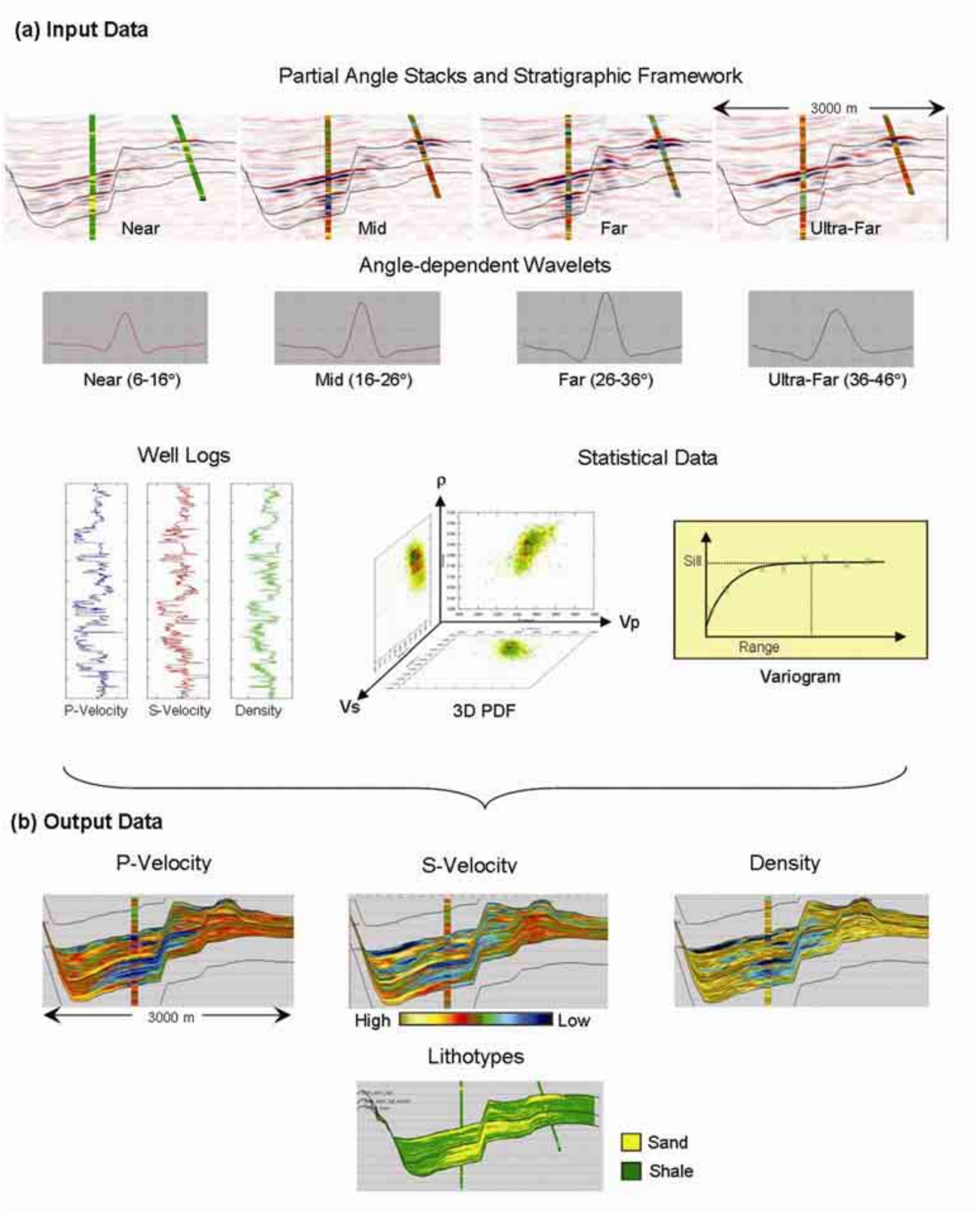

Figure 5.1: Schematic representation of the input and output data involved in pre-stack stochastic inversion: (a) Input data: partial-angle stacks, angle-dependent wavelets, well-logs of Vp, Vs, density, and lithotypes; and 3D PDF's of elastic properties and variograms (lithotype- and layer-dependents); (c) Outputs: volumes of Vp, Vs, density, and lithotypes.

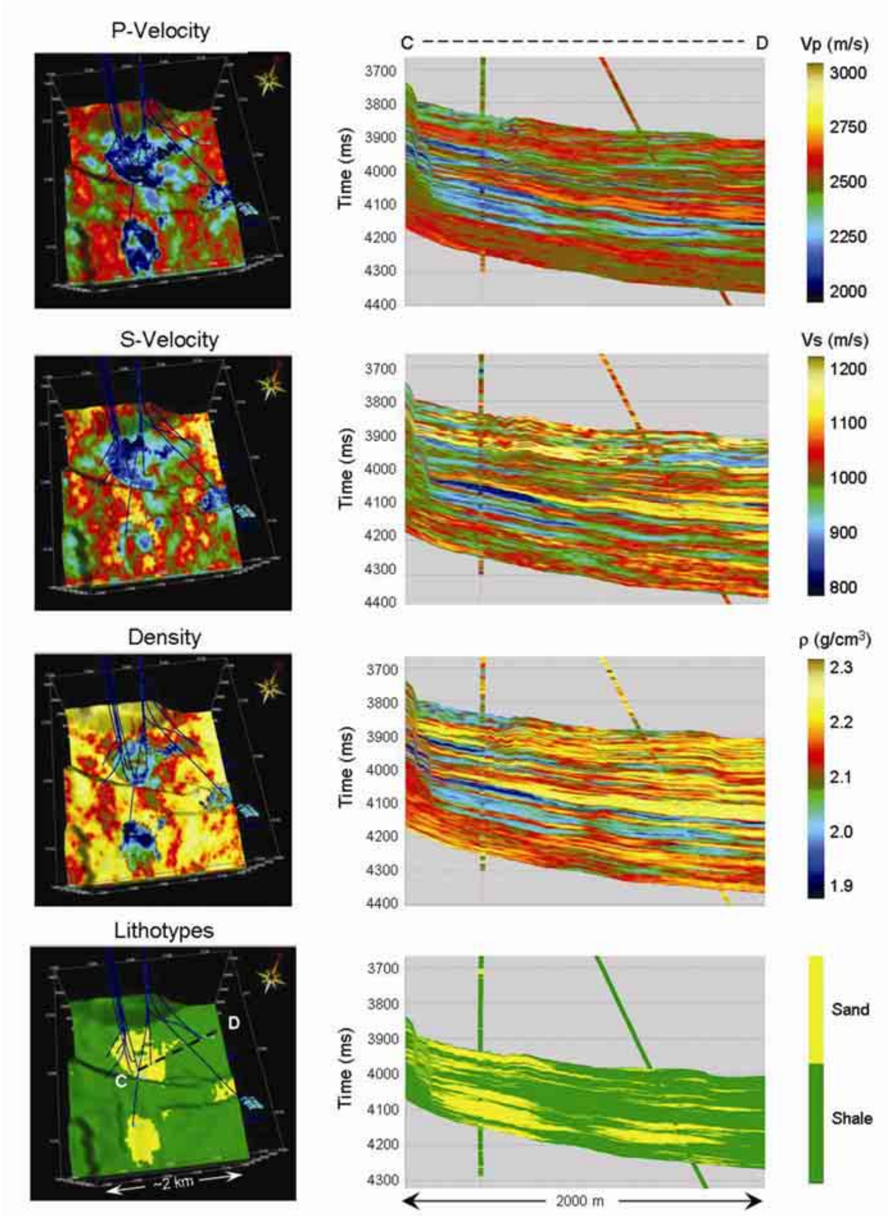

Figure 5.2: Elastic properties derived from pre-stack stochastic inversion: (a) P-Velocity, (b) S-Velocity, (c) Density, and (d) Lithotypes. Sand intervals and areas are identified by relatively low values of the three elastic properties. Cross-sections correspond to line C-D in the 3D view of litholotypes. Three-dimensional views correspond to only one internal microlayer associated to the uppermost sand reservoir (M-10). The spatial coverage is approximately 4 km^2.

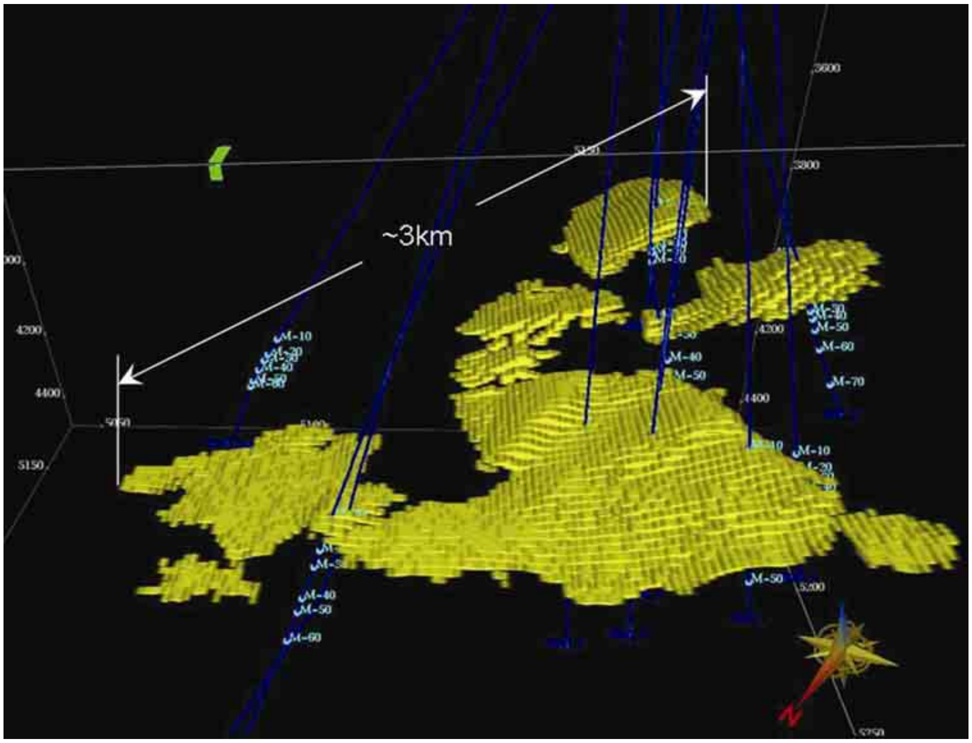

Figure 5.3: Spatial distributions of lithotypes derived from pre-stack stochastic inversion: 3D view of the filtered sand distribution (yellow geobodies) corresponding to the M-10 reservoir (mean of 6 realizations).

5.3 CO-SIMULATION OF PETROPHYSICAL PROPERTIES

The 3D spatial distributions of the main petrophysical properties (porosity, permeability, and water saturation) were generated via co-simulation of the AVA stochastic inversion results (Vp, Vs, and density) using a multivariate statistical approach. The methodology consisted of generating 1D sample histograms from well logs for each elastic and petrophysical property and then combining the information into layer- and lithotype-dependent multidimensional joint distributions. The aim of this methodology is to capture all the relationships and correlations between the six properties (Vp, Vs, density, porosity, permeability, and water saturation).

Figure 5.4 is an example of the multidimensional joint probability distributions of elastic properties generated from well-log sampled histograms and used for pre-stack stochastic inversion. The same approach is used for petrophysical co-simulation by integrating 3 elastic and 3 petrophysical properties. Figure 5.5 shows the spatial distribution of co-simulated petrophysical properties obtained with the latter procedure.

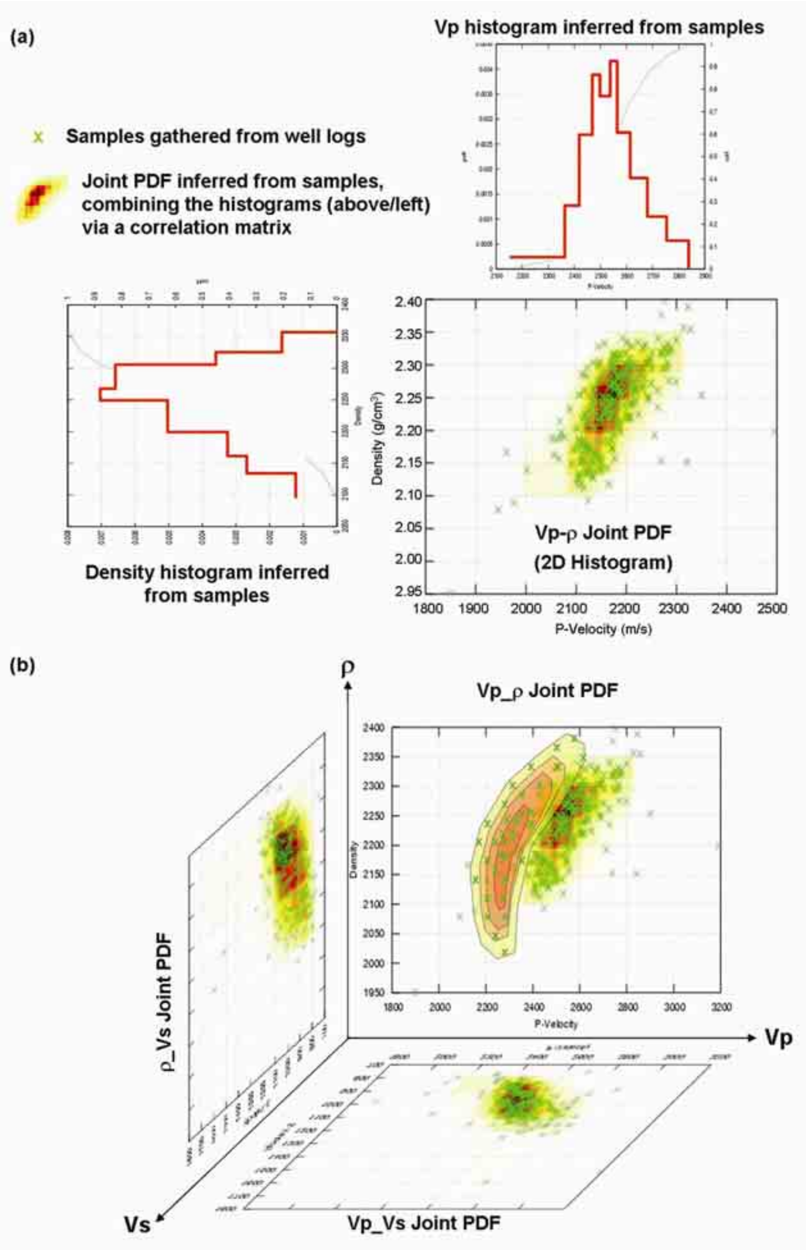

Figure 5.4: Example of lithotype-dependent multidimensional joint probability density functions (PDFs) constructed from well-log data: (a) Vp-Density Joint PDF (2D histogram) derived from 1D sample histograms ; (b) Schematic 3D Joint PDF of elastic properties: Vp, Vs, and Density (ρ).

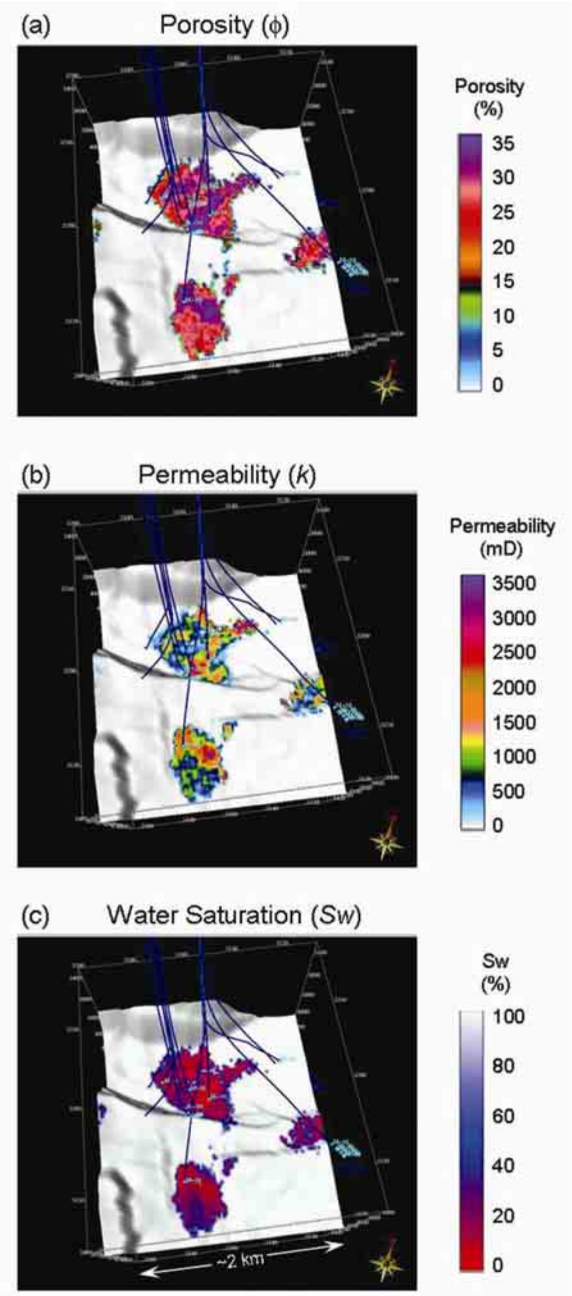

Figure 5.5: Co-simulated petrophysical properties for the M-10 reservoir: (a) porosity, (b) permeability, and (c) water saturation. Three-dimensional view of only one internal microlayer associated with the M-10 reservoir. The spatial coverage is approximately 4 km^2.

5.4 GEOLOGICAL INTERPRETATION OF STOCHASTIC INVERSION RESULTS

By integrating the channel/lobe depositional model introduced by Galloway and Hobday (1983) (Figure 5.6a) and the geomorphologic visualization of lithotype distributions achieved with pre-stack stochastic inversion results (Figure 5.6b), the M-series reservoir can be conclusively described as stacked turbidite lobes.

Furthermore, the co-simulated 3D models of petrophysical properties consistently reveal the existence of internal heterogeneities (small internal lobes) within the main lobes as predicted by the depositional model (Figure 5.6c).

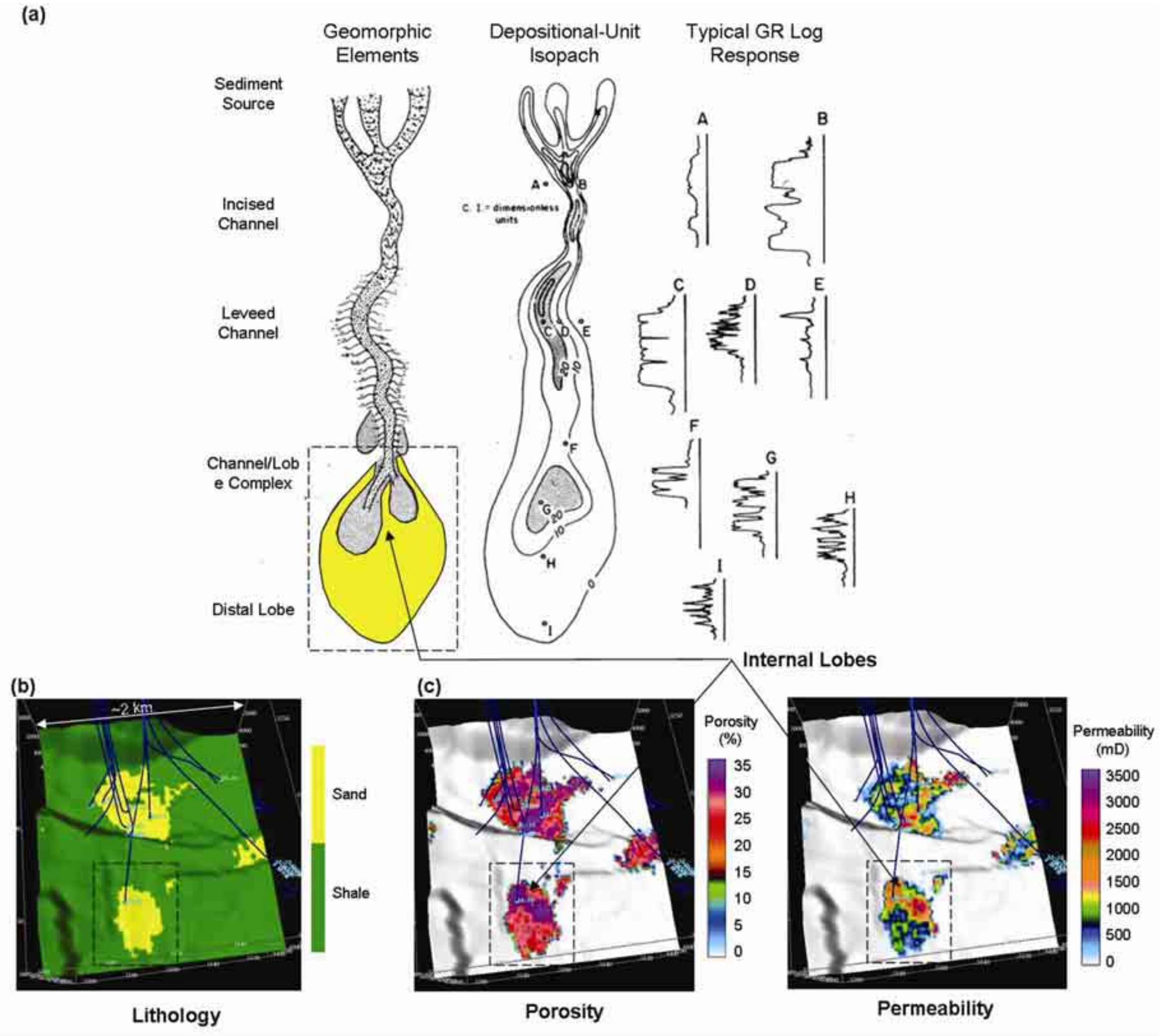

Figure 5.6: (a) Depositional model: Geomorphic elements, depositional isopach unit, and typical well-log responses of a channel-lobe complex (modified from Galloway and Hobday, 1983); (b) 3D view of stochastic inversion results (lithotypes); and (c) Co-simulated petrophysical models. The M-series reservoir sands can be interpreted as stacked turbidite lobes; in addition, internal heterogeneities associated with relatively high values of porosity and permeability can be delineated.

5.5 DETERMINISTIC VERSUS STOCHASTIC RESULTS

Numerous differences can be stated between the deterministic and stochastic inversion techniques described in this study. Firstly, deterministic inversion is based on the CSSI inversion algorithm while stochastic inversion on the MCMC algorithm. Deterministic inversion is a trace-based technique mainly based on seismic amplitude data, whereas stochastic inversion is a model-based approach that fully integrates information from different sources (seismic amplitude data, well-log, geostatistical data, and geological information). Deterministic inversion makes use of well-log data exclusively for low-frequency modeling, whereas stochastic inversion takes into account and fully honor well log data as an essential component of the simulation, and additionally generates statistical information from well-log data.

Additionally, deterministic inversion results are limited to the resolution of the seismic amplitude data (generally 4 ms sample rate) whereas stochastic inversion results can have any intermediate resolution between that of the seismic and well-log data (generally 1 ms sample rate). The inverted elastic properties from AVA deterministic inversion are in the impedance domain (Ip, Is, ρ) whereas AVA stochastic inversion solves for velocities (Vp, Vs, ρ), with the additional simulation of lithotypes. The petrophysical properties commonly derived from deterministic inversion results are porosity and fluid/lithology-sensitive modulus attributes, whereas stochastic inversion results can be used for co-simulation of multiple petrophysical parameters such as porosity, permeability, and water saturation. Lastly, the intrinsic geostatistical basis of the stochastic inversion technique allows us to generate multiple, equi-probable solution models, which in turn can be used for uncertainty assessments; deterministic inversion, on the other hand, only produces multiple solution models when the inversion parameters are changed. A detailed comparison between the deterministic and stochastic inversion techniques is summarized in Table 5.1.

Figure 5.7 graphically compares the high-resolution stochastically derived acoustic impedance (sampled at 1 ms) against the acoustic impedance yielded by 1D constrained sparse-spike inversion (CSSI, sampled at 4 ms). We emphasize the difference in vertical resolution between the deterministic and stochastic results: CSSI results are a smooth version of the well logs whereas the new stochastic inversion algorithm successfully reproduces high-resolution variations of elastic properties.

Table 5.1: Comparison between pre-stack deterministic and stochastic inversion techniques.

Inversion Type	**Trace-based**	**Model-based**
Inversion Algorithm	AVA-CSSI	AVA-MCMC
Integrated Data	Pre-stack Seismic + Well-Logs (Low Frequency only)	Pre-stack Seismic + Well-Logs + Geostatistical Data
Vertical Resolution (Sample Rate)	4 ms	1 ms
Inverted Properties	Ip, Is, Rho	Vp, Vs, Rho Lithotypes
Properties Used For Petrophysical Co-Simulation	Ip, Is	Vp, Vs, Rho
Co-Simulated Petrophysical Properties	Porosity	Porosity Permeability Water Saturation
Co-Simulation Method	Empirical Transforms	Multivariate Statistics
Multiple Realizations (Uncertainty Assessment)	No	Yes

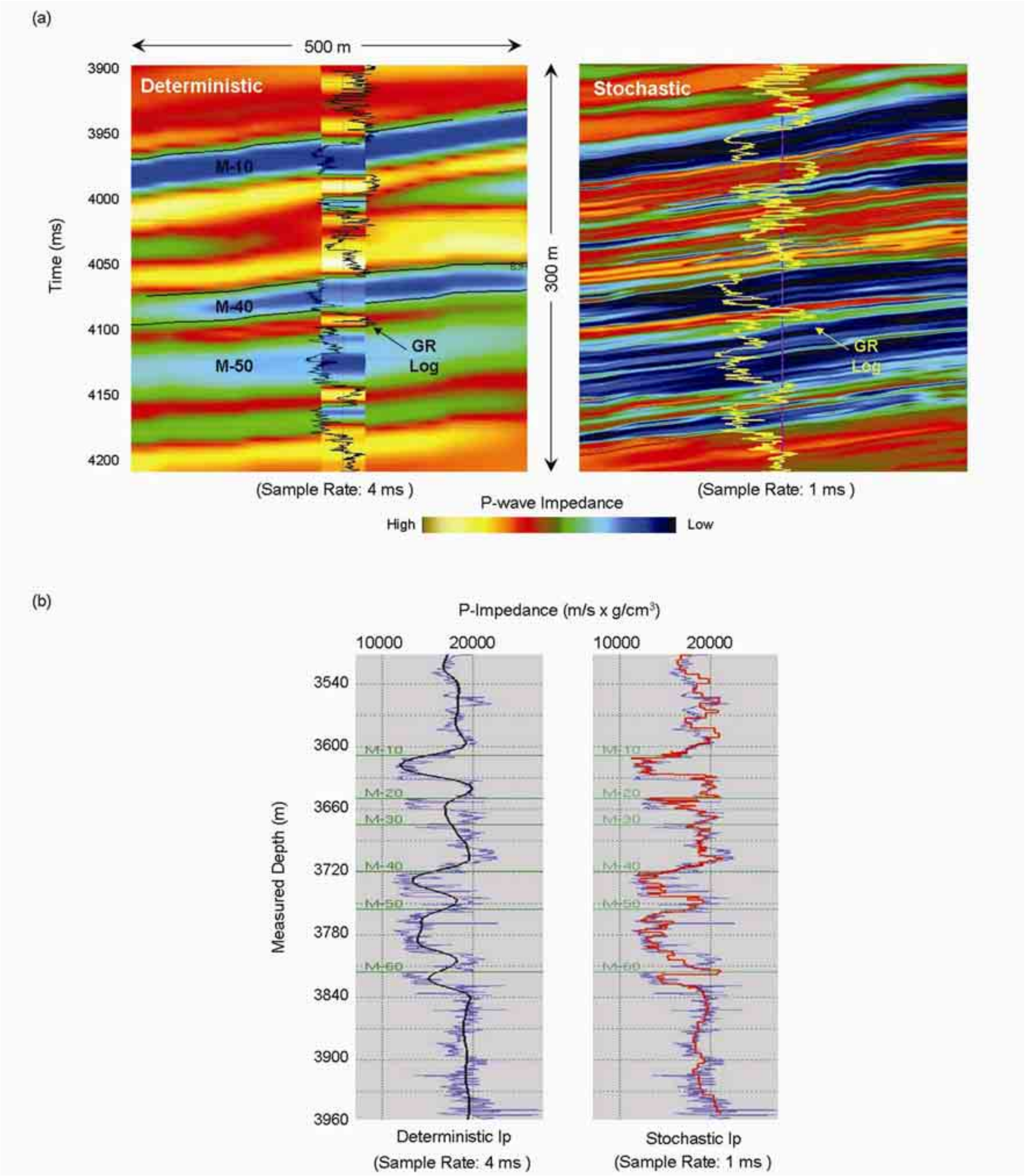

Figure 5.7: Comparison between deterministic and high-resolution stochastic inversion results in the acoustic impedance domain: (a) section view, (b) inverted pseudo-logs. Deterministic results are sampled at 4 ms whereas stochastic inversion results are sampled at 1 ms.

5.5.1 Integration of Deterministic and Stochastic Inversion Results with Depositional Model, Regional Studies, and Analogous Examples

In order to generate a conclusive geological interpretation of the M-series reservoir sands, deterministic and stochastic inversion results were integrated with depositional models, analogous examples, previous core data interpretations, and regional stratigraphic studies.

As shown in Figure 5.8, both deterministic and stochastic results clearly evidence the existence of lobate-shapes geo-bodies associates with prospective reservoir areas. Deterministic results show low "*LambdaRho*" anomalies, characteristics of hydrocarbon-bearing sands, and high-porosity geobodies simulated from the inverted P-impedance model. Similarly, lithotype distributions obtained from stochastic inversion confirm the presence of lobate-shape sand bodies. Furthermore, the co-simulated 3D models of petrophysical properties consistently reveal the existence of internal heterogeneities (small internal lobes) within the main lobes as predicted by the depositional model.

Accordingly, the channel/lobe depositional model introduced by Galloway and Hobday (1983), describe similar lobate-shaped deposits as the characteristic geomorphic feature of this base-of-slope sediments. Furthermore, the model predicts the presence of internal heterogeneities (small lobes) within the main lobe, which is clearly confirmed by the stochastically co-simulated petrophysical models. In addition, the typical GR log motif associated with this depositional setting is found to be characteristic of the logs recorded in the Marco Polo Field.

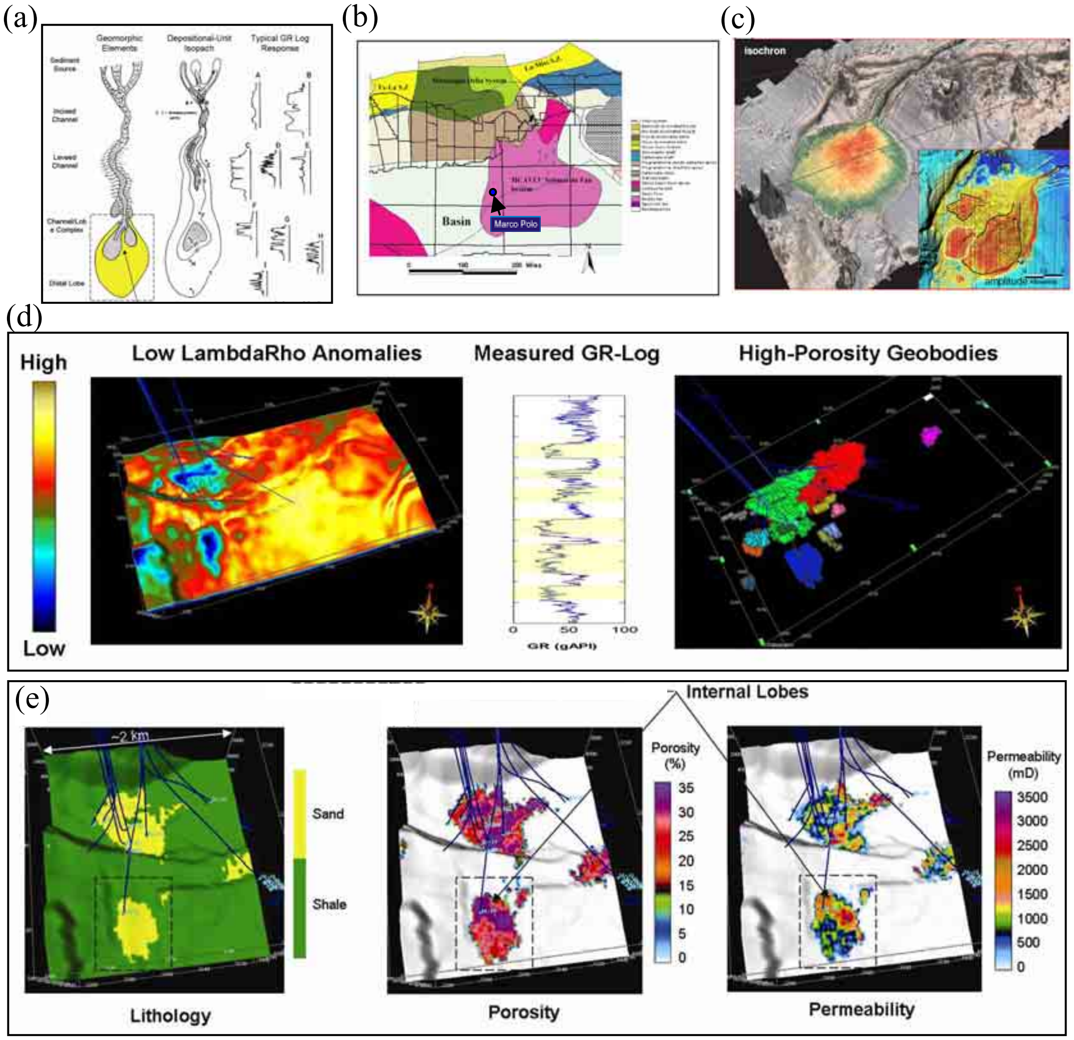

Figure 5.8: (a) Channel-lobe complex depositional model (modified from Galloway and Hobday, 1983); (b) Principal depositional systems interpreted in the Middle Miocene depositional episode in the east-central GOM basin (modified from Galloway et al., 2000). (c) Analogous example from the Niger Delta Slope: 3D perspective of a depositional lobe (From Pirmez et al., 2000). (d) Deterministic inversion results. (e) 3D view of stochastic inversion results (lithotypes) and co-simulated petrophysical models. From the integration of the information above, the M-series reservoir sands can be conclusively interpreted as stacked turbidite lobes within an overall fan complex (the MCAVLU submarine fan system).

Because of the geometry and relatively small size of the lobate geobodies obtained from the inversion results, the M-series reservoir sands can be described as “mounded” lobes rather than sheet lobes. As described by Galloway and Hobday (1985), mounded lobes are associated with sandy turbidite deposits, with low-moderate channelizations, and small areal extent (about 1 km^2). This description is consistent with the characteristics of the M-sands.

Comparison of previous regional interpretations (Galloway et al., 2000; Combellas, 2003; Wu, 2004) with the location of the Marco Polo Field indicates that the Miocene M-series sands are genetically linked to the MCAVLU submarine fan system deposition. Accordingly, Baud et al. (2000) includes the Marco Polo Field among the new deepwater plays in the Gulf of Mexico, localized within the Mississippi Fan Foldbelt. Previous core-data analyses also suggest the interpretation of the M-series reservoir sands as stacked, progradational turbidite lobes within an overall fan complex.

The analogous example from the Niger Delta shows typical lobate-shaped deepwater deposits, and also illustrates the presence of internal lobes associated with a principal lobe. These findings are clearly confirmed by the stochastic petrophysical models, where small lobate anomalies associated with high porosity and permeability values are visualized within the main sand lobe.

Finally, by integrating the information and descriptions above, the M-series reservoir sands can be conclusively interpreted as stacked turbidite lobes within an overall fan complex (the MCAVLU submarine fan system).

5.6 SUMMARY

This chapter describes the results from the successful application of the stochastic inversion algorithm to the high-resolution characterization of hydrocarbon-producing units of a deepwater reservoir in the study area. High-resolution stochastic reservoir models of elastic properties (Vp, Vs, density), lithotypes, and petrophysical properties were generated by integrating amplitude information of 3D pre-stack seismic data and well logs through well-log-derived acoustic/petrophysical statistical correlations.

Several factors differentiate deterministic and stochastic inversion techniques, including inversion algorithm, input data used, variables inverted, co-simulated properties, and sample rate of the results. However, when compared to deterministic inversion techniques the stochastic inversion procedure described in this dissertation is superior in that it allows the progressive adjustment of the vertical resolution of the estimated property distributions. The statistical nature of the algorithm allows the explicit enforcement of statistical correlations between elastic and petrophysical properties, as well as the assessment of non-uniqueness and uncertainty. All of these features make the stochastic inversion algorithm described in this study ideal for the extrapolation of petrophysical properties away from wells.

From the integration of stochastic inversion results with analogous depositional models, the M-series reservoirs have been interpreted as stacked turbidite lobes with internal heterogeneities/lobes clearly delineated, and localized within an overall fan complex (the MCAVLU submarine fan system).

Chapter 6: Conclusions

The most important purpose of this research was to develop a novel methodology for quantitative reservoir characterization based on the implementation of state-of-the-art seismic inversion techniques that truly integrate pre-stack seismic amplitude data, well-log data, geologic models, and geostatistical information. We described the successful application of the novel methodology to deepwater hydrocarbon reservoirs in the central Gulf of Mexico with emphasis on reservoir delineation and fluid/lithology characterization.

The specific sand body dimensions and geometries were determined by identifying relatively small lobate-shaped turbidite deposits of about 1 km^2 of areal extent; and we increased understanding of the factors controlling hydrocarbon distribution by selecting the appropriate geologic model (channel-lobe complexes) and describing stacked turbidite lobes with internal heterogeneities (small lobes within individual lobes) associated to high porosity/permeability areas. Additionally, we assessed the lateral extent of lithology and fluid units away from wells and estimated inter-well petrophysical properties; and quantified the effect of data- and algorithm-dependent factors on the accuracy of the inversion results through detailed sensitivity analyses.

Furthermore, the nature of AVA effects in the study area was analyzed and the hydrocarbon-bearing M-series sands were recognized as Class 3 AVO sands. To determine the sensitivity of elastic properties to changes in lithology, fluid content, and petrophysical properties, we conducted detailed sensitivity analyses which indicated that sands and shales can be clearly discriminated on the basis of elastic properties, and hydrocarbon saturation significantly affects (decreases) the P-velocity and density of the sands. Finally, the uncertainty in the stochastic lithologic and petrophysical models was quantified by analyzing the mean and standard deviation of multiple realizations.

6.1 AVA DETERMINISTIC INVERSION

AVA fluid/lithology sensitivity analysis indicates significant sensitivity of acoustic properties to fluid substitution and corroborates the existence of Class III AVA responses associated with the shale/hydrocarbon-sand interface at the top of the M-series reservoir sands. Accordingly, 1D pre-stack seismic inversion products in the form of fluid/lithology sensitive modulus attributes ($\lambda\rho$) provided accurate quantitative information about the spatial continuity of lithology and fluid units within the turbidite reservoirs.

From integration of 1D deterministic inversion results with deepwater analogue depositional models and previous rock-core studies, the M-series reservoirs have been interpreted as stacked terminal turbidite lobes within an overall fan complex. This interpretation is consistent with the channel-lobe depositional model, previous interpretations of rock-core measurements, and regional stratigraphic/depositional studies. Finally, by combining fluid/lithology sensitivity analysis techniques with 1D AVA simultaneous inversion and awareness of inversion pitfalls, it is possible to substantially reduce the risk in the exploration and development of the M-series reservoirs.

6.2 SENSITIVITY ANALYSIS OF DATA FACTORS CONTROLLING AVA DETERMINISTIC INVERSION

Detailed sensitivity analysis performed on synthetic seismic amplitude data indicates that, even in an ideal scenario (perfect knowledge of the forward model and noise-free measurements), the original elastic models used to generate synthetic seismic amplitudes are not reliably reconstructed by 1D inversion. The order of reliability of the inverted 1D distributions of elastic parameters is P-impedance, followed by S-impedance, and bulk density. Additionally, sufficient far-angle coverage is crucial for the accurate and reliable reconstruction of 1D distributions of S-impedance and bulk density. Inversion of seismic amplitude measurements indicated that time alignment of partial-angle stacks significantly improves the vertical resolution of inversion results and decreases the data misfit.

We found that the migration velocity field used to organize the pre-stack seismic amplitude data into PAS must be corrected to honor the well-log P-velocity trend imposed by the shale base line. Such correction entailed an increase of P-wave velocity, which in turn caused a decrease of the maximum angle range available for the generation of PAS. We found that by increasing the preserved AVA information via multiple single-angle stacks and by optimally selecting the maximum angle used for inversion (i.e., excluding far-angle data with low signal-to-noise ratios), the accuracy and reliability of the inverted distributions of elastic properties consistently increased. Sensitivity analysis of data-related factors affecting the reliability of pre-stack seismic inversion is crucial to avert inversion pitfalls such as over-parameterization and artificial correlation between P-impedance, S-impedance, and density.

We strongly recommend that the inversion of pre-stack seismic amplitude data be preceded by a systematic quantitative analysis of the influence of data related factors on the estimated distributions of elastic parameters. Forward modeling based on well logs and subsequent inversion with realistic wavelets is an excellent alternative to assess the reliability and vertical resolution of inversion products as a function of angle range, number of PAS, and signal-to-noise ratios of the simulated seismic amplitude data.

6.3 AVA STOCHASTIC INVERSION: ALGORITHM DESCRIPTION AND SENSITIVITY ANALYSIS

Stochastic inversion of pre-stack seismic data and well logs yields high-resolution spatial distributions of elastic and petrophysical properties. This is possible because pre-stack seismic data are sensitive to three independent elastic properties (Vp, Vs, density) that are, in principle, statistically related to lithology, porosity, and type of saturating fluid. Consequently, compared to post-stack seismic data, pre-stack seismic data provide additional degrees of freedom for the accurate co-simulation of petrophysical properties via multivariate statistics.

Pre-stack stochastic inversion results are relatively sensitive to inversion parameters such as variogram model, lateral correlation length, and lithotype fraction. Sensitivity analyses and blind tests indicate that thick sands are accurately reconstructed by the inversion and are relatively insensitive to slight changes in the assumed inversion parameters. Moreover, the statistical uncertainty of the extrapolation monotonically decreases away from well locations in a manner that is consistent with the assumed variogram range.

Definition of accurate multidimensional correlations between elastic and petrophysical properties depends on the quality of the well-log data and associated petrophysical estimations, as well as on the degree of statistical correlation among such properties. Consequently, the accuracy of the results is directly proportional to the reservoir quality of the sand units involved in the prediction. The best extrapolations of lithology units and petrophysical properties away from wells are obtained for clean and high-porosity reservoir units whose thickness is above the vertical resolution of the seismic data.

6.4 APPLICATION OF AVA STOCHASTIC INVERSION FOR HIGH-RESOLUTION RESERVOIR CHARACTERIZATION

The methodology for high-resolution pre-stack reservoir characterization and petrophysical modeling consists of (1) generating reliable volumes of elastic properties from simultaneous stochastic inversion of high-quality partial angle stacks, (2) at the same time obtaining realizations of lithotype via mutual thresholding from the elastic volumes as control fields, (3) establishing precise lithotype-dependent and multidimensional correlations between elastic and petrophysical properties at well locations, and (4) using those correlations in conjunction with the simulated lithotype field to guide the petrophysical co-simulations from inverted volumes of elastic properties.

Stochastic inversion results are consistent with deepwater depositional models; therefore, the M-series reservoir sands can be described as stacked turbidite lobes. Furthermore, the co-simulated 3D models of petrophysical properties consistently reveal the existence of internal heterogeneities (small internal lobes) within the main lobes as predicted by the depositional model.

When compared to deterministic amplitude-versus-angle (AVA) inversion techniques (e.g., constrained sparse-spike inversion), the stochastic inversion procedure described in this dissertation is superior in that it allows the progressive adjustment of the vertical resolution of the estimated property distributions. Moreover, the stochastic inversion algorithm makes use of a statistically consistent criterion to adjust the fit to the seismic and well-log data without enforcing unrealistic spatial variations in the inverted distributions. Finally, the statistical nature of the algorithm allows the explicit enforcement of statistical correlations between elastic and petrophysical properties, as well as the assessment of non-uniqueness and uncertainty. All of these features make the stochastic inversion algorithm described in this study ideal for the extrapolation of petrophysical properties away from wells.

From the integration of deterministic and stochastic inversion results with depositional models, analogous examples, and previous regional stratigraphic studies, the M-series reservoir sands can be conclusively described as stacked turbidite lobes within an overall fan complex (the MCAVLU submarine fan system).

Appendix: AVA-CSSI Inversion Algorithm

While the inversion algorithm developed and implemented by Fugro-Jason considers several variants for data conditioning, model parameterization, model constraints, and stabilization, in this appendix we explain only the specific version and features of the algorithm implemented to obtain the results described in the dissertation.

One-dimensional inversion of AVA surface seismic amplitude measurements yields distributions of P-impedance (I_p), S-impedance (I_s), and bulk density (ρ) as functions of normal-incidence seismic travel time.

The algorithm used in this study for the 1D inversion of NMO-corrected AVA seismic amplitude measurements is based on a sparse-spike regularization strategy. This procedure emphasizes PP reflectivity models that exhibit a prescribed degree of sparsity (or clustering) of reflectors. P- and S-impedances and density are further constrained to remain within upper and lower bounds inferred from well logs (thus why the name "AVA constrained sparse-spike inversion," or AVA-CSSI, used when referring to this inversion algorithm). The inversion of 1D AVA seismic amplitude measurements is performed by minimizing the constrained objective function $\mathbf{F}(I_P, I_S, \rho)$ given by

$$\mathbf{F}(I_P, I_S, \rho) = \alpha \sum_{i,j} \left[S_{ij}^{\;data} - S_{ij}(I_P, I_S, \rho) \right]^2 + \sum_{i,j} \left| R_{ij}(I_P, I_S, \rho) \right|$$

$$+ \sum_{i} \left[\left| I_P^{low} - \hat{I}_P^{low} \right| + \left| I_s^{low} - \hat{I}_S^{low} \right| + \left| \rho^{low} - \hat{\rho}^{low} \right| \right] , \qquad \text{(A.1)}$$

subject to

$I_{P\min} \le I_P \le I_{P\max}$,
$I_{S\min} \le I_S \le I_{S\max}$, and
$\rho_{\min} \le \rho \le \rho_{\max}$.

In the above expressions, I_P, I_S, and ρ designate functions sampled at discrete values of normal seismic travel time, i is the partial-angle stack index, j is the sample (time) index, R_{ij} identifies the angle-dependent PP reflectivity coefficients, S_{ij}^{data} is the measured AVA seismic amplitude data, and $S_{ij}(I_P, I_S, \rho)$ is the 1D numerically simulated AVA seismic amplitude data. The variables $\hat{I}_P^{low}$, $\hat{I}_S^{low}$, and $\hat{\rho}^{low}$ designate low-frequency components of P-impedance, S-impedance, and bulk density, respectively previously interpolated and low-pass filtered from available well-log measurements, while the variables I_P^{low}, I_S^{low}, and ρ^{low} designate the corresponding low-pass filtered components of the inverted models. Moreover, the functions $I_{P\min}$, $I_{P\max}$, $I_{S\min}$, $I_{S\max}$, $\rho_{\min}$, and $\rho_{\max}$ identify time-dependent value-range constraints enforced by the inversion.

The first additive term (ℓ_2-norm) of the cost function **F** given by equation (A-1) enforces a prescribed degree of misfit between the numerically simulated and measured pre-stack seismic amplitude data. The second additive term (ℓ_1-norm) of the objective function biases the estimation of P-impedance, S-impedance, and density to render sparse and amplitude-constrained time sequences of angle-dependent PP reflectivity coefficients. Finally, the third additive term of the objective function (ℓ_1-norm) biases the low-frequency components of the estimated P-impedance, S-impedance, and density toward the corresponding pre-defined volumes of low-frequency properties. The second and third additive components of the cost function are included to stabilize the inversion in the presence of noisy and inadequate AVA seismic amplitude measurements. In so doing, the user-defined scalar α in equation (A-1) is chosen to control the sparsity and amplitude of the estimated angle-dependent reflection coefficients when decreasing the data misfit (Debeye and van Riel, 1990, and Oldenburg et al., 1983). Unaccounted presence of noise in the input AVA seismic amplitude data may cause the inversion to yield spurious reflectors (associated with spurious reflectivities). Thus, the adjustment of α prevents the inversion from mapping noisy AVA seismic measurements into non-existing reflectors. The use of mixed norms in the cost function **F** is intended to reduce Gibb's-type oscillations in the inverted 1D distribution of elastic parameters that could be mistakenly associated with non-existing reflectors (Oldenburg et al., 1983).

In the inversion exercises considered in this dissertation, we enforced wide-open value-range model constraints. The enforced value of α was estimated from trial-and-error by best-fitting existing well logs. Finally, we generated the low-frequency model components from low-pass filtered versions of the 3D volumes of properties interpolated from well logs.

References

Aki, K., and P. G. Richards, 1980, Quantitative Seismology: W. H. Freeman and Co.

Bashore, W., U. Araktingi, , M.Levy, and W. Schweller, 1993, The importance of the geological model for reservoir characterization using geostatistical techniques and the impact on subsequent fluid flow: SPE No. 26474 presented at the 68th Annual Technical Conference and Exhibition of the Society of Petroleum Engineers held in Houston, Texas.

Bassiouni, Z., 1994, Theory, measurement, and interpretation of well logs: SPE Textbook Series Vol. 4.

Baud R. D., R. H. Peterson, C. Doyle, and G.E. Richardson, 2000, Deepwater Gulf of Mexico 2000: America's Emerging Frontier, OCS Report MMS 2000-022.

Biot, M. A., 1956, Theory of propagation of elastic waves in a fluid saturated porous solid, I Low frequency range, The Journal of the Acoustical Society of America, 28, 168-178.

Box, G., G. Jenkins, and G. Reinsel, 1994, Time Series Analysis: Prentice Hall.

Brown, A. R., 1999, Interpretation of three-dimensional seismic data: AAPG Memoir Series Vol. 42.

Buffler, R. T., and D. S. Sawyer, 1985, Distribution of crust and early history, Gulf of Mexico basin: Gulf Coast Association of Geological Societies Transactions, 35, 333-344.

Buffler, R. T., 1989, Distribution of crust, distribution of salt, and the early evolution of the Gulf of Mexico: SEPM Gulf Coast Section 10th Annual Research Foundation Conference, p. 25-27.

Buffler, R. T., 1991, Seismic stratigraphy of the deep Gulf of Mexico basin and adjacent margins, *in* A. Salvador, ed., The Gulf of Mexico Basin: Boulder,Colorado, Geological Society of America, The Geology of North America, 1, 353-387.

Castagna, J., and M. Backus, 1993, Offset dependent reflectivity- theory and practice of AVO analysis: Society of Exploration Geophysicists.

Chilés, J., and P. Delfiner, 1999, Geostatistics: modeling spatial uncertainty: John Wiley and Sons, Wiley Series in Probability and Statistics, New York, p. 695.

Colling, Jr, E. L., R. J. Alexander, and R. L. Phair, 2001, Regional mapping and maturity modeling for the northern deep water Gulf of Mexico, *in* R. H. Fillon, N. C. Rosen, P. Weimer, A. Lawrie, H. Pettingill, R. L. Phair, H.H. Roberts, and B. van Hoorn, eds., Petroleum systems of deep-water basins global and Gulf of Mexico experience: SEPM Gulf Coast Section 21st Annual Research Foundation Conference, p. 87-110.

Combellas, R., 2003, Depositional and structural evolution of the Middle Miocene depositional episode, East-Central Gulf of Mexico: Ph.D. Dissertation, The University of Texas at Austin, Austin, Texas.

Contreras, A., C. Torres-Verdin, W. Chester, K. Kvien, and T. Fasnacht, 2005, Joint stochastic inversion of petrophysical logs and 3D pre-stack seismic data to assess the spatial continuity of fluid units away from wells: Application to a Gulf of Mexico deepwater hydrocarbon reservoir. SPWLA 46th Annual Logging Symposium.

Contreras, A., C. Torres-Verdin, and T. Fasnacht, *in press*, AVA simultaneous one-dimensional inversion of partially-stacked seismic amplitude data for the spatial delineation of lithology and fluid units of deepwater hydrocarbon reservoirs in the central Gulf of Mexico: Geophysics.

Curtis, D. M., 1970, Miocene deltaic sedimentation, Louisiana Gulf Coast, *in* Morgan, J. P., ed., Deltaic sedimentation, modern and ancient: SEPM Special Publication 15, p. 293-308.

Debeye, H., and P. van Riel, 1990, Lp-norm deconvolution: Geophysical Prospecting, 38, 381-403.

Debeye, H., E. Sabbah, and P. van der Made, , 1996, Stochastic inversion: SEG 66 Annual International Meeting held in Denver, Colorado.

Deutsch, C., and A. Journel, 1998, GSLIB, Geostatistical Software Library and User's Guide: Oxford University Press.

Dresser Atlas, 1992, Introduction to Wireline Log Analysis: Houston, TX (Western Atlas International)

Domenico, S., 1984, Rock lithology and porosity determination from shear and compressional wave velocity: Geophysics, 49, 1188-1195.

Doyen, P., 1988, Porosity from seismic data: A geostatistical approach: Geophysics, 53, 1263-1275.

Feng, J., 1995, Post mid- cretaceous seismic stratigraphy and depositional history, deep Gulf of Mexico: The University of Texas at Austin, Ph.D. dissertation, 253 p.

Fisher, W. L., and J. H. McGowen, 1967, Depositional systems in the Wilcox Group of Texas and their relationship to occurrence of oil and gas: Gulf Coast Association of Geological Societies Transactions, v. 17, p. 105-125.

Galloway, W., 1998, Siliciclastic slope and base of slope depositional systems: component facies, stratigraphic architecture, and classification: AAPG Bulletin, 82, 569-595.

Galloway, W., and D. Hobday, 1996, Terrigenous clastic depositional systems: applications to fossil fuel and groundwater resources: Springer-Verlag.

Galloway, W., R. Buffler, P. Ganey-Curry, and X. Li, 2000, Gulf of Mexico depositional synthesys project: Cenozoic depositional history of the Gulf Basin: AAPG Bulletin, 84, 1743-1774.

Gambús, M., and C. Torres-Verdín, 2002, High-resolution geostatistical inversion of a 3D seismic data set acquired in a Gulf of Mexico gas field: 72nd Annual Technical Conference and Exhibition , SEG, Expanded Abstracts.

Gassmann, F., 1951, Elastic waves through a packing of spheres: Geophysics, 16, 673-685.

Geertsma, J., 1961, Velocity-log interpretation: The effect of rock bulk compressibility: Soc. Pet. Eng., 1, 235-248.

Gilks, W., S. Richardson, and D. Spiegelhalter, 1996, Markov Chain Monte Carlo in practice: Chapman & Hall/CRC, Interdisciplinary Statistics, London, p. 486.

Goodway, W., T. Chen, and J. Downton, 1997, Improved AVO fluid detection and lithology discrimination using Lame petrophysical parameters: 67th Annual International Meeting, SEG, Expanded Abstracts, 183-186.

Goodman, J., and A. Sokal, 1989, Multigrid Monte Carlo method. Conceptual foundations: Physical Review D, volume 40, p. 2035-2071.

Greenberg, M., and J. Castagna, 1992, Shear-wave velocity estimation in porous rocks: Theoretical formulation, preliminary verification and application. Geophysical Prospecting, 40, 195-209.

Grijalba-Cuenca, A., C. Torres-Verdín, and H. Debeye, 2000, Geostatistical inversion of 3D seismic data to extrapolate wireline petrophysical variables laterally away from the well: SPE No. 63283 presented at the Annual International Technical Conference, Dallas, Texas.

Haas, A., and O. Dubrule, 1994, Geostatistical inversion: a sequential method for stochastic reservoir modeling constrained by seismic data: First Break, 12, 561-569.

Journel, A., and C. Huijbregts, 1978, Mining Geostatistics: Academic Press Inc.

Kleverlaan, K., 1989, Three distinctive feeder-lobe systems within one time slice of the Tortonian Tabernas fan, SE Spain: Sedimentology, 36, 25-45.

Koefoed, O., 1962, Reflection and transmission coefficients for plane longitudinal incident waves: Geophysical Prospecting, 10, 304-351.

Kormendi, F., and M. Dietrich, 1991, Nonlinear waveform inversion of plane-wave seismograms in stratified elastic media: Geophysics, 56, 664–674.

Latimer, R. B., R. Davison, and P. van Riel, 2000, An interpreter's guide to understanding and working with seismic-derived acoustic impedance data: The Leading Edge, 19, 242-256.

Liner, C. L., 1999, Elements of 3D seismology: PennWell Publishing.

Lortzer, G., and A. Berkhout, 1992, An integrated approach to lithologic inversion – Part1: Geophysics, 57, 233-245.

Madiba G.B., and G.A. McMechan, 2003a, Seismic impedance inversion and interpretation of a gas carbonate reservoir in the Alberta Foothills, western Canada: Geophysics, 68, 1460-1469.

Madiba G.B., and G.A. McMechan, 2003b, Processing, inversion, and interpretation of a 2D seismic data set from the North Viking Graben, North Sea: Geophysics, 68, 837-848.

Mallick, S., 1999, Some practical aspects of prestack waveform inversion using a genetic algorithm: An example from the east Texas Woodbine gas sands: Geophysics, 64, 326–336.

Maureau, G., and D. Van Wijhe, 1979, The prediction of porosity in the Permian carbonate of eastern Netherlands using seismic data: Geophysics, 44, 1502-1517.

Mavko, G., T. Mukerji, and J. Dvorkin, 1996, Rock Physics Handbook: Stanford University.

Menke, W., 1989, Geophysical data analysis: Discrete inverse theory: International Geophysics Series, Vol. 45, Academic Press.

Merkel, R., R. Barree, and G. Towle, 2001, Seismic response of Gulf of Mexico reservoir rocks with variations in pressure and water saturation: The Leading Edge, 20, 290-299.

Meyerhoff, A. A., 1968, Geology of natural gas in south Louisiana, *in* Beebe, B. W., ed., Natural gases of North America: AAPG Memoir 9, p. 376-581

Montgomery, D., 1991, Introduction to Statistical Quality Control: John Wiley and Sons.

Mutti, E., 1992, Turbidite sandstone: AGIP, Italy, 275 p.

Mutti, E., and F. Ricci Lucci, 1972, Turbidites of the Northern Apennines: introduction to facies analysis: International Geological Review, 20, 125-166.

Mutti, E. and W. R. Normark, 1991, An integrated approach to the study of turbidite systems, *in* P. Weimer, M. H. Link, eds., Seismic facies and sedimentary processes of submarine fans and turbidite systems, New York, Sringer-Verlag, p. 75-105.

Mutti E., W. R. Normark, and M. Park, 1987, Comparing examples of modern and ancient turbidite systems: problems and concepts, *in* J. K. Legget, G. G. Zuffa, eds., Marine clastic sedimentology, London, Graham and Trotman, p. 1-38.

Nehring, R, 1991, Oil and gas resources in Salvador, A., ed., The Gulf of Mexico basin: Boulder, Colorado, Geological Society of America, The geology of North America, p. 445-494.

Normark W. R., D. J. W. Piper, and G. Hess, 1979, Distributary channels, sand lobes, and mesotopography of Navy Submarine Fan, California Borderland, with applications to ancients fan sediments: Sedimentology, 26, 749-774.

Normark W. R. and D. J. W. Piper, 1985, Navy Fan, Pacific Ocan, *in* A.H. Bouma, W. R. Normark, N. E. Barnes, eds., Submarine fans and related turbidite systems, New York, Sringer-Verlag, p. 87-94.

Oldenburg, D., T. Scheuer, and S. Levy, 1983, Recovery of the acoustic impedance from reflection seismograms: Geophysics, 48, 1318-1330.

Pan, G. S., and R. A. Phinney, 1989, Full-waveform inversion of plane wave seismograms in stratified acoustic media: Applicability and limitations: Geophysics, 54, 368–380.

Pendrel, J., H. Debeye, R. Pedersen-Tatalovic, B. Goodway, J. Dufour, M. Boggards, and R. Stewart, 2000, Estimation and interpretation of P and S impedance volumes from simultaneous inversion of P-wave offset seismic data: 70th Annual International Meeting, SEG, Expanded Abstracts, 146-149.

Pendrel, J., and P. van Riel, 1997, Estimating porosity from 3D seismic inversion and 3D geostatistics: Presented at the 67th Annual International Meeting, SEG.

Piper D. J. W. and W. R. Normark, 1983, Turbidite depositional patterns and flow characteristics, Navy Submarine Fan, California Borderland: Sedimentology, 30, 681-694.

Pirmez C., R. T. Beaubouef, S. J. Friedmann, and D. C. Mohrig, 2000, Equilibrium profile and base level in submarine channels: Examples from late Pleistocene systems and implications for the architecture of deepwater reservoirs: GCSSEPM Foundation 20th Annual Research Conference Deep-Water Reservoirs of the World, 782-805.

Rain, D. B., and D. B. Meyer, 2001, A deepwater odyssey, the past and the future potential of the deepwater Gulf of Mexico (abs): AAPG Bulletin, 85, 121.

Rainwater, E. H., 1964, Regional stratigraphy of the Gulf Coast Miocene: Gulf Coast Association of Geological Societies Transactions, 14, 81-124.

Roy, I. G., M. Sen, C. Torres-Verdin, and O. Varela, 2004, Prestack inversion of a Gulf of Thailand (OBC) data set: Geophysics, 69, 1470–1483.

Rutherford, S., and R. Williams, 1989, Amplitude-versus-offset variations in gas sands: Geophysics, 54, 680-688.

Sen, M. K., and P. L. Stoffa, 1991, Nonlinear one-dimensional seismic waveform inversion using simulated annealing: Geophysics, 56, 1624–1638. [ISI] Global optimization methods in geophysical inversion, Elsevier Science Publ. Co.: 1995.

Sen, M. K., and P.L. Stoffa, 1995, Global optimization methods in geophysical inversion: Elsevier Science Publishing Co.

Sen, M. K., and I. G. Roy, 2003, Computation of differential seismogram and iteration adaptive regularization in prestack waveform inversion: Geophysics, 68, 2026–2039.

Shanmugam G. and R. J. Miola, 1988, Submarine fans: characteristics, models, classification, and reservoir potential: Earth Science Reviews 24, 383-428.

Tarantola, A., 2005, Inverse problem theory and methods for model parameter estimation: Society for Industrial and Applied Mathematics, Philadelphia, p. 342.

Tatham, R., and M. McComack, 1991, Multicomponent seismology in petroleum exploration: SEG Publication.

Torres-Verdín, C., M. Victoria, G. Merletti, and J. Pendrel, 1999, Trace-based and geostatistical inversion of 3D seismic data for thin-sand delineation: An application to San Jorge Basin, Argentina: The Leading Edge, 18, 1070-1076.

White, R. E., 1980, Partial coherence matching of synthetic seismograms with seismic traces: Geophysical Prospecting, 28, 333-358.

Winker, C. D., and J. R. Booth, 2000, Sedimentary dynamics of the salt-dominated continental slope, Gulf of Mexico: integration of observations from the seafloor, near-surface, and deep subsurface, *in* P. Weimer, R. M. Slatt, J. Coleman, N.C. Rosen, H. Nelson, A. H. Bouma, M. J. Styzen, and D. T. Lawrence, eds., Deep-water reservoirs of the world: SEPM Gulf Coast Section 20th Annual Research Foundation Conference, p. 1059-1086.

Winker, C. D., and R. T. Buffler, 1988, Paleogeographic evolution of early deepwater Gulf of Mexico and margins, Jurassic to Middle Cretaceous (Comanchean): AAPG Bulletin, 72, 318-346.

Winker, C. D., 1982, Cenozoic shelf margins, Northwestern Gulf of Mexico: Gulf Coast Association of Geological Societies Transactions, v. 32, p. 427-448.

Woodbury, H. O., I. B. Murray, Jr., P. J. Pickford, and W. H. Akers, 1973, Pliocene and Pleistocene depocenters, outer continental shelf, Louisiana and Texas: AAPG Bulletin, 54, 2428-2439.

Wu, X., 2004, Upper Miocene depositional history of the central Gulf of Mexico Basin: Ph.D. Dissertation, The University of Texas at Austin, Austin, Texas.

Xia, G., M. K. Sen, and P. L. Stoffa, 1998, 1-D elastic waveform inversion: A divide-and-conquer approach: Geophysics, 63, 1670–1684.

Vita

Arturo Javier Contreras was born in Barquisimeto, Venezuela on April 20, 1975, the son of Miguel Contreras and Edith Santos. After completing his work at High School for Industrial Technology "MFF" in Cagua, Venezuela, he received the degree of Electrical Technician in June 1992. In September of the same year, he entered the Engineering Department of Universidad Central de Venezuela (UCV) in Caracas, Venezuela. He received the degree of Bachelor of Science in Geophysical Engineering from UCV in January 2000. Upon graduation, he joined the UCV-Department of Geophysical Engineering as lecturer. In January 2001 he enrolled in The University of Texas at Austin for graduate studies (Ph.D.) in Geological Sciences.

Permanent address: Urb. La Haciendita, Edif. Arauca, Apto. B-11
Cagua, Edo. Aragua, Venezuela

This dissertation was typed by the author.